

Contents

I Preliminaries	3
1 RBF Methods for PDEs	4
1.1 Survey of Related Work	5
1.1.1 Global RBF Methods	8
1.1.2 Compactly Support RBFs	9
1.1.3 Local RBF Methods	10
1.1.4 Recent Advances in Conditioning	11
1.2 Comparison of RBF Methods	11
1.2.1 RBF Scattered Data Interpolation	12
1.2.2 Reconstructing Solutions for PDEs	13
1.2.3 PDE Methods	14
1.2.4 Local Methods	17
2 Introduction to RBF-FD	19
2.1 Background	20
2.2 The RBF-generated Finite Differences Method	21
2.2.1 Stencil Weights	22
2.2.2 Differentiation Matrix	23
2.2.3 Multiple Operators	23
2.2.4 Weight Operators	24
2.3 Implementation	28
2.3.1 Grid	29
2.3.2 Generating Stencils	30
2.3.3 Approximate Nearest Neighbor (ANN) Query	32
2.3.4 On Choosing the Right ϵ	33
3 A Distributed Multi-GPU RBF-FD Implementation	34
4 Parallel Solvers	36
4.1 On the use of libraries for parallel solvers	37
4.2 Partitioning	37
4.3 Local node ordering	38
4.4 Two level parallelism	41
4.4.1 Explicit Solvers	41
4.4.2 Fragments (integrate above)	45

4.4.3	Implicit Solvers	45
4.5	RBF-FD as SpMV	47
5	Numerical Validation	48
5.1	Choosing ϵ	48
5.1.1	CVT epsilon tests	48
5.2	Parabolic	48
5.3	Hyperbolic	48
5.3.1	Vortex Rollup	50
5.3.2	Solid body rotation	52
5.4	Fragments (integrate above)	55
5.4.1	CFL	56
5.5	GFLOP Throughput	56
5.6	Elliptic	57
6	Stokes	58
6.1	Introduction	58
6.2	Bad Problem	61
6.2.1	Details	61
6.3	RBF-FD Weights	61
6.4	GPU Based Solver	62
6.4.1	GMRES Algorithm	62
6.4.2	Multiple GPUs	63
6.5	Multiple GPUs	64
6.5.1	Solution Ordering	65
6.6	Governing Equations	66
6.6.1	Constraints	68
6.6.2	Manufactured Solution	68
6.7	Preconditioning	69
6.8	GMRES Results	70
6.9	Fragments	70

Part I

Preliminaries

Chapter 1

RBF Methods for PDEs

The process of solving partial differential equations (PDEs) using radial basis functions (RBFs) dates back to 1990 [47, 48]. However, at the core of all RBF methods lies the fundamental problem of approximation/interpolation. Some methods (e.g., global- and compact-RBF methods) apply RBFs to approximate derivatives directly. Others (e.g., RBF-generated Finite Differences) leverage the basis functions to generate weights for finite-differencing stencils, utilizing the weights in turn to approximate derivatives. Regardless, to track the history of RBF methods, one must look back to 1971 and R.L. Hardy’s seminal research on interpolation with multi-quadric basis functions [40].

As “meshless” methods, RBF methods excel at solving problems that require geometric flexibility with scattered node layouts in d -dimensional space. They naturally extend into higher dimensions without significant increase in programming complexity [27, 85]. In addition to competitive accuracy and convergence compared with other state-of-the-art methods [24, 25, 27, 28, 85], they also boast stability for large time steps.

This chapter is dedicated to summarizing the four-decade history of RBF methods leading up to the development of the RBF-generated Finite Differences (RBF-FD) method. Beginning with a brief introduction to RBFs and a historical survey, we attempt to classify related work into three types: global, compact, and local methods. Following this, the general approximation problem is introduced, with a look at the core of all three method classifications: RBF scattered-data interpolation.

Three global RBF collocation methods are presented: Kansa’s method, Fasshauer’s method and Direct collocation. Within the historical context of RBF methods we highlight extensions that lead to local interpolation matrices instead of a single global interpolation matrix. Additionally, the RBF-pseudospectral (RBF-PS) method is shown as an extension to fit global RBF methods into the framework of lower complexity pseudo-spectral methods.

By surveying related work in the field of RBF PDE methods, we frame the context in which RBF-FD was developed, and illustrate both the benefits and pitfalls inherited from its predecessors.

1.1 Survey of Related Work

In Radial Basis Function methods, radially symmetric functions provide a non-orthogonal basis used to interpolate between nodes of a point cloud. RBFs are univariate and a function of distance from a center point defined in \mathbb{R}^d , so they easily extend into higher dimensions without significant change in programming complexity. Examples of commonly used RBFs from the literature are provided in Table 1.1; 2D representations of the same functions can be found in Figure 1.1. Figure 1.2 illustrates the radial symmetry of RBFs—in this case, a Gaussian RBF—in the first three dimensions.

RBF methods are based on a superposition of translates of these radially symmetric functions, providing a linearly independent but non-orthogonal basis used to interpolate between nodes in d -dimensional space. The interpolation problem—referred to as *RBF scattered data interpolation*—seeks the unknown coefficients, $\mathbf{c} = \{c_j\}$, that satisfy:

$$\sum_{j=1}^N \phi_j(r(\mathbf{x})) c_j = f(\mathbf{x}),$$

where $\phi_j(r(\mathbf{x}))$ is an RBF centered at $\{\mathbf{x}_j\}_{j=1}^n$. In theory the radial coordinate, $r(\mathbf{x})$, could be any distance metric, but is most often assumed to be $r(\mathbf{x}) = \|\mathbf{x} - \mathbf{x}_j\|_2$ (i.e., Euclidean distance), as it is here. The coefficients \mathbf{c} result in a smooth interpolant that collocates sample values $f(\mathbf{x}_j)$. An example of RBF interpolation in 2D using 15 Gaussians is shown in Figure 1.3.

RBFs have been shown in some cases to have exponential convergence for function approximation [21]. It is also possible to reformulate RBF methods as pseudospectral methods that have generated solutions to ill-posed problems for which Chebyshev-based and other pseudospectral methods fail [19]. However, as with all methods, RBFs come with certain limitations. For example, RBF interpolation is—in general—not a well-posed problem, so it requires careful choice of positive definite or conditionally positive definite basis functions (see [21, 43] for details).

RBFs depend on a shape or support parameter ϵ that controls the width of the function. The functional form of the shape function becomes $\phi(\epsilon r(\mathbf{x}))$. For simplicity in what follows, we use the notation $\phi_j(\mathbf{x})$ to imply $\phi(\epsilon \|\mathbf{x} - \mathbf{x}_j\|_2)$. Decreasing ϵ increases the support of the RBF and in most cases, the accuracy of the interpolation, but worsens the conditioning of the RBF interpolation problem [67]. This inverse relationship is widely known as the *Uncertainty Relation* [43, 67]. Fortunately, recent algorithms such as Contour-Padé [31] and RBF-QR [33, 35] allow for numerically stable computation of interpolants in the nearly flat RBF regime (i.e., $\epsilon \rightarrow 0$) where high accuracy has been observed [36, 52].

RBF methods for interpolation first appeared in 1971 with Hardy’s seminal research on multiquadratics [40]. In his 1982 survey of scattered data interpolation methods [37], Franke rated multiquadratics first-in-class against 28 other methods (3 of which were RBFs) [37]. Many other RBFs, including those presented in Table 1.1 have been applied in literature, but for PDEs in particular, none have rivaled the attention received by multiquadratics.

By 1990, the understanding of the scientific community regarding RBFs was sufficiently

Name	Abbrev.	Formula	Order (m)
Multiquadric	MQ	$\sqrt{1 + (\varepsilon r)^2}$	1
Inverse Multiquadric	IMQ	$\frac{1}{\sqrt{1+(\varepsilon r)^2}}$	0
Gaussian	GA	$e^{-(\varepsilon r)^2}$	0
Thin Plate Splines	TPS	$r^2 \ln r $	2
Wendland (C^2)	W2	$(1 - \varepsilon r)^4(4\varepsilon r + 1)$	0

Table 1.1: Examples of frequently used RBFs based on [21, 36]. ε is the support parameter. All RBFs have global support. For compact support, enforce a cut-off radius (see Equation 1.1).

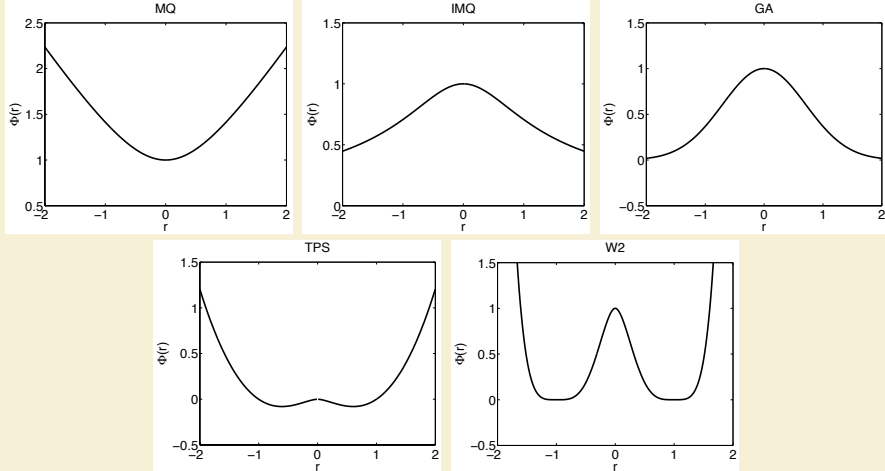


Figure 1.1: Example RBF shapes from Table 1.1 with parameter $\varepsilon = 1$.

developed for collocating PDEs [47, 48]. PDE collocation seeks a solution of the form

$$(\mathcal{L}u)(x_i) = \sum_{j=1}^N \phi_j(x_i) c_j = f(x_i)$$

where \mathcal{L} is, in general, a nonlinear differential operator acting on $u(x)$. The solution $u(x)$ is expressed as a linear combination of N basis functions $\phi_j(x)$, not necessarily RBFs:

$$u(x) = \sum_{i=1}^N \phi_j(x) c_j$$

As in the problem of RBF scattered data interpolation, $\mathbf{c} = \{c_j\}$ is the unknown coefficient vector. Under the assumption that \mathcal{L} is a linear operator, one can collocate the differential equation. Alternatively, individual derivative operators can be expressed as linear combinations of the unknowns u_j (leading to the RBF-FD methods). In all cases, a linear system

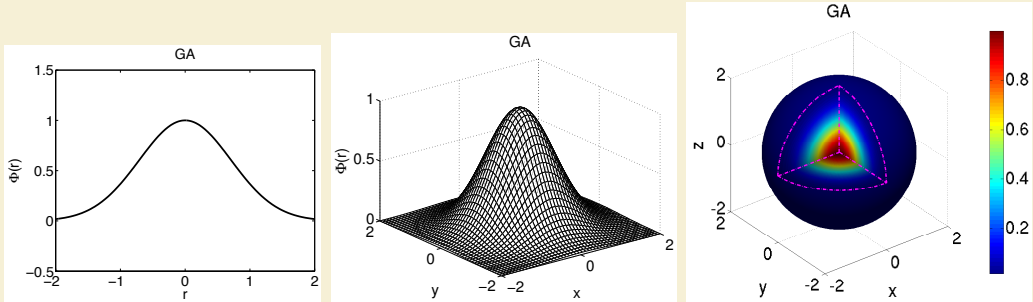


Figure 1.2: The Gaussian (GA) RBF (Table 1.1) with parameter $\epsilon = 1$ and r in $D = 1, 2$ and 3 .

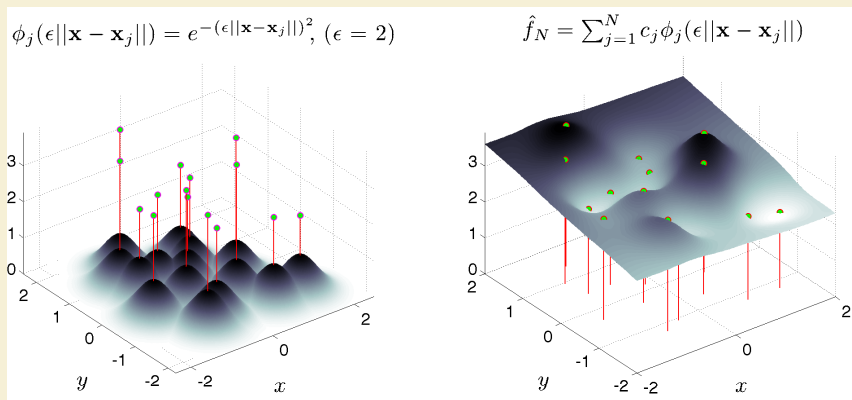


Figure 1.3: RBF interpolation using 15 translates of the Gaussian RBF with $\epsilon = 2$. One RBF is centered at each node in the domain. Linear combinations of these produce an interpolant over the domain passing through known function values.

of equations arises, with different degrees of sparsity, dependent on the chosen basis functions and how the various constraints are enforced. While we restrict the $\phi_j(x)$ to RBFs or various operators applied to the RBFs, we note that spectral methods, finite-element or spectral-element methods can be formulated in a similar way with different choices of basis functions. Of course, u can be a vector of unknown variables (\mathbf{c} then becomes a matrix).

In Table 1.3 we classify references according to their choice of collocation method and RBF interpolation type. There are three main categories of RBF interpolation; we list them in Table 1.2. The first is *Global* in the case that a single, large ($N \times N$) and dense matrix corresponding to globally supported RBFs is inverted; second, *Compact* if compactly supported RBFs are used to produce a single, large, but *sparse* matrix; and third, *Local* if compactly supported RBFs are used to produce many small but dense matrices with one corresponding to each collocation point. In all three cases the matrices are symmetric and with the correct choice of RBF they are at least conditionally positive definite. The final row of Table 1.3 considers literature on the RBF-FD method and is discussed in depth in Chapter 2.

We note that three types of collocation occur throughout the RBF literature: Kansa's unsymmetric collocation method [47, 48], Fasshauer's symmetric collocation method [20], and the Direct collocation method [23].

Interpolation Type	Dense/Sparse A	Dim(A) ($N_S \ll N$)	# of A^{-1}	RBF Support
Global	Dense	$N \times N$	1	Global
Compact	Sparse	$N \times N$	1	Compact
Local	Dense	$N_S \times N_S$	N	Global/Compact

Table 1.2: RBF interpolation types and properties, assuming a problem with N nodes.

We now turn to discussion of the benefits and shortcomings of each RBF method, before covering derivation of the methods.

1.1.1 Global RBF Methods

Kansa's method [47, 48] (a.k.a. unsymmetric collocation) was the first RBF method for PDEs, and is still the most frequently used method. The idea behind Kansa's method is that an approximate solution to the PDE can be found by finding an interpolant which satisfies the differential operator with zero residual at a set of *collocation points* (these coincide with the RBF centers). To find the interpolant, the differential equation is formulated as a two block (unsymmetric) linear system with: 1) the approximation of values at boundary points with boundary data only, and 2) the approximation of interior points by directly applying the differential operator. It was shown in [20, 41] that the unsymmetric linear system produced by Kansa's method does not guarantee non-singularity; although it is also noted that in practice singularities are rare encounters [52].

The second alternative for RBF collocation, is based on Hermite scattered data interpolation (see [87]). The so-called *Fasshauer* or *Symmetric Collocation* method ([20]) performs a change of basis for the interpolant by directly applying the differential operator to the RBFs. It then collocates using the same approach as Kansa's method [52, 73]. The resulting block structure of the linear system is symmetric and guaranteed to be non-singular [20]. In comparison to Kansa's method, the disadvantages of Fasshauer's method include: a) requirement of higher order differentiability of the basis functions (to satisfy double application of the differential operator) and b) the linear system is larger and more complex to form [21]. As [41] points out, the possible existence of a singularity in Kansa's method is not enough to justify the added difficulties of using Fasshauer's method.

The last collocation method, *Direct Collocation*, was introduced by Fedoseyev, Friedman and Kansa [23] and satisfies the differential operator on the interior and the boundary. Larsson and Fornberg [52] observe that this third method has a matrix structure similar to that found in Kansa's method; however, it is noted that the dimensions of the matrix blocks for each method differ. This is due to collocation constraints added for the differential operator applied to the boundary. Aside from the survey on RBF collocation presented by Larsson and Fornberg [52], no related work was found that applied, or investigated, this method further.

Both Kansa's method and Fasshauer's methods were shown in [19] to fit well in the generalized framework of pseudo-spectral methods with a subtle change in algorithm. While

collocation methods explicitly compute the coefficients for a continuous derivative approximation, their alternates, referred to in literature as RBF-pseudospectral (RBF-PS) methods, never explicitly compute the interpolant coefficients. Instead, a differentiation matrix (DM) is assembled and used to approximate derivates at the collocation points only [22]. Since most computational models are simply concerned with the solution at collocation points, the change to assemble DMs as in RBF-PS is organic.

Following the evolution of the RBF-PS algorithm, applications of global RBFs in the classic collocation sense (i.e., without the RBF-PS DMs) become impractical. This statement stems from the algorithmic complexity of each method. Global RBF methods result in full matrices [21]. The global collocation methods then scale on the order of $O(N^3)$ floating point operations (FLOPs) to solve for weighting coefficients on a given node layout, plus $O(N^2)$ to apply the weights for derivatives. If time-stepping is required, global collocation methods must recompute the time-dependent coefficients with additional cost dominated by $O(N^3)$ operations. RBF-PS methods have similar requirements for $O(N^3)$ operations to assemble the differentiation matrix and $O(N^2)$ to apply for derivatives. However, by avoiding time-dependent coefficients, RBF-PS methods only apply the differentiation matrix each time-step for $O(N^2)$ operations. As an aside, the $O(N^3)$ complexity for each method—typically due to an LU-decomposition, with subsequent forward- and back-solves—could be reduced. While not in mainstream use by the RBF community, [56] correctly points out that the use of iterative solvers could reduce complexity of preprocessing to the order of $O(N^2)$.

Hon et al. [42] employed Kansa's method to solve shallow water equations for Typhoon simulation. In [28], Flyer and Wright employed RBF-PS (Kansa method) for the solution of shallow water equations on a sphere. Their results show that RBFs allow for longer time steps with spectral accuracy. The survey [24] by Flyer and Fornberg showcases RBF-PS (Kansa) out-performing some of the best available methods in geosciences, namely: Finite Volume, Spectral Elements, Double Fourier, and Spherical Harmonics. When applied to problems such as transport on the sphere [27], shallow water equations [28], and 3D mantle convection[85], RBF-PS consistently required fewer time steps, and a fraction of the nodes for similar accuracy [24].

1.1.2 Compactly Support RBFs

Thus far, all cases of collocation and interpolation mentioned have assumed globally supported RBFs. While global RBFs are well-studied and have nice properties, a major limitation is the large, dense system that must be solved. One alternative to global support is to use a set of compactly supported RBFs (CSRBFs) that are defined as:

$$\phi(r) = \begin{cases} \varphi(r) & r \in [0, 1] \\ 0 & r > 1 \end{cases} \quad (1.1)$$

where a cut-off radius is defined past which the RBF (in this case $\varphi(r)$) has no influence on the interpolant. Note that the radius can be scaled to fit a desired support. Methods that leverage CSRBFs produce a global interpolation matrix that is *sparse* and therefore results in a system that is more efficiently assembled and solved with smaller memory requirements [21]. The actual complexity estimate of the CSRBF method depends on the sparsity of the

Method	RBF Interpolation Type		
	Global (Dense)	Compact (Sparse Global)	Local
Kansa's Method	[19, 24, 27, 28, 31, 36, 37, 41, 42, 47, 48, 52, 57, 69, 85]	[36, 80]	[16, 51, 78, 79]
Fasshauer's Method	[19, 20, 52]	[54]	[73, 74, 75]
Direct Collocation	[23, 52]		[9, 10, 14, 25, 26, 33, 34, 70, 71, 83, 84, 86]
RBF-FD	N/A	N/A	

Table 1.3: Classification of references based on choice of RBF interpolation types and method for solving PDEs. References may appear in multiple cells according to the breadth of their research.

problem as well as the ordering of the assembled system. Assuming $n \ll N$ where n represents the number of nodes in support, [90] lists the complexity as dominated by $O(N)$ for properly structured systems within MATLAB, and the investigation in [56] found $O(N^{1.5})$ consistent with the estimate provided by their choice of general sparse solver package. A multi-level CSRBDF method, introduced by Fasshauer [21], collocates solutions over multiple grid refinements to achieve reduced $O(N)$ complexity, but the method is plagued by poor convergence. We also note that in the context of CSRBFs, analogues to Kansa's method and Fasshauer's method are known by the names *radial point interpolation method (RPIM)* [80] and *radial point interpolation collocation method (RPICM)* [54], respectively. A more thorough survey of CSRBDF history can be found in [21, 43].

CSRBFs have attracted a lot of attention in applications. For example, in the field of dynamic surface and image deformation, compact support allows for local transformations which do not induce global deformation (see e.g., [13, 53, 88]).

1.1.3 Local RBF Methods

Around 2005, Šarler and Vertnik [78, 79] demonstrated that if compactly supported RBFs are chosen, the traditional global collocation matrix from Kansa's method, can be avoided altogether in favor of small localized collocation matrices defined for each node. Local collocation still faces possible ill-conditioning and singularities like global collocation, but make it easier to distribute computation across parallel systems. Also, the smaller linear systems can be solved with less conditioning issues. In [79], the authors consider 2D diffusion problems. Divo and Kassab [16] employ the method for Poisson-like PDEs including fluid flow and heat transfer. Kosec and Šarler [51] apply the same technique to solve coupled heat transfer and fluid flow problems.

In similar fashion, Stevens et al. [75] introduced a local version of Fasshauer’s method called *local Hermitian interpolation*. The authors have applied their method to 3D soil problems based on transient Richards’ equations [73, 74, 75].

1.1.4 Recent Advances in Conditioning

The most limiting factor in the success of RBF methods is not the complexity of the methods, nor the task of collocating the PDE. Rather, it is the support parameter, ϵ , and the dilemma one faces in the *Uncertainty Relation* [67]. Recall that as $\epsilon \rightarrow 0$ ill-conditioning increases, but the accuracy of the method also increases. Similarly, as the number of collocation points increases, so too does the ill-conditioning.

In response to this problem, Fornberg and Wright [31] presented the *Contour–Padé algorithm*, which allows for numerically stable computation of highly accurate interpolants for (very small) cases typically associated with ill-conditioning induced by nearly flat RBFs (i.e., $\epsilon \rightarrow 0$). Larsson and Fornberg [52] applied the algorithm to all three methods of collocation (Kansa’s, Fasshauer’s and Direct Collocation) with considerable gain in accuracy over solutions from classical second-order FD and a pseudospectral method. Note that currently, the Contour-Padé algorithm was only studied for global RBF interpolation, not for compact or local collocation methods.

The *RBF-QR* method, an alternative for numerically stable computation in the limit as $\epsilon \rightarrow 0$, was introduced by Fornberg and Piret [35] in context of a sphere, and later extended to planar 2D problems in [32]. The RBF-QR method is simple to implement (less than 100 lines of Matlab code), and it allows solution of large problems that are typically ill-conditioned. Fornberg, Larsson and Flyer [32] successfully applied RBF-QR on large problems with 6000 nodes for globally supported basis functions.

With these two algorithms, global RBF methods have overcome most ill-conditioning issues for small to mid-sized problems. Unfortunately, both Contour-Padé and RBF-QR fail for large problems. As the number of RBFs increases beyond a few thousand nodes it is impossible to avoid ill-conditioning of the extremely large interpolation matrix.

This reveals the benefit of local methods, which decrease the number of RBFs and ill-conditioning. However, in the limit as local stencil size increases to include all nodes in a domain, the local and global method are equivalent; thus it is known that local methods also suffer extreme ill-conditioning around 2000 nodes per stencil [71]. Although, to our knowledge, no applications of local methods require more than a few hundred nodes per local solution.

1.2 Comparison of RBF Methods

We now detail RBF methods for PDEs leading up to the derivation of RBF-FD.

Following [57], consider a PDE expressed in terms of a (linear) differential operator, \mathcal{L} :

$$\begin{aligned}\mathcal{L}u &= f && \text{on } \Omega \\ u &= g && \text{on } \Gamma\end{aligned}$$

where Ω is the interior of the physical domain, Γ is the boundary of Ω and f, g are known explicitly. In the case of a non-linear differential operator, a Newton’s iteration, or some

other method, can be used to linearize the problem (see e.g., [86]); of course, this increases the complexity of a single time step. Then, the unknown solution, u , which produces the observations on the right hand side can be approximated by an interpolant function u_ϕ expressed as a linear combination of radial basis functions, $\{\phi_j(x) = \phi(\|x - x_j\|)\}_{j=1}^N$, and polynomial functions $\{P_l(x)\}_{l=1}^M$:

$$u_\phi(x) = \sum_{j=1}^N \phi_j(x)c_j + \sum_{l=1}^M P_l(x)d_l, \quad P_l(x) \in \Pi_p^d \quad (1.2)$$

where $\phi_j(x) = \|x - x_j\|_2$ (Euclidean distance). The second sum represents a linear combination of polynomials that enforces zero approximation error when $u(x)$ is a polynomial of degree less than or equal to p . The variable d is the problem dimension (i.e., $u_\phi(x) \in \mathbb{R}^d$). To eliminate degrees of freedom for well-posedness, p should be greater than or equal to the order of the chosen RBF (see Table 1.1) [43]. Note that Equation 1.2 is evaluated at $\{x_j\}_{j=1}^N$ data points through which the interpolant is required to pass with zero residual. We refer to the x_j 's as *collocation points* (a.k.a. trial points), taken as the RBF centers. The test points, x , usually coincide with collocation points, although this is not a requirement.

To clarify the role of the polynomial part in Equation 1.2, it is necessary to put aside the PDE for the moment and consider only the problem of *scattered data interpolation* with Radial Basis Functions.

1.2.1 RBF Scattered Data Interpolation

Borrowing notation from [21, 43], we seek an interpolant of the form

$$f(x) = \sum_{j=1}^N \phi_j(x)c_j$$

where $f(x)$ is expressed as a scalar product between the unknown coefficient weights c_j and the radial basis functions $\phi_j(x)$.

To obtain the unknown coefficients, c_j , form a linear system in terms of the N RBF centers:

$$\begin{aligned} f(x) &= \sum_{j=1}^N c_j \phi_j(x) \quad \text{for } x = \{x_j\}_{j=1}^N \\ (\ f \) &= [\ \phi \] (\ c \) \end{aligned}$$

The invertibility of this system depends on the choice of RBF, so one typically chooses a function that is positive definite to avoid issues. It has been shown (see [21, 43]) that some choices of RBFs (e.g. multiquadratics and thin-plate splines [41]) are not positive definite and therefore there is no guarantee that the approximation is well-posed. A sufficient condition for well-posedness is that the matrix be *conditionally positive definite*. In [21], Fasshauer demonstrates that conditional positive definiteness is guaranteed when Equation 1.2 exactly reproduces functions of degree less than or equal m . For RBF scattered data interpolation

in one dimension, this can be achieved by adding a polynomial of order m with $M = \binom{m+1}{1}$ terms (e.g., x^0, x^1, \dots, x^m). In \mathbb{R}^d , $M = \binom{m+d}{d}$ [43], giving

$$\begin{aligned} \sum_{j=1}^N c_j \phi_j(x) + \sum_{l=1}^M d_l P_l(x) &= f(x), \quad P_l(x) \in \Pi_m^d \\ [\phi \quad P] \begin{pmatrix} c \\ d \end{pmatrix} &= (f) \end{aligned} \quad (1.3)$$

where the second summation (referred to as *interpolation conditions* [43]) ensures the minimum degree of the interpolant. Refer to Table 1.1 for a short list of recommended RBFs and minimally required orders of m . This document prefers the Gaussian RBF. Notice, in Equation 1.3, that the interpolation conditions add M new degrees of freedom, so we must provide M additional constraints to square the system. In this case:

$$\sum_{j=1}^N c_j P_l(x_j) = 0, \quad l = 1, \dots, M$$

or

$$P^T c = 0. \quad (1.4)$$

It is now possible again to write the interpolation problem as a complete linear system using Equations 1.3 and 1.4:

$$\underbrace{\begin{bmatrix} \phi & P \\ P^T & 0 \end{bmatrix}}_A \begin{pmatrix} c \\ d \end{pmatrix} = \begin{pmatrix} f \\ 0 \end{pmatrix} \quad (1.5)$$

Equation 1.5—typically a dense system except in the case of RBFs with compact support—can be solved efficiently via standard methods like LU-decomposition. With the coefficients, the interpolant can be sampled at any test points, $\{x_i\}_{i=1}^n$, by substitution into Equation 1.3:

$$\begin{aligned} f(x_i) &= \sum_{j=1}^N c_j \phi_j(x_i) + \sum_{l=1}^M d_l P_l(x_i) \\ &= \underbrace{[\phi \quad P]}_B \begin{pmatrix} c \\ d \end{pmatrix} \Big|_{x=x_i} \end{aligned} \quad (1.6)$$

1.2.2 Reconstructing Solutions for PDEs

In the next few subsections, we will consider collocation equations based on this general form:

$$\begin{aligned} \mathcal{L}u_\phi(x) &= f(x) \quad \text{on } \Omega \\ \mathcal{B}u_\phi(x) &= g(x) \quad \text{on } \Gamma \end{aligned}$$

where the methods presented below will apply the differential operators, \mathcal{L} and \mathcal{B} , to different choices of u_ϕ and different sets of collocation points. In many applications \mathcal{L} is chosen as a differential operator (e.g., $\frac{\partial}{\partial x}$, ∇ , ∇^2) and $\mathcal{B} = I$ (i.e. identity operator for Dirichlet boundary conditions) for PDEs. For RBF scattered data interpolation, $\mathcal{L} = I$. There are also applications where \mathcal{L} is a convolution operator (see e.g., [7, 8]) capable of smoothing/de-noising a surface reconstructed from point clouds.

For all the methods that follow a linear system is generated:

$$A_{\mathcal{L}} \begin{pmatrix} c \\ d \end{pmatrix} = \begin{pmatrix} f \\ 0 \end{pmatrix}$$

$$\begin{pmatrix} c \\ d \end{pmatrix} = A_{\mathcal{L}}^{-1} \begin{pmatrix} f \\ 0 \end{pmatrix}$$

where matrix $A_{\mathcal{L}}$ depends on the choice of collocation method. Once the linear system is solved, the value $u(x)$ is reconstructed at the test points following Equation 1.6:

$$\begin{aligned} u(x) &\approx [\phi \quad P] \begin{pmatrix} c \\ d \end{pmatrix} \Big|_{x=x_i} \\ &\approx BA_{\mathcal{L}}^{-1} \begin{pmatrix} f \\ 0 \end{pmatrix} \end{aligned} \tag{1.7}$$

Likewise, to obtain differential quantities we have:

$$\begin{aligned} \mathcal{L}u(x) &\approx [\phi_{\mathcal{L}} \quad P_{\mathcal{L}}] \begin{pmatrix} c \\ d \end{pmatrix} \Big|_{x=x_i} \\ &\approx B_{\mathcal{L}} A_{\mathcal{L}}^{-1} \begin{pmatrix} f \\ 0 \end{pmatrix} \end{aligned}$$

1.2.3 PDE Methods

Now, since $u_\phi(x)$ from Equation 1.2 cannot (in general) satisfy the PDE everywhere, we enforce the PDE at a set of collocation points, which are distributed over both the interior and the boundary. Again, these points do not necessarily coincide with the RBF centers, but it is convenient for this to be true in practice. Also, for each of the methods the choice of RBF can be either global, resulting in a large dense system, or compact, resulting in a large sparse system.

Kansa's Method

The first global RBF method for PDEs, *Kansa's method* [47, 48], collocates the solution through known values on the boundary, while constraining the interpolant to satisfy the PDE operator on the interior. This is equivalent to choosing u_ϕ according to Equation 1.2.

The resulting system is given by [57]; assuming that \mathcal{L} is a linear operator,

$$\mathcal{L}u_\phi(x_i) = \sum_{j=1}^N c_j \mathcal{L}\phi_j(x_i) + \sum_{l=1}^M d_l \mathcal{L}P_l(x_i) = f(x_i) \quad i = 1, \dots, n_I \quad (1.8)$$

$$\mathcal{B}u_\phi(x_i) = \sum_{j=1}^N c_j \mathcal{B}\phi_j(x_i) + \sum_{l=1}^M d_l \mathcal{B}P_l(x_i) = g(x_i) \quad i = n_I + 1, \dots, n \quad (1.9)$$

$$\sum_{j=1}^N c_j P_l(x_j) = 0 \quad l = 1, \dots, M \quad (1.10)$$

where n_I are the number of interior collocation points, with the number of boundary collocation points equal to $n - n_I$. First, observe that the differential operators are applied directly to the RBFs inside summations, rather than first solving the scattered data interpolation problem and then applying the operator to the interpolant. Second, since the basis functions are known analytically, it is possible (although sometimes painful) to derive $\mathcal{L}\phi$ (refer to [21] for RBF derivative tables); the same is true for the polynomials P_l .

We can now reformulate Kansa's method as the linear system:

$$\underbrace{\begin{bmatrix} \phi_{\mathcal{L}} & P_{\mathcal{L}} \\ \phi_{\mathcal{B}} & P_{\mathcal{B}} \\ P^T & 0 \end{bmatrix}}_{A_{\mathcal{L}}} \begin{pmatrix} c \\ d \end{pmatrix} = \begin{pmatrix} f \\ g \\ 0 \end{pmatrix} \quad (1.11)$$

where $\phi_{\mathcal{L}} = \mathcal{L}\phi$, $P_{\mathcal{L}} = \mathcal{L}P$ are the interior components (Equation 1.8), $\phi_{\mathcal{B}}$ and $P_{\mathcal{B}}$ are the boundary components (Equation 1.9), and $P^T = [P_{\mathcal{L}}^T \ P_{\mathcal{B}}^T]$ are constraints for both interior and boundary polynomial parts (Equation 1.10). From Equation 1.11 it should be clear why Kansa's method is also known as the *Unsymmetric* collocation method.

Recall that the matrix in Equation 1.11 has no guarantee of non-singularity [20]; however, singularities are rare in practice [52].

Fasshauer's Method

Fasshauer's method [20] addresses the problem of singularity in Kansa's method by assuming the interpolation to be Hermite. That is, it requires higher differentiability of the basis functions (they must be at least C^k -continuous if \mathcal{L} is of order k). Leveraging this assumption, Fasshauer's method chooses:

$$u_\phi(x_i) = \sum_{j=1}^{N_I} c_j \mathcal{L}\phi_j(x_i) + \sum_{j=N_I+1}^N c_j \mathcal{B}\phi_j(x_i) + \sum_{l=1}^M d_l P_l(x_i) \quad (1.12)$$

as the interpolant passing through collocation points. Note N_I is used here to specify the number of RBF centers in the interior of Ω . Here the interpolant is similar to Equation 1.2, but a change of basis functions is used for the expansion: $\mathcal{L}\phi_j(x)$ on the interior and $\mathcal{B}\phi_j(x)$ on the boundary.

Substituting Equation 1.12 into Equations 1.8-1.10 we get:

$$\begin{aligned} \sum_{j=1}^{N_I} c_j \mathcal{L}^2 \phi_j(x_i) + \sum_{j=N_I+1}^N c_j \mathcal{LB} \phi_j(x_i) + \sum_{l=1}^M d_l \mathcal{LP}_l(x_i) &= f(x_i) \quad i = 1, \dots, n_I \\ \sum_{j=1}^{N_I} c_j \mathcal{BL} \phi_j(x_i) + \sum_{j=N_I+1}^N c_j \mathcal{B}^2 \phi_j(x_i) + \sum_{l=1}^M d_l \mathcal{BP}_l(x_i) &= g(x_i) \quad i = n_I + 1, \dots, n \\ \sum_{j=1}^{N_I} c_j \mathcal{LP}_l(x_j) + \sum_{j=N_I+1}^N c_j \mathcal{BP}_l(x_j) &= 0 \quad l = 1, \dots, M \end{aligned} \quad (1.13)$$

which becomes the following:

$$\underbrace{\begin{bmatrix} \phi_{\mathcal{LL}} & \phi_{\mathcal{LB}} & P_{\mathcal{L}} \\ \phi_{\mathcal{BL}} & \phi_{\mathcal{BB}} & P_{\mathcal{B}} \\ P_{\mathcal{L}}^T & P_{\mathcal{B}}^T & 0 \end{bmatrix}}_{A_{\mathcal{L}}} \begin{pmatrix} c \\ d \end{pmatrix} = \begin{pmatrix} f \\ g \\ 0 \end{pmatrix} \quad (1.14)$$

Note that $\phi_{\mathcal{LL}}$ represents the first summation in Equation 1.13.

The symmetry of Fasshauer's (*symmetric collocation*) method is apparent in Equation 1.14. Likewise, it is clear that the symmetric method requires more storage and computation to solve compared to Kansa's method. However, based on the assumption that collocation points coincide with RBF centers, the symmetry reduces storage requirements by half.

Direct Collocation

In *Direct collocation* (see [23, 52], the interpolant is chosen as Equation 1.2 (the same as Kansa's method). However, the Direct method collocates both the interior and boundary operators at the boundary points:

$$\begin{aligned} \sum_{j=1}^N c_j \mathcal{L} \phi_j(x_i) + \sum_{l=1}^M d_l \mathcal{LP}_l(x_i) &= f(x_i) \quad i = 1, \dots, n \\ \sum_{j=1}^N c_j \mathcal{B} \phi_j(x_i) + \sum_{l=1}^M d_l \mathcal{BP}_l(x_i) &= g(x_i) \quad i = 1, \dots, n_B = n - n_I \\ \sum_{j=1}^N c_j P_l(x_j) &= 0 \quad l = 1, \dots, M \end{aligned} \quad (1.15)$$

Reformulating as a linear system we get:

$$\begin{bmatrix} \phi_{\mathcal{L}} & P_{\mathcal{L}} \\ \phi_{\mathcal{B}} & P_{\mathcal{B}} \\ P^T & 0 \end{bmatrix} \begin{pmatrix} c \\ d \end{pmatrix} = \begin{pmatrix} f \\ g \\ 0 \end{pmatrix} \quad (1.16)$$

While the final system in Equation 1.16 is structured the same as Kansa's method (Equation 1.11), careful inspection of the index i in Equations 1.8 and 1.15 reveals that Direct collocation produces a larger system.

RBF-PS

The extension of global collocation to traditional pseudo-spectral form was introduced by Fasshauer in [19]. Dubbed RBF-PS, the method utilizes the same logic from Kansa's and Fasshauer's collocation methods to form matrix $A_{\mathcal{L}}$ (i.e., $A_{\mathcal{L}}$ can be either Equation 1.11 or 1.14). However, RBF-PS subtly assumes the solution, $u(x)$, is only required at collocation points (i.e., $\{x_i\} = \{x_c\}$) [19, 21]. Then, extending Equation 1.7, RBF-PS gives:

$$\begin{aligned} u(x) &= (BA_{\mathcal{L}}^{-1}) \begin{pmatrix} f \\ 0 \end{pmatrix} \\ &= D_{\mathcal{L}}^T \begin{pmatrix} f \\ 0 \end{pmatrix}. \end{aligned} \quad (1.17)$$

where $D_{\mathcal{L}}$ is a discrete differentiation matrix (DM) for the operator \mathcal{L} . Here, $D_{\mathcal{L}}$ is independent of the function $f(x)$ and is assembled by solving the system:

$$D_{\mathcal{L}} = A_{\mathcal{L}}^{-T} B^T \quad (1.18)$$

An LU-decomposition ($O(N^3)$) in preprocessing with forward- and back-solves ($O(N^2)$) are fitting to efficiently solve the multiple RHS system[21, 85].

Since matrix $D_{\mathcal{L}}$ is independent of functions $u(x)$ and $f(x)$, the matrix requires update only if the RBF centers move—a compelling benefit for time-dependent problems on stationary nodes. The complexity of RBF-PS for time-dependent solutions is then reduced to a matrix-vector multiply ($O(N^2)$) for each time-step. In contrast, classic RBF collocation methods also construct LU factors of $A_{\mathcal{L}}^{-1}$ in preprocessing, but delay application of forward- and back-solves to acquire time-dependent weighting coefficients at each time-step. This is then followed by the pre-multiply of B (i.e., additional $O(N^2)$) to complete the time-step.

1.2.4 Local Methods

Another trend in RBF methods is to use compact support to produce local linear systems defined at each collocation point. Examples of this include [78, 79] for Kansa's method, [73, 74, 75] for Fasshauer's method. To our knowledge no one has considered local Direct collocation. Also, instead of specifying a cut-off radius for RBF support, some authors specify the exact stencil size (i.e., number of neighboring points to include); see e.g., [16, 73].

After observing the general structure of the symmetric and unsymmetric collocation methods above, it is necessary only to present the symmetric (i.e. Fasshauer's) local method and note that in the unsymmetric case certain blocks will be zero allowing the system to shrink.

The formula for the interpolant local to the (k) -th collocation point (i.e., RBF center) is given by:

$$u_{\phi}^{(k)}(x_i) = \sum_{j(k)=1}^{N_I} c_j^{(k)} \mathcal{L} \phi_j(x_i) + \sum_{j(k)=N_I+1}^{N_S} c_j^{(k)} \mathcal{B} \phi_j(x_i) + \sum_{l=1}^M d_l^{(k)} P_l(x_i)$$

where N_S represents the number of points that defines the local stencil; N is possibly a function of the cut-off radius in the RBF, N_I is the number of interior stencil points (those

points of the stencil that lie in the interior of Ω). The index j is a function of the stencil center k allowing the system to include a local neighborhood of stencil points.

This results in a linear system with similar structure to the global collocation problem, but the dimensions are much smaller:

$$\underbrace{\begin{bmatrix} \phi_{\mathcal{L}\mathcal{L}} & \phi_{\mathcal{L}\mathcal{B}} & P_{\mathcal{L}} \\ \phi_{\mathcal{B}\mathcal{L}} & \phi_{\mathcal{B}\mathcal{B}} & P_{\mathcal{B}} \\ P_{\mathcal{L}}^T & P_{\mathcal{B}}^T & 0 \end{bmatrix}}_{A_{\mathcal{L}}} \begin{pmatrix} c^{(k)} \\ d^{(k)} \\ 0 \end{pmatrix} = \begin{pmatrix} f \\ g \\ 0 \end{pmatrix} \quad (1.19)$$

Solving this system gives an interpolant locally defined around the stencil center. Note that approximating the PDE solution $u(x)$ requires finding the stencil center nearest x , then using the local interpolant for that stencil. Since interpolation is local (i.e., $c_j^{(k)}$'s are unique to each RBF center), reconstructing the derivatives with Equation 1.8 is limited to an inner product for each center rather than the matrix-vector grouping possible with global RBFs. This approach decomposes the problem into smaller and more manageable parts. However, because the interpolants are local, there is no notion of global continuity/smoothness of the solution.

Chapter 2

Introduction to RBF-FD

While most of the literature surrounding RBFs for PDEs involves collocation, an alternative method does exist: RBF-generated Finite Differences (RBF-FD). RBF-FD is a hybrid of RBF scattered data interpolation and Finite Difference (FD) stencils.

The idea behind FD stencils is to express various derivative operators as a linear combination of known functional values in the neighborhood of a point where an approximation to the derivative operator is desired. Common approximations such as upwind differencing, center differencing, and higher order approximations are of this form. Similarly, RBF-FD combines functional values, but it does so in a more generalized sense than standard FD stencils. While one is typically restricted to regular meshes and often symmetric stencils in classic FD, RBF-FD allows for stencils with irregular placement and number of nodes.

The choice to study RBF-FD within this work is motivated by two factors. First, RBF-FD represents one of the latest developments within the RBF community. The method was first introduced in 2000 [77], but is only now showing signs it has obtained the critical-mass following necessary for the method's use in large-scale scientific models. Our goal throughout the dissertation has been to scale RBF-FD to complex problems on high resolution meshes, and to lead the way for its adoption in high performance computational geophysics. Graphics Processing Units (GPUs), introduced in Chapter ??, are many-core accelerators capable of general purpose, embarrassingly parallel computations. GPUs represent the latest trend in high performance computing, where compute nodes are commonly supplemented by one or more accessory GPUs. Our effort leads the way for application of RBF-FD in an age when compute nodes with attached accelerator boards will be key to breaching the exa-scale computing barrier [3]. Second, RBF-FD inherits many of the positive features from global and local collocation schemes, but sacrifices others for reduced computational complexity and potentially increased parallelism. The method is sufficiently young, so many opportunities for investigation still remain. Key challenges lie in the choice of grid, the choice of stencil, whether or not to change the support as a function of the stencil, how to guaranty the stability of the differentiation operator after discretization, etc.

2.1 Background

RBF-generated Finite Differences (RBF-FD) were first introduced by Tolstykh in 2000 [77], but it was the simultaneous, yet independent, efforts in [70], [76], [84] and [9] that gave the method its real start. The RBF-FD method (and the RBF-HFD, “Hermite” equivalent [86]) is similar in concept to classical finite-differences (FD), but differs in that the underlying differentiation weights are exact for RBFs rather than polynomials. The method contrasts with global RBF methods in the sense that it does not collocate the PDE. Instead, RBF-FD provides a set of generalized FD weights representing the discrete differential operator for a small neighborhood of nodes.

RBF-FD share many advantages with global RBF methods, like the ability to function without an underlying mesh, easily extend to higher dimensions and afford large time steps; however spectral accuracy is lost. Other advantages of RBF-FD include lower computational complexity together with high-order accuracy (6th to 10th order accuracy is common). As in FD, increasing the stencil size, n , increases the order accuracy of the approximation. While not a panacea for PDEs, the method is simple to code, easily extensible to higher dimensions, and powerful in its ability to avoid singularities introduced by the coordinate systems that might impact other methods (see e.g., [27, 34]).

In some ways, RBF-FD and global RBF methods are plagued by the same difficulties. For example, as the number of nodes in the stencil increases, so too does the ill-conditioning of the linear systems to be inverted. Similarly, the most accurate weights occur when $\epsilon \rightarrow 0$, but values in that regime beget additional ill-conditioning problems—a recurrence of the *Uncertainty Relation* [67]. One key difference in the multiple independent RBF-FD origins was that Wright [84] focused on bypassing ill-conditioning of RBF-FD and investigated its behavior in the limit as $\epsilon \rightarrow 0$ by means of the Contour-Padé algorithm.

Given N total nodes in the domain, N linear systems, each of size $(n+1) \times (n+1)$, are solved to calculate the differentiation weights for derivatives at each node. With $n \ll N$, the RBF-FD preprocessing complexity is dominated by $O(N)$; significantly lower than the global RBF or RBF-PS methods ($O(N^3)$). Additionally, the cost per time step is also dominated by $O(N)$.

RBF-FD have been successfully employed for a variety of problems including Hamilton-Jacobi equations [9], convection-diffusion problems [10, 73], incompressible Navier-Stokes equations [11, 70], transport on the sphere [34], and the shallow water equations [26]. Shu et al. [71] compared the RBF-FD method to Least Squares FD (LSFD) in context of 2D incompressible viscous cavity flow, and found that under similar conditions, the RBF-FD method was more accurate than LSFD, but the solution required more iterations of an iterative solver. RBF-FD was applied to Poisson’s equation in [83]. Chandhini and Sanyasiraju [10] studied it in context of 1D and 2D, linear and non-linear, convection-diffusion equations, demonstrating solutions that are non-oscillatory for high Reynolds number, with improved accuracy over classical FD. An application to Hamilton-Jacobi problems [9], and 2D linear and non-linear PDEs including Navier-Stokes equations [70] have all been considered.

2.2 The RBF-generated Finite Differences Method

The RBF-FD method is similar to classical Finite Differences in that RBF-FD allows derivatives of a function $u(x)$ to be approximated by weighted combinations of n function values in a small neighborhood (i.e., $n \ll N$) around a *center* node, x_c . That is:

$$\mathcal{L}u(x) |_{x=x_c} \approx \sum_{j=1}^n c_j u(x_j) \quad (2.1)$$

where $\mathcal{L}u$ again represents a differential quantity over $u(x)$ (e.g., $\mathcal{L} = \frac{\partial}{\partial x}$). We refer to the n nodes around x_c as a *stencil* with size n . While not required, in practice one considers stencils to include the center, x_c , plus the $n - 1$ nearest neighboring nodes. The definition of “nearest” depends the choice of distance metric; here, Euclidean distance ($\|x - x_c\|_2$) is preferred.

Generally, one typically needs derivatives at every node in the discretized domain to solve PDEs. To achieve this with RBF-FD, stencils are generated around each node in the domain. Stencils need not have the same size (n), but this is assumed here for simplicity in discussion. Furthermore, the number of stencils need not match the number of nodes in the domain, but this is also assumed.

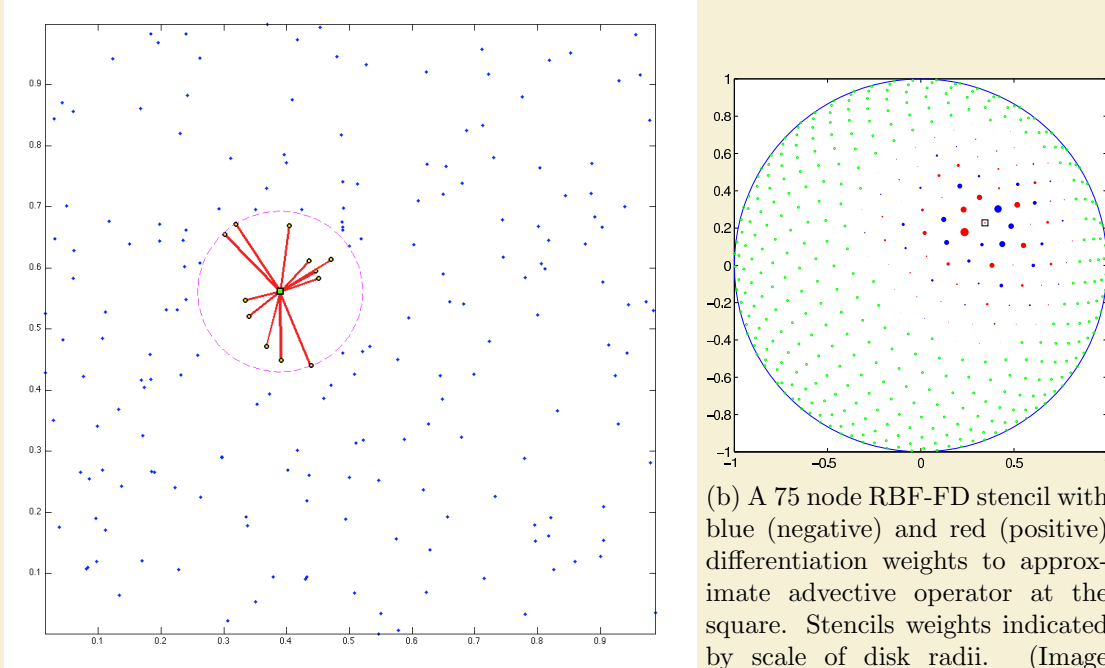


Figure 2.1: Examples of stencils computable with RBF-FD

Figure 2.1 provides two examples of RBF-FD stencils. First, Figure 2.1a illustrates a single stencil of size $n = 13$ in a domain of randomly distributed nodes. The stencil center,

x_c , is represented by a green square, with the 12 neighboring nodes connected via red edges. The purple circle, the minimum covering circle for the stencil, demonstrates that the stencil contains only the 12 nearest neighbors of the center node. In Figure 2.1b, a larger RBF-FD stencil of size $n = 75$ on the unit sphere is shown as red and blue disks surrounding the center represented as a square. Green disks are nodes outside of the stencil. The radii and color of the red and blue disks represent the magnitude and alternating sign of coefficients, c_j , determined to calculate a derivative quantity at the stencil center.

2.2.1 Stencil Weights

To approximate $\mathcal{L}u(x)$, one requires the stencil *weights* (coefficients), c_j . Stencil weights are a discrete representation of the differential operator at the stencil center and may vary by node location (e.g., nodes at the boundary are usually governed by another operator, \mathcal{B}). Weights are obtained by enforcing that they be exact within the space spanned by the RBFs centered at stencil nodes (i.e., $\phi_j(x) = \phi(\epsilon\|x - x_j\|_2)$; an RBF centered at x_j). Various studies [26, 29, 34, 86] show that better accuracy is achieved when the interpolant can exactly reproduce a constant, p_0 , such that

$$\mathcal{L}\phi_i(x) |_{x=x_c} = \sum_{j=1}^n c_j \phi_j(x_i) + c_{n+1} p_0 \quad \text{for } i = 1, 2, \dots, n$$

with $\mathcal{L}\phi_i$ provided by analytically applying the differential operator to the RBF. Assuming $p_0 = 1$, the constraint $\sum_{i=1}^n c_i = \mathcal{L}p_0|_{x=x_c} = 0$ completes the system:

$$\begin{aligned} \begin{bmatrix} \phi_1(x_1) & \phi_2(x_1) & \cdots & \phi_n(x_1) & 1 \\ \phi_1(x_2) & \phi_2(x_2) & \cdots & \phi_n(x_2) & 1 \\ \vdots & \ddots & \ddots & \vdots & \vdots \\ \phi_1(x_n) & \phi_2(x_n) & \cdots & \phi_n(x_n) & 1 \\ 1 & 1 & \cdots & 1 & 0 \end{bmatrix} \begin{pmatrix} c_1 \\ c_2 \\ \vdots \\ c_n \\ c_{n+1} \end{pmatrix} &= \begin{pmatrix} \mathcal{L}\phi_1(x) |_{x=x_c} \\ \mathcal{L}\phi_2(x) |_{x=x_c} \\ \vdots \\ \mathcal{L}\phi_n(x) |_{x=x_c} \\ 0 \end{pmatrix} \\ \begin{bmatrix} \phi & P \\ P^T & 0 \end{bmatrix} \begin{pmatrix} c_{\mathcal{L}} \\ d_{\mathcal{L}} \end{pmatrix} &= \begin{pmatrix} \phi_{\mathcal{L}} \\ 0 \end{pmatrix}. \end{aligned} \tag{2.2}$$

The choice of \mathcal{L} can be any linear operator. As an example, if \mathcal{L} is the identity operator, then the above procedure leads to RBF-FD weights for interpolation. If $\mathcal{L} = \frac{\partial}{\partial x}$, one obtains the weights to approximate the first derivative in x . Refer to [21] for a table of commonly used RBF derivatives. Section 2.2.4 provides a list of derivatives used in this work.

The small $(n+1) \times (n+1)$ system in Equation 2.2 is dense, and is solved at a cost of $O(n^3)$ floating point operations (FLOPs) using direct methods like LU-decomposition. The resulting stencil weights, $c_{\mathcal{L}} = \{c_j\}_{j=1}^n$ can be substituted into Equation 6.3 for the derivative approximation at x_c . Coefficient c_{n+1} ($d_{\mathcal{L}} = c_{n+1}$), included in the solution of Equation 2.2, is of no use and discarded once the system has been solved.

Based on the choice of support parameter, ϵ , the Equation 2.2 may suffer problems with conditioning. In such cases, stable methods like Contour–Padé [84] or RBF-QR [14, 33] may be preferred.

2.2.2 Differentiation Matrix

Note that Equation 2.2 resolves the weights only for the stencil x_c . The small system solve is repeated N times—once for each stencil—to obtain a total of $N \times n$ stencil weights.

For PDEs, it is common practice to assemble a *differentiation matrix* (DM); a discrete representation of the PDE operator on the domain. Given the set of nodes in the domain $\{x_k\}_{k=1}^N$, the c -th row of the DM represents the discrete PDE operator for the stencil centered at node x_c with stencil nodes $\{x_j\}_{j=1}^n$:

$$\begin{aligned}\mathcal{L}u(x) &\approx D_{\mathcal{L}}u \\ D_{\mathcal{L}}^{(c,k)} &= \begin{cases} c_j & x_k = x_j \\ 0 & x_k \neq x_j \end{cases}\end{aligned}$$

where (c, k) represents the (row, column) index of $D_{\mathcal{L}}$ and vector $u = \{u(x_k)\}_{k=1}^N$. Equation 6.3 can be rewritten as:

$$\mathcal{L}u(x) |_{x=x_c} \approx D_{\mathcal{L}}^{(c)} u .$$

In the solution of PDEs the DMs are utilized in explicit and implicit modes. Here explicit implies evaluating the matrix-vector multiply to get derivative values, u' , from explicitly known vector of solution values u :

$$u' = D_{\mathcal{L}}u \quad (2.3)$$

whereas implicit solves for unknown u :

$$D_{\mathcal{L}}u = f \quad (2.4)$$

An example RBF-FD DM is illustrated in Figure 2.2. In this example, assume operator $\mathcal{L} = \frac{\partial}{\partial x}$ is approximated at all N stencil centers of an arbitrary domain. RBF-FD weights assemble the rows of the differentiation matrix, D_x . On each row, weights are indicated by blue dots. The sparsity of rows reflects the subset of $\{x_k\}_{k=1}^N$ included in corresponding stencils of size n . On the right hand side, discrete derivative values $\frac{du}{dx}$ are approximated at all stencil centers.

Differentiation matrices are assembled at a cost of $O(n^3 N)$ FLOPs. However, since the goal of RBF-FD is to keep stencil neighborhoods small ($n \ll N$), the cost of assembly scales as $O(N)$. Furthermore, RBF-FD weights are independent of function values ($u(x)$) and rely only on stencil node locations. The implications of this are as profound as in the context RBF-PS for time-dependent PDEs: the stencil weights are constant so long as the nodes are stationary. Thus, the DM assembly is part of a one-time preprocessing step.

The sparsity exhibited by the DM in Figure 2.2 is typical for RBF-FD due to $n \ll N$. Best practices dictate that the DMs be stored in a compressed sparse storage format to retain only non-zeros and their corresponding indices in memory.

2.2.3 Multiple Operators

In many cases, multiple derivatives (e.g., $\mathcal{L} = \nabla^2$, $\frac{\partial}{\partial x}$, $\frac{\partial}{\partial y}$, etc.) are required at stencil centers. This is common, for example, when solving coupled PDEs. For RBF-FD, acquiring

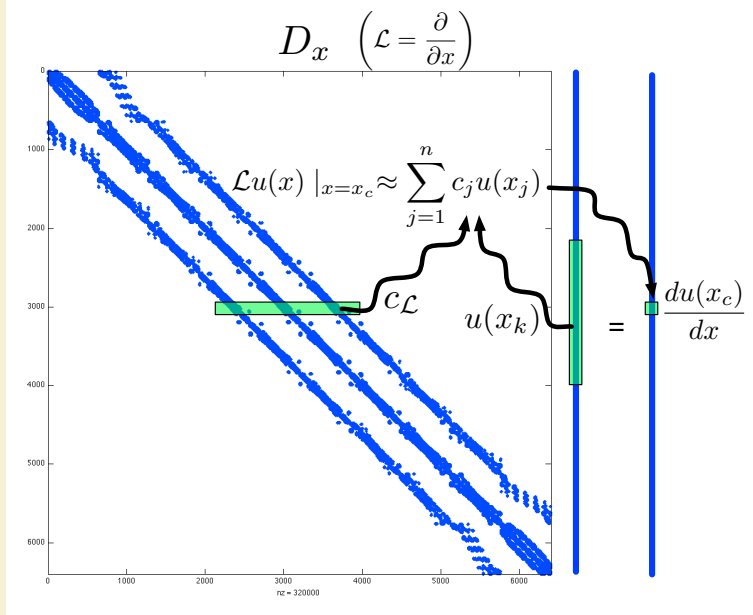


Figure 2.2: Differentiation matrix D_x is applied to the solution values $u(x)$ to obtain derivative approximations, $\frac{du}{dx}$.

weights for each additional operator can be both straight-forward and computationally efficient. For each change of differential operator, observe that only the RHS of Equation 2.2 is modified. Thus, new operators amount to extending Equation 2.2 to solve

$$\begin{bmatrix} \phi & P \\ P^T & 0 \end{bmatrix} \begin{bmatrix} c_{\nabla^2} & c_x & c_y & \cdots \\ d_{\nabla^2} & d_x & d_y & \cdots \end{bmatrix} = \begin{bmatrix} \phi_{\nabla^2} & \phi_x & \phi_y & \cdots \\ 0 & 0 & 0 & \cdots \end{bmatrix}.$$

where multiple sets of weights (c_{∇}, c_x, c_y) solved simultaneously. This dense, symmetric, multiple RHS linear system is considered ideal by linear algebra packages, and many highly optimized routines exist to solve them (e.g., LAPACK “dgesv”) [1].

2.2.4 Weight Operators

In the course of this work we work with a variety of PDEs. This section enumerates a list of relevant operators and their corresponding equations for the RHS of Equation 2.2. Whenever possible the general form of $\mathcal{L}\phi$ is provided; otherwise the Gaussian RBF ($\phi(r) = e^{-(\epsilon r)^2}$) is assumed.

First and Second Derivatives ($\frac{1}{r} \frac{\partial \phi}{\partial r}, \frac{\partial^2 \phi}{\partial r^2}$)

The following are used in subsequent derivatives:

$$\begin{aligned} \frac{1}{r} \frac{d}{dr} \phi(r) &= -2\epsilon^2 \phi(r) \\ \frac{\partial^2 \phi}{\partial r^2} &= \epsilon^2 (-2 + 4(\epsilon r)^2) \phi(r) \end{aligned}$$

Cartesian Gradient (∇)

The first derivatives in Cartesian coordinates $(\frac{\partial}{\partial x}, \frac{\partial}{\partial y}, \frac{\partial}{\partial z})$ are produced via the chain rule:

$$\begin{aligned}\frac{\partial \phi}{\partial x} &= \frac{\partial r}{\partial x} \frac{\partial \phi}{\partial r} = \frac{(x - x_j)}{r} \frac{\partial \phi}{\partial r} \\ \frac{\partial \phi}{\partial y} &= \frac{\partial r}{\partial y} \frac{\partial \phi}{\partial r} = \frac{(y - y_j)}{r} \frac{\partial \phi}{\partial r} \\ \frac{\partial \phi}{\partial z} &= \frac{\partial r}{\partial z} \frac{\partial \phi}{\partial r} = \frac{(z - z_j)}{r} \frac{\partial \phi}{\partial r}\end{aligned}$$

where $\frac{\partial \phi}{\partial r}$ for the Gaussian RBFs is given above.

Cartesian Laplacian (∇^2)

Fasshauer [21] provides the general form of ∇^2 in 2D as:

$$\nabla^2 = \frac{\partial^2}{\partial r^2} \phi(r) + \frac{1}{r} \frac{\partial}{\partial r} \phi(r)$$

For Gaussian RBFs in particular we have the following operators:

- 1D:

$$\nabla^2 = \epsilon^2 (-2 + 4(\epsilon r)^2) \phi(r)$$

- 2D:

$$\nabla^2 = \epsilon^2 (-4 + 4(\epsilon r)^2) \phi(r)$$

- 3D:

$$\nabla^2 = \epsilon^2 (-6 + 4(\epsilon r)^2) \phi(r)$$

which all fit $\nabla^2 = \frac{\partial^2}{\partial r^2} \phi(r) + \frac{d-1}{r} \frac{\partial}{\partial r} \phi(r)$ for dimension d .

Laplace-Beltrami (Δ_S) on the Sphere

The ∇^2 operator can be represented in spherical polar coordinates for \mathbb{R}^3 as:

$$\nabla^2 = \underbrace{\frac{1}{r} \frac{\partial}{\partial r} \left(r^2 \frac{\partial}{\partial r} \right)}_{\text{radial}} + \underbrace{\frac{1}{r^2} \Delta_S}_{\text{angular}}$$

where Δ_S is the Laplace-Beltrami operator—i.e., the Laplacian operator constrained to the surface of the sphere. This form nicely illustrates the separation of components into radial and angular terms.

In the case of PDEs solved on the unit sphere, there is no radial term, so we have:

$$\nabla^2 \equiv \Delta_S. \tag{2.5}$$

Although this originated in the spherical coordinate system, [85] introduced the following Laplace-Beltrami operator for the surface of the sphere:

$$\Delta_S = \frac{1}{4} \left[(4 - r^2) \frac{\partial^2 \phi}{\partial r^2} + \frac{4 - 3r^2}{r} \frac{\partial \phi}{\partial r} \right],$$

where r is the Euclidean distance between nodes of an RBF-FD stencil and is independent of our choice of coordinate system.

Constrained Gradient ($P_x \cdot \nabla$) on the Sphere

Following [26, 28], the gradient operator can be constrained to the sphere with this projection matrix:

$$P = I - \mathbf{x}\mathbf{x}^T = \begin{pmatrix} (1 - x_1^2) & -x_1x_2 & -x_1x_3 \\ -x_1x_2 & (1 - x_2^2) & -x_2x_3 \\ -x_1x_3 & -x_2x_3 & (1 - x_3^2) \end{pmatrix} = \begin{pmatrix} P_{x_1} \\ P_{x_2} \\ P_{x_3} \end{pmatrix} \quad (2.6)$$

where \mathbf{x} is the unit normal at the stencil center.

The direct method of computing RBF-FD weights for the projected gradient for $\mathbf{P} \cdot \nabla$ is presented in [28]. When solving for the weights, we apply the projection on the right hand side of our small linear system. We let $\mathbf{x} = (x_1, x_2, x_3)$ be the stencil center, and $\mathbf{x}_k = (x_{1,k}, x_{2,k}, x_{3,k})$ indicate an RBF-FD stencil node.

Using the chain rule, and assumption that

$$r(\mathbf{x}_k - \mathbf{x}) = \|\mathbf{x}_k - \mathbf{x}\| = \sqrt{(x_{1,k} - x_1)^2 + (x_{2,k} - x_2)^2 + (x_{3,k} - x_3)^2},$$

we obtain the unprojected gradient of ϕ as

$$\nabla \phi(r(\mathbf{x}_k - \mathbf{x})) = \frac{\partial r}{\partial \mathbf{x}} \frac{\partial \phi(r(\mathbf{x}_k - \mathbf{x}))}{\partial r} = -(\mathbf{x}_k - \mathbf{x}) \frac{1}{r(\mathbf{x}_k - \mathbf{x})} \frac{\partial \phi(r(\mathbf{x}_k - \mathbf{x}))}{\partial r}.$$

Applying the projection matrix gives

$$\begin{aligned} \mathbf{P} \nabla \phi(r(\mathbf{x}_k - \mathbf{x})) &= -(\mathbf{P} \cdot \mathbf{x}_k - \mathbf{P} \cdot \mathbf{x}) \frac{1}{r(\mathbf{x}_k - \mathbf{x})} \frac{\partial \phi(r(\mathbf{x}_k - \mathbf{x}))}{\partial r} \\ &= -(\mathbf{P} \cdot \mathbf{x}_k - 0) \frac{1}{r(\mathbf{x}_k - \mathbf{x})} \frac{\partial \phi(r(\mathbf{x}_k - \mathbf{x}))}{\partial r} \\ &= -(I - \mathbf{x}\mathbf{x}^T)(\mathbf{x}_k) \frac{1}{r(\mathbf{x}_k - \mathbf{x})} \frac{\partial \phi(r(\mathbf{x}_k - \mathbf{x}))}{\partial r} \\ &= \begin{pmatrix} x\mathbf{x}^T \mathbf{x}_k - x_k \\ y\mathbf{x}^T \mathbf{x}_k - y_k \\ z\mathbf{x}^T \mathbf{x}_k - z_k \end{pmatrix} \frac{1}{r(\mathbf{x}_k - \mathbf{x})} \frac{\partial \phi(r(\mathbf{x}_k - \mathbf{x}))}{\partial r} \end{aligned}$$

Thus, we directly compute the weights for $P_x \cdot \nabla$ using these three RHS in Equation 2.2:

$$\begin{aligned} P \frac{\partial}{\partial x_1} &= (x_1 \mathbf{x}^T \mathbf{x}_k - x_{1,k}) \frac{1}{r(\mathbf{x}_k - \mathbf{x})} \frac{\partial \phi(r(\mathbf{x}_k - \mathbf{x}))}{\partial r} \Big|_{\mathbf{x}=\mathbf{x}_j} \\ P \frac{\partial}{\partial x_2} &= (x_2 \mathbf{x}^T \mathbf{x}_k - x_{2,k}) \frac{1}{r(\mathbf{x}_k - \mathbf{x})} \frac{\partial \phi(r(\mathbf{x}_k - \mathbf{x}))}{\partial r} \Big|_{\mathbf{x}=\mathbf{x}_j} \\ P \frac{\partial}{\partial x_3} &= (x_3 \mathbf{x}^T \mathbf{x}_k - x_{3,k}) \frac{1}{r(\mathbf{x}_k - \mathbf{x})} \frac{\partial \phi(r(\mathbf{x}_k - \mathbf{x}))}{\partial r} \Big|_{\mathbf{x}=\mathbf{x}_j} \end{aligned}$$

Hyperviscosity Δ^k for Stabilization

When explicitly solving hyperbolic equations, differentiation matrices encode convective operators of the form

$$D = \alpha \frac{\partial}{\partial \lambda} + \beta \frac{\partial}{\partial \theta} \quad (2.7)$$

The convective operator, discretized through RBF-FD, has eigenvalues in the right half-plane causing the method to be unstable [26, 34]. Stabilization of the RBF-FD method is achieved through the application of a hyperviscosity filter to Equation (2.7) [34]. By using Gaussian RBFs, $\phi(r) = e^{-(\epsilon r)^2}$, the hyperviscosity (a high order Laplacian operator) simplifies to

$$\Delta^k \phi(r) = \epsilon^{2k} p_k(r) \phi(r) \quad (2.8)$$

where k is the order of the Laplacian and $p_k(r)$ are multiples of generalized Laguerre polynomials that are generated recursively ([34]):

$$\begin{cases} p_0(r) &= 1, \\ p_1(r) &= 4(\epsilon r)^2 - 2d, \\ p_k(r) &= 4((\epsilon r)^2 - 2(k-1) - \frac{d}{2})p_{k-1}(r) - 8(k-1)(2(k-1)-2+d)p_{k-2}(r), \end{cases} \quad k = 2, 3, \dots$$

where d is the dimension of the problem. The application of hyperviscosity in Chapter 5, utilizes the operator as a filter to shift eigenvalues and stabilize advection equations on the surface of the unit sphere. In that case, $d = 2$ is assumed since individual RBF-FD stencils can be viewed as (nearly) lying on a plane. For small N , the diameter of the stencil may not be sufficiently small compared to the radius of the sphere, and hyperviscosity might not work as advertised.

In the case of parabolic and hyperbolic PDEs, hyperviscosity is added as a filter to the right hand side of the evaluation. For example, at the continuous level, the equation solved takes the form

$$\frac{\partial u}{\partial t} = -\mathcal{L}u + Hu, \quad (2.9)$$

where \mathcal{L} is the PDE operator, and H is the hyperviscosity filter operator. Applying hyperviscosity shifts all the eigenvalues of L (the discrete form of \mathcal{L}) to the left half of the complex plane. This shift is controlled by k , the order of the Laplacian, and a scaling parameter γ_c , defined by

$$H = \gamma \Delta^k = \gamma_c N^{-k} \Delta^k.$$

It was found in [26], and verified in our own application, that $\gamma = \gamma_c N^{-k}$ provides stability and good accuracy for all values of N considered here. It also ensures that the viscosity vanishes as $N \rightarrow \infty$ [26]. In general, the larger the stencil size, the higher the order of the Laplacian. This is attributed to the fact that, for convective operators, larger stencils treat a wider range of modes accurately. As a result, the hyperviscosity operator should preserve as much of that range as possible. The parameter γ_c must also be chosen with care and its sign depends on k (for k even, γ_c will be negative and for k odd, it will be positive). If γ_c is too large, the eigenvalues move outside the stability domain of our time-stepping scheme and/or eigenvalues corresponding to lower physical modes are not left intact, reducing the accuracy of our approximation. If γ_c is too small, eigenvalues remain in the right half-plane [26, 34].

2.3 Implementation

This section provides an overview of how one implements RBF-FD. Consider Algorithm 2.1. The algorithm is partitioned into two phases: preprocessing and application. The complexity of each phase depends on the choice of algorithms/method utilized for each task.

Preprocessing encompasses tasks such as grid setup/generation, stencil generation and stencil weight calculations. As output from these tasks one expects one or more DMs representing the discrete differential operators. Assuming the grid nodes do not move, the DMs remain constant for the duration of the second phase. Additionally, DMs can be loaded from disk on subsequent runs to effectively bypass the cost of all preprocessing.

Algorithm 2.1 A High-Level View of RBF-FD

Preprocessing:

```

 $\{x\}_{j=1}^N = \text{GenerateGrid}()$ 
for  $j = 1$  to  $N$  do
    Stencil  $\{S_{j,i}\}_{i=1}^n = \text{QueryNeighbors}(x_j)$ 
end for
for  $j = 1$  to  $N$  do
     $\{w_{j,i}\}_{i=1}^n = \text{SolveForWeights}(\{S_j\})$ 
     $D_{\mathcal{L}}^{(j)} = \text{AssembleDM}(\{w_j\})$ 
end for

```

Application:

```

 $t = t_{min}$ 
while  $t < t_{max}$  do
     $\{u'\} = \text{SolvePDE}(D_{\mathcal{L}}, \{u\})$ 
     $\{u\} = \text{UpdateSolution}(\{u\}, \{u'\}, \Delta t)$ 
     $t += \Delta t$ 
end while

```

The constructed DMs are applied in the Application phase to solve a PDE either explicitly or implicitly. Note that regardless of the explicit or implicit method, this phase reduces to a Sparse Matrix-Vector Multiply (SpMV) within the SolvePDE step. For explicit solutions, SolvePDE computes the SpMV in Equation 2.3. In the implicit case, SolvePDE must invert the DM in Equation 2.4 via a direct or iterative linear system solve. Although it is not mandatory, many PDE solutions are time-dependent and require some time advancement scheme. The time-scheme could be as simple as an Euler update with a single call to SolvePDE. Higher order methods (e.g., Runge-Kutta, Adams-Bashforth, etc.) may require multiple applications of the DM, with the outputs weighted and combined within UpdateSolution.

Tuning the performance of the RBF-FD method requires one to focus on the Application phase. This is especially true for time-dependent PDEs where an increase in grid size results in proportional increase in the number time-steps. The recurring cost of computing an SpMV each time-step quickly amortizes the one-time cost of preprocessing.

On the other hand, preprocessing tasks have more impact on accuracy, stability and conditioning of the method. As each of these properties improve, the overall time to solution can decrease thanks to larger stable time-steps, smaller grid size, and fewer iterations in

iterative linear system solves.

Here we discuss various design decisions in implementing the preprocessing tasks for RBF-FD and consider potential impacts on performance (if any). Chapter 3 will discuss Application and SpMV performance in more detail.

2.3.1 Grid

An implementation of RBF-FD begins with the grid. The method has no requirement for structured grids, or for a well-refined mesh/lattice that limits connectivity between nodes. It operates both on structured grids and random point clouds; although, the choice of grid does impact the accuracy of the method. This freedom to function on domains of any shape, dimension, and granularity is a major selling point for RBF-FD and often impossible for many other PDE methods.

The choice of grid is only relevant to the extent that it impacts the connectivity between nodes in stencils. Connectivity translates to non-zeros in rows of the DMs, so the various grid distributions result in a number of sparsity patterns. For all other intents and purposes, the choice of grid is only pertinent to ensure consistency with the PDEs to solve.

In the course of this work, we applied RBF-FD to a number of PDEs and grid distributions. Here we focus on the subset utilized in Chapters 5 and ???. This subset is chosen for two reasons: a) to easily construct refinements in 2D/3D for consistent benchmarking and convergence studies, and b) to verify our solutions against existing methods.

Regular Grid

For basic debugging and benchmarking purposes the most natural choice is to start with a regular or Cartesian grid. Equally spaced nodes in multiple dimensions are simple to generate. Additionally, refinements—for convergence tests—are direct subsamples.

In theory, RBF-FD functions the same whether nodes are uniformly spaced or random. However, regular grids do not fully exercise advantages that RBF-FD has over other methods with its ability to operate on scattered nodes.

Maximum Determinant Nodes

In Chapter 5 we verify our RBF-FD implementation by solving PDEs on the unit sphere. For consistency with respect to related investigations (e.g., [30, 34, 35]), we choose the Maximum Determinant (MD) node sets [72, 82].

MD node sets were introduced to the RBF community due to their success in spherical harmonics interpolation, where the seemingly irregular node distributions gain an order of magnitude accuracy compared to regular looking (Minimum Energy) node distributions [82]. RBF interpolation tends to reproduce spherical harmonics interpolants on the sphere when $\epsilon \rightarrow 0$, and RBF methods have been shown to benefit similarly from a subtle irregularity in node locations [35].

The MD node files are available for download on the authors' web site (<http://web.maths.unsw.edu.au/~rsw/Sphere>), and range in size from $N = 4$ up to $N=27,556$ nodes on the sphere. Figure 2.3 plots the $N = 4096$ node set to illustrate the irregularity in distribution. Node sets greater than $N=27,556$ are not available. Unlike regular grids, each

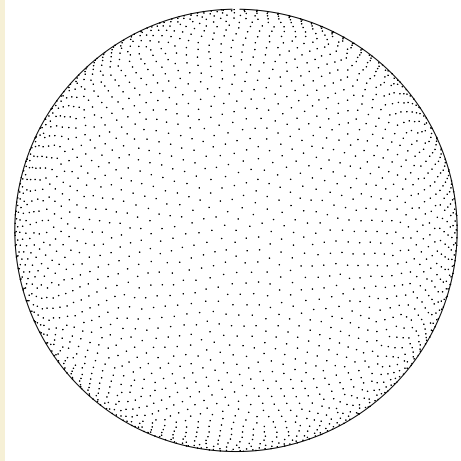


Figure 2.3: Example of $N = 4096$ maximum determinant (MD) node sets on the unit sphere.

MD node set is a refinement of the sphere, but not a subdivision, so extending beyond $N=27,556$ nodes would require complete regeneration.

Centroidal Voronoi Tessellations

While the MD nodes suffice for verification against related work, our objective is to scale RBF-FD to problem sizes never attempted. To this end, we sought approximately regular grids on the sphere on the order of hundreds of thousands and even millions of nodes. To this end we leverage Spherical Centroidal Voronoi Tessellations (SCVTs) to generate approximately regular node distributions on the sphere [18, 81].

SCVTs come with a sense of “optimality” in node locations due to energy minimizing properties [18]. The process to generate SCVTs involves constructing a Voronoi diagram, computing the mass centroids for each Voronoi partition, and updating node locations to the mass centroids projected onto the sphere. After a number of iterations the nodes coincide with the projected mass centroids and a converged SCVT is produced. In most large-scale applications, this iterative process leverages a probabilistic Lloyd’s method, where integrals to compute mass centroids are approximated through random sampling [18, 81]. While SCVTs in theory converge to a regular node distribution, the probabilistic nature of the centroid calculation introduces irregularities in distribution reminiscent of MD nodes.

Figure 2.4 provides an example SCVT grid with $N=100,000$ nodes. On the left, the full sphere; on the right, a close-up of the same node set. The close-up perspective clearly demonstrates the random artifacts/scarring of irregularly distributed nodes. For benchmarking purposes we use node sets $N=100,000$, $N=500,000$ and $N=1,000,000$ generated by the SCVT library from [81]. These SCVT grids are publicly available from: https://github.com/bollig/sphere_grids.git.

2.3.2 Generating Stencils

After a grid is either generated or loaded stencils must be generated by querying the n nearest neighbors to each $\{x_j\}_{j=1}^N$. Brute force searching for neighbors—computing the

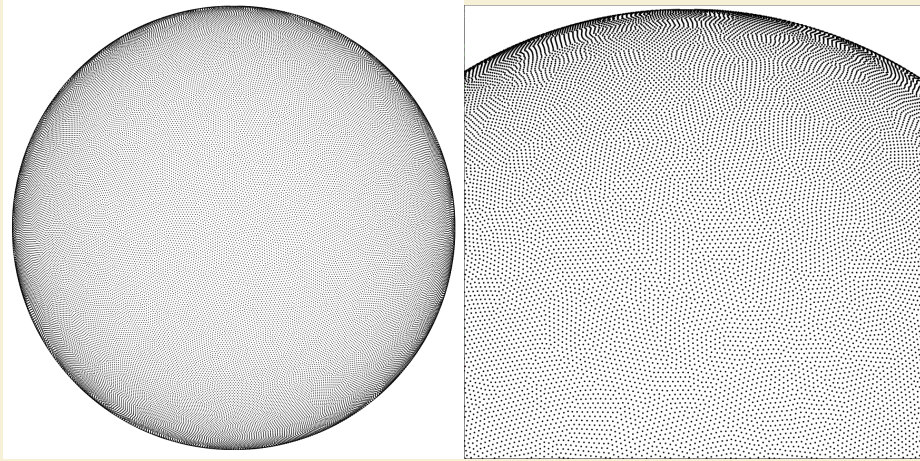


Figure 2.4: (Left) $N=100,000$ Spherical Centroidal Voronoi Tessellation nodes. (Right) Close-up of the same $N=100,000$ nodes to illustrate the irregularities in the grid.

distance between every pair of nodes and then selecting the n nearest—is discouraged due to its $O(N^2)$ complexity. Alternatively, it is common practice in the RBF community to construct k D-Trees to decrease the cost of queries (e.g., [21, 26, 34]).

This can be done efficiently using neighbor query algorithms or spatial partitioning data-structures such as Locality Sensitive Hashing (LSH) and k D-Tree. Different query algorithms often have a profound impact on the DM structure and memory access patterns. We choose a Raster (ijk) ordering LSH algorithm [?] leading to the matrix structure in Figures 4.4 and 4.5. While querying neighbors for each stencil is an embarrassingly parallel operation, the node sets used here are stationary and require stencil generation only once. Efficiency and parallelism for this task has little impact on the overall run-time of tests, which is dominated by the time-stepping. We preprocess node sets and generate stencils serially, then load stencils and nodes from disk at run-time. In contrast to the RBF-FD view of a static grid, Lagrangian/particle based PDE algorithms promote efficient parallel variants of LSH in order to accelerate querying neighbors at each time-step [39, 61].

Many algorithms exist to query the k -nearest neighbors (equivalently all nodes in the minimum/smallest enclosing circle). Some algorithms overlay a grid similar to Locality Sensitive Hashing and query such as... [?].

RBF-FD is designed to handle irregular node distributions. Therefore, it is not essential that stencils contain only nearest neighbors. Instead, one can acquire the *approximate nearest neighbors*. Figure ?? demonstrates a case where a does not contain all nearest neighbors. As illustrated in the Figure, the ANN stencil and true nearest neighbor stencil differ by one node. THis is not dire

KDTree

Hashing

Hashing, shown in Figure ?? overlays a regular grid. This is equivalent to an axis aligned bounding box AABB, with refinement. In other words, we form a quad-tree in 2D, an octree in 3D. The neighbor query starts with the cell in which x_c resides. Since we use

an axis aligned bounding box, this cell index is easily calculated given the coordinate and number of subdivisions in each dimension. Once the cell index is resolved, the stencil is populated by taking the n nearest neighbors from within the current cell. If the cell does not contain sufficient number of nodes to fill the stencil, the search for neighbors expands to include the cells immediately adjoining the center cell, taking only the nearest nodes in the provided cells. The search continues to expand outward in a rasterized circle/sphere until n is satisfied. This search is considered approximate because it can happen that a true nearest neighbor would lie in a cell that is not included in the rasterized circle, and other nodes are substituted from the far reaches of the discretized grid.

The complexity of the method is still higher than the more efficient implementations used by Lagrangian methods, but as demonstrated in Figure ?? the savings are significant. Generating stencils for RBF-FD is a preprocessing cost, so we do not dedicate an excessive amount of attention to this algorithm. However, a few ideas that would improve: hilbert ordering, choose AABB resolution based on N not user parameters, faster sorting, GPU implementation

Savings

To demonstrate the savings in choice of stencil generation method, we provide Figure ??.

2.3.3 Approximate Nearest Neighbor (ANN) Query

RBF-FD operates on general node distributions. Historically, stencils are uniform in size (n) and generated by selecting the $(n - 1)$ true nearest neighbors to a node x_c . This is a k -NN query.

Alternative queries are possible: ball query and approximate nearest neighbor. The approximate is of particular interest because nodes closest to the stencil will always be selected, whereas the nodes further away have minimal influence so swapping out can't hurt. The justification in altering the selection is for reduced complexity in neighbor queries.

For example, in general brute force is inefficient. The author of [21] queries n nearest neighbors for a compact-support RBF partition of unity example with a k -D tree. In [26, 34] a k -D Tree is leveraged for all neighbor queries for RBF-FD.

In our work in [6] an alternative to k -D tree was leveraged, based loosely on Locality Sensitive Hashing.

Rather than iterate through all N nodes to find the true neighbors, or step through a k -D tree in something like $O(\log N)$ that requires extra built-out, ANN allows us to use a set of nodes that satisfy

k -D Tree

Most of the RBF community leverages the k -D tree, due to its low computational complexity for querying neighbors and its wide availability as standalone software in the public domain (e.g., matlab central has a few implementations for download, and the MATLAB Statistics Toolbox includes an efficient k -D Tree).

The complexity of assembling the tree is

The Matlab central k -D Tree is MEX compiled and efficient. We integrated the standalone C++ code into our library.

While the k -D Tree functions well for queries, its downfall is a large cost in preprocessing to build the tree. For moving nodes, such as in Lagrangian schemes, this cost is prohibitively high. In an attempt to reduce the cost, lagrangian schemes introduced approximate nearest neighbor queries based on

Approximate nearest neighbors will be nearly balanced. We observe that RBF-FD functions as well on stencils of true nearest neighbors as it does on approximate nearest neighbors.

Sparsity

To quantify the sparsity of a Differentiation Matrix we consider the ratio of non-zeros ($N * n$) to total elements in the matrix (N^2). For example, a problem of size $N = 10,000$ with stencil size $n = 31$ has a ratio of 0.0031 and is 99.69% empty.

2.3.4 On Choosing the Right ϵ

If solving for the weights directly (i.e., inverting Equation 2.2), one must carefully choose ϵ to prevent ill-conditioning. Numerous attempts exist in literature to provide “good” functions for ϵ based on node spacing, h , stencil size n , etc. In general, the values provided are particular to the specific problem and/or grid under consideration. No fool-proof method exists to select the support parameters, so the prospect of hassle-free application of the RBF-FD method is still out of reach.

Modern algorithms introduced in the last couple years provide methods for acquiring weights. Contour-Padé, RBF-QR, and RBF-GA are all options for weights corresponding to the $\epsilon \rightarrow 0$. These methods appear to resolve many issues including conditioning of implicit systems for more accurate solutions [14] [?]

In this work, we have attempted a variety of scalings on ϵ . We forego discussion of these attempts since they are outside our current scope of investigation. In the end, we find that the most effective method for choosing ϵ was to adopt the approach introduced in [26], wherein ϵ is expressed as a function of the number of nodes N and desired mean condition number, $\bar{\kappa}_A$.

The optimal ϵ for general node distributions is out of the scope of this research and not necessary for our purposes. For now we assume that nodes are more or less regularly distributed, either via some algorithm such as Lloyd’s method to create Centroidal Voronoi Tessellations, repelling springs (distmesh), minimum energy or minimum determinant, or some other algorithm. Except in cases where convergence on PDE solutions can not be attained via RBF-FD, we find that a direct solve for RBF-FD weights is sufficient. To a certain extent, this work considers parallelization of the method so it does not matter if our weights are precise or not.

Chapter 3

A Distributed Multi-GPU RBF-FD Implementation

Parallel implementations of RBF methods currently rely on parallel domain decomposition. Depending on the implementation, domain decomposition not only accelerates solution procedures, but can decrease the ill-conditioning that plague all global RBF methods [16]. The ill-conditioning is reduced if each domain is treated as a separate RBF domain, and the boundary update is treated separately. Domain decomposition methods for RBFs were introduced by Beatson et al. [4] in the year 2000 as a way to increase problem sizes into the millions of nodes.

Divo and Kassab [16] used a domain decomposition method with artificial subdomain boundaries for their implementation of a local collocation method [16]. Subdomains are processed independently. The derivative values at artificial boundary points are averaged to maintain global consistency of physical values. Their implementation was designed for a 36 node cluster, but benchmarks and scalability tests are not provided.

Kosec and Šarler [51] used OpenMP to parallelize coupled heat transfer and fluid flow problems on a single workstation. Their test cases used local collocation, explicit time-stepping and Neumann boundary conditions. A speedup factor of 1.85x over serial execution was achieved by executing on two CPU cores; no results from scaling tests were provided.

Stevens et al. [75] mention a parallel implementation under development, but no document is available yet.

Additional RBF implementations are discussed at the end of this chapter in the context of parallel co-processing with the GPU.

In this work, we will add to the above experiences, with the added twist of incorporating an implementation on the GPU (see later chapters).

RBFs on GPU work: [68, 69] (global), [89] (compact)

We are investigating optimizations that target both GPUs and Phi cards for a class of numerical methods based on Radial Basis Functions (RBFs) to solve Partial Differential Equations. RBF methods are increasingly popular across disciplines due to their low complexity, natural ability to function in higher dimension with minimal requirements for an underlying mesh, and high-order—in many cases, spectral—accuracy. RBF methods can be viewed as generalizations of many traditional methods such as Finite Difference and Finite Element to allow for truly unstructured grids. This generalization allows one to reuse many

of the same techniques (e.g., sparse matrices, iterative solvers, domain decompositions, etc.) to efficiently obtain solutions. The variety of hardware available on Cascade will help us establish a clear argument in the choice of accelerator type and resolve the dilemma between choosing Phi vs GPU for our method. Since RBFs generalize other methods, our results should have broad reaching impact to answer similar questions for related methods.

With the generalization of RBF-FD derivative computation formulated as a sparse matrix multiplication, we can consider the various sparse formats provided by CUSP and ViennaCL.

Consider the performance of the problem given

- All stencils with uniform size
- All stencils with non-uniform size

What is the optimal choice of sparse container? How do the sparse containers compare in performance to each other, and to our custom kernels? What can we conclude?

Compare formats:

- JAD
- ELL
- HYB
- COO
- CSR
- DIA

How is communication overlap handled with each format?

Conclude: sparse containers allow increased efficiency compared to our custom kernels.
The custom kernels compete with CSR and COO.

Chapter 4

Parallel Solvers

Parallel solution of PDEs in a distributed computing environment requires three design decisions [65]. First, partitioning the domain and distributing work across compute nodes requires knowledge of *neighboring processors* with which communication will occur. Intelligent partitioning impacts load balancing on processors and the computation to communication ratio; imbalanced computation can cause excessive delay per iteration as processors wait to receive information. Second, one must decide what information each processor is able to access regarding node information, solution values, etc and establish index mappings that translate between a processor's local context and the global problem. In situations where processors are not aware of all nodes/solution values in the global domain, the index mappings are essential to maintaining solution consistency at each time-step. Last but not least, each processor can re-order nodes locally in an effort to improve solver efficiency and local system conditioning. Node ordering also allows us to minimize data transfer between CPU and GPU.

Parallelization of the RBF-FD method is achieved at two levels. First, the physical domain of the problem—in this case, the unit sphere—is partitioned into overlapping sub-domains, each handled by a different CPU process. All CPUs operate independently to compute/load RBF-FD stencil weights, run diagnostic tests and perform other initialization tasks. A CPU computes only weights corresponding to stencils centered in the interior of its partition. After initialization, CPUs continue concurrently to solve the PDE. Communication barriers ensure that the CPUs execute in lockstep to maintain consistent solution values in regions where partitions overlap. The second level of parallelization offloads time-stepping of the PDE to the GPU. Evaluation of the right hand side of Equation (2.9) is data-parallel: the solution derivative at each stencil center is evaluated independently of the other stencils. This maps well to the GPU, offering decent speedup even in unoptimized kernels. Although the stencil weight calculation is also data-parallel, we assume that in this context that the weights are precomputed and loaded once from disk during the initialization phase.

4.1 On the use of libraries for parallel solvers

Since our focus within this work is to lay the foundation for parallel computing with RBF-FD, we have made several simplifying assumptions in our code design. Libraries like PETsc, Hypre, Trilinos and Deal.ii distribute sparse matrix operations in similar fashion to our approach. When work initially began on this dissertation, none of these competing libraries contained support for the GPU. PETsc is currently developing support for the GPU, but we have not had the chance to consider it yet.

Our codebase began as a prototype demonstrating the feasibility of RBF-FD operating on the GPU. Starting from the perspective of RBF-FD as a Lagrangian method with stationary nodes, the code was developed as N independent dot products of weights and solution values to approximate derivatives. Weights were stored linearly in memory, with the solution values read randomly. On the GPU, stencils were evaluated independently by threads, or shared by a warp of threads. Operating on stencils in this way implied that GPU kernels were to be hand written, tuned and optimized.

Much later, our perspective evolved to see derivative approximation and time-stepping as sparse matrix operations. This opened new possibilities for optimization and allowed us to forego hand optimization and fine-tuning of GPU kernels. With all of the effort put into optimizing sparse operations within libraries like CUSP [5], ViennaCL [63] and even the Nvidia provided CUSPARSE [?], formulating the problem in terms of sparse matrix operations allows us to quickly prototype on the GPU and leverage all of the optimizations available within the third party libraries.

In the most recent version of ViennaCL a set of auto-tuning options were introduced. We have not investigated these options, but the idea is that they would only improve the efficiency of our code.

4.2 Partitioning

For ease of development and parallel debugging, partitioning is initially assumed to be linear within one physical direction (typically the x -direction). Figure 4.1 illustrates a partitioning of $N = 10,201$ nodes on the unit sphere onto four CPUs. Each partition, illustrated as a unique color, represents set \mathcal{G} for a single CPU. Alternating representations between node points and interpolated surfaces illustrates the overlap regions where nodes in sets \mathcal{O} and \mathcal{R} (i.e., nodes requiring MPI communication) reside. As stencil size increases, the width of the overlap regions relative to total number of nodes on the sphere also increases.

Author's Note: Q: what is the percentage overlap for n ? $\frac{1}{2}n^{\frac{1}{d}}$ gives depth into neighbor since n is uniformly sampled we expect a cube shape. (SHould be literature on this...no?)

The linear partitioning in Figure 4.1 was chosen for ease of implementation. Communication is limited for each processor to left and right neighbors only, which simplifies parallel debugging. This partitioning, however, does not guarantee properly balanced computational work-loads. *Author's Note: Update w/ ParMETIS* Other partitionings of the sphere exist but are not studied here because this paper's focus is neither on efficiency nor on selecting a partitioning strategy for maximum accuracy. Examples of alternative approaches include a cubed-sphere [44] or icosahedral geodesic grid [62], which can evenly balance the computational load across partitions. Other interesting partitionings can be generated with

software libraries such as the METIS [49] family of algorithms, capable of partitioning and reordering directed graphs produced by RBF-FD stencils.

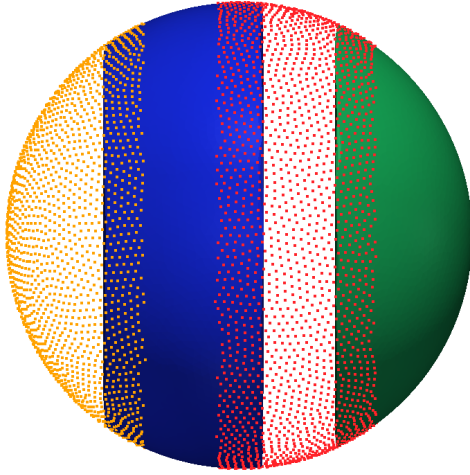


Figure 4.1: Partitioning of $N = 10,201$ nodes to span four processors with stencil size $n = 31$.

4.3 Local node ordering

After partitioning, each CPU/GPU is responsible for its own subset of nodes. To simplify accounting, we track nodes in two ways. Each node is assigned a global index, that uniquely identifies it. This index follows the node and its associated data as it is shuffled between processors. In addition, it is important to treat the nodes on each CPU/GPU in an identical manner. Implementations on the GPU are more efficient when node indices are sequential. Therefore, we also assign a local index for the nodes on a given CPU, which run from 1 to the maximum number of nodes on that CPU.

It is convenient to break up the nodes on a given CPU into various sets according to whether they are sent to other processors, are retrieved from other processors, are permanently on the processor, etc. Note as well, that each node has a home processor since the RBF nodes are partitioned into multiple domains without overlap. Table 4.1, defines the collection of index lists that each CPU must maintain for both multi-CPU and multi-GPU implementations.

Figure 4.2 illustrates a configuration with two CPUs and two GPUs, and 9 stencils, four on CPU1, and five on CPU2, separated by a vertical line in the figure. Each stencil has size $n = 5$. In the top part of the figures, the stencils are laid out with blue arrows pointing to stencil neighbors and creating the edges of a directed adjacency graph. Note that the connection between two nodes is not always bidirectional. For example, node 6 is in the stencil of node 3, but node 3 is not a member of the stencil of node 6. Gray arrows point to stencil neighbors outside the small window and are not relevant to the following discussion, which focuses only on data flow between CPU1 and CPU2. Since each CPU is responsible for the derivative evaluation and solution updates for any stencil center, it is

\mathcal{G}	: all nodes received and contained on the CPU/GPU g
\mathcal{Q}	: stencil centers managed by g (equivalently, stencils computed by g)
\mathcal{B}	: stencil centers managed by g that require nodes from another CPU/GPU
\mathcal{O}	: nodes managed by g that are sent to other CPUs/GPUs
\mathcal{R}	: nodes required by g that are managed by another CPU/GPU

Table 4.1: Sets defined for stencil distribution to multiple CPUs

clear that some nodes have a stencil with nodes that are on a different CPU. For example, node 8 on CPU1 has a stencil comprised of nodes 4,5,6,9, and itself. The data associated with node 6 must be retrieved from CPU2. Similarly, the data from node 5 must be sent to CPU2 to complete calculations at the center of node 6.

The set of all nodes that a CPU interacts with is denoted by \mathcal{G} , which includes not only the nodes stored on the CPU, but the nodes required from other CPUs to complete the calculations. The set $\mathcal{Q} \in \mathcal{G}$ contains the nodes at which the CPU will compute derivatives and apply solution updates. The set $\mathcal{R} = \mathcal{G} \setminus \mathcal{Q}$ is formed from the set of nodes whose values must be retrieved from another CPU. For each CPU, the set $\mathcal{O} \in \mathcal{Q}$ is sent to other CPUs. The set $\mathcal{B} \in \mathcal{Q}$ consists of nodes that depend on values from \mathcal{R} in order to evaluate derivatives. Note that \mathcal{O} and \mathcal{B} can overlap, but differ in size, since the directed adjacency graph produced by stencil edges is not necessarily symmetric. The set $\mathcal{B} \setminus \mathcal{O}$ represents nodes that depend on \mathcal{R} but are not sent to other CPUs, while $\mathcal{Q} \setminus \mathcal{B}$ are nodes that have no dependency on information from other CPUs. The middle section Figure 4.2 lists global node indices contained in \mathcal{G} for each CPU. Global indices are paired with local indices to indicate the node ordering internal to each CPU. The structure of set \mathcal{G} ,

$$\mathcal{G} = \{\mathcal{Q} \setminus \mathcal{B}, \mathcal{B} \setminus \mathcal{O}, \mathcal{O}, \mathcal{R}\}, \quad (4.1)$$

is designed to simplify both CPU-CPU and CPU-GPU memory transfers by grouping nodes of similar type. The color of the global and local indices in the figure indicate the sets to which they belong. They are as follows: white represents $\mathcal{Q} \setminus \mathcal{B}$, yellow represents $\mathcal{B} \setminus \mathcal{O}$, green indices represent \mathcal{O} , and red represent \mathcal{R} .

The structure of \mathcal{G} offers two benefits: first, solution values in \mathcal{R} and \mathcal{O} are contiguous in memory and can be copied to or from the GPU without the filtering and/or re-ordering normally required in preparation for efficient data transfers. Second, asynchronous communication allows for the overlap of communication and computation. This will be considered as part of future research on algorithm optimization. Distinguishing the set $\mathcal{B} \setminus \mathcal{O}$ allows the computation of $\mathcal{Q} \setminus \mathcal{B}$ while waiting on \mathcal{R} .

Author's Note: The local index set is ordered as QmB, BmO, O, R

Author's Note: Domain boundary nodes appear at beginning of the list

When targeting the GPU, communication of solution or intermediate values is a four step process:

1. Transfer \mathcal{O} from GPU to CPU
2. Distribute \mathcal{O} to other CPUs, receive R from other CPUs
3. Transfer \mathcal{R} to the GPU

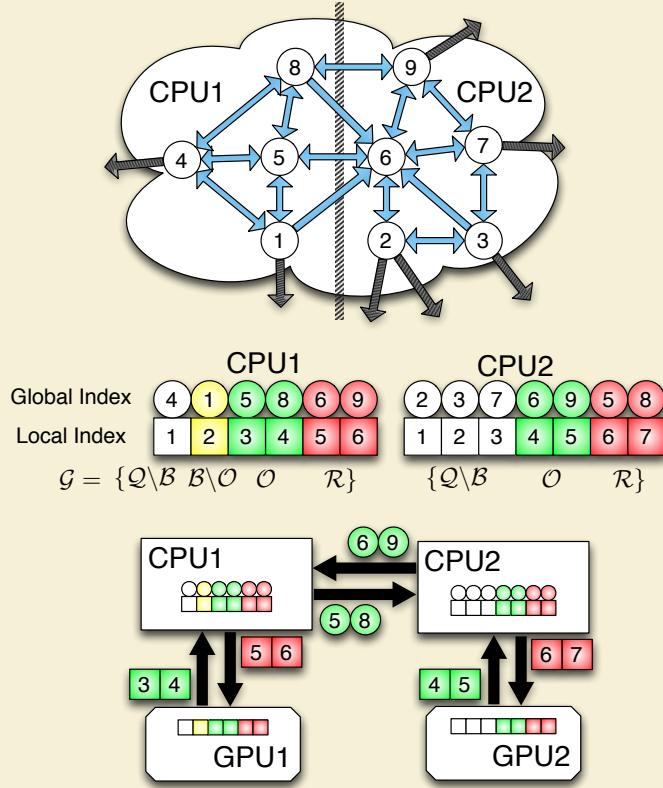


Figure 4.2: Partitioning, index mappings and memory transfers for nine stencils ($n = 5$) spanning two CPUs and two GPUs. Top: the directed graph created by stencil edges is partitioned for two CPUs. Middle: the partitioned stencil centers are reordered locally by each CPU to keep values sent to/received from other CPUs contiguous in memory. Bottom: to synchronize GPUs, CPUs must act as intermediaries for communication and global to local index translation. Middle and Bottom: color coding on indices indicates membership in sets from Table 4.1: $\mathcal{Q} \setminus \mathcal{B}$ is white, $\mathcal{B} \setminus \mathcal{O}$ is yellow, \mathcal{O} is green and \mathcal{R} is red.

4. Launch a GPU kernel to operate on \mathcal{Q}

The data transfers involved in this process are illustrated at the bottom of Figure 4.2. Each GPU operates on the local indices ordered according to Equation (4.1). The set \mathcal{O} is copied off the GPU and into CPU memory as one contiguous memory block. The CPU then maps local to global indices and transfers \mathcal{O} to other CPUs. CPUs send only the subset of node values from \mathcal{O} that is required by the destination processors, but it is important to note that node information might be sent to several destinations. As the set \mathcal{R} is received, the CPU converts back from global to local indices before copying a contiguous block of memory to the GPU.

This approach is scalable to a very large number of processors, since the individual processors do not require the full mapping between RBF nodes and CPUs.

4.4 Two level parallelism

Our current implementation assumes that we are computing on a cluster of CPUs, with one GPU attached to each CPU. The CPU maintains control of execution and launches kernels on the GPU that execute in parallel. Under the OpenCL standard [50], a tiered memory hierarchy is available on the GPU with *global device memory* as the primary and most abundant memory space. The memory space for GPU kernels is separate from the memory available to a CPU, so data must be explicitly copied to/from global device memory on the GPU.

- How to copy to/from GPU
- Where are the synchronization points (lockstep and overlapping)

Author's Note: [The basic primitives necessary to parallelize our problems: SpMV, AXPY and](#)

4.4.1 Explicit Solvers

Our implementation leverages the GPU for acceleration of the standard fourth order Runge-Kutta (RK4) scheme. Nodes are stationary, so stencil weights are calculated once at the beginning of the simulation, and reused in every iteration. To avoid the cost of calculating stencil weights each time a test case is run, they are written to disk and loaded from file on subsequent runs. There is one set of weights computed for each new grid. Ignoring code initialization, the cost of the algorithm is simply the explicit time advancement of the solution.

Figure 4.3 summarizes the time advancement steps for the multi-CPU/GPU implementation. The RK4 steps are:

$$\begin{aligned}\mathbf{k}_1 &= \Delta t f(t_n, \mathbf{u}_n) \\ \mathbf{k}_2 &= \Delta t f\left(t_n + \frac{1}{2} \Delta t, \mathbf{u}_n + \frac{1}{2} \mathbf{k}_1\right) \\ \mathbf{k}_3 &= \Delta t f\left(t_n + \frac{1}{2} \Delta t, \mathbf{u}_n + \frac{1}{2} \mathbf{k}_2\right) \\ \mathbf{k}_4 &= \Delta t f(t_n + \Delta t, \mathbf{u}_n + \mathbf{k}_3) \\ \mathbf{u}_{n+1} &= \mathbf{u}_n + \frac{1}{6}(\mathbf{k}_1 + 2\mathbf{k}_2 + 2\mathbf{k}_3 + \mathbf{k}_4),\end{aligned}$$

where each equation has a corresponding kernel launch. To handle a variety of Runge-Kutta implementations, steps \mathbf{k}_{1-4} correspond to calls to the same kernel with different arguments. The evaluation kernel returns two output vectors:

1. $\mathbf{k}_i = \Delta t f(t_n + \alpha_i \Delta t, \mathbf{u}_n + \alpha_i \mathbf{k}_{i-1})$, for steps $i = 1, 2, 3, 4$, and
2. $\mathbf{u}_n + \alpha_{i+1} \mathbf{k}_i$

We choose $\alpha_i = 0, \frac{1}{2}, \frac{1}{2}, 1, 0$ and $\mathbf{k}_0 = \mathbf{u}_n$. The second output for each $\mathbf{k}_{i=1,2,3}$ serves as input to the next evaluation, \mathbf{k}_{i+1} . In an effort to avoid an extra kernel launch—and corresponding

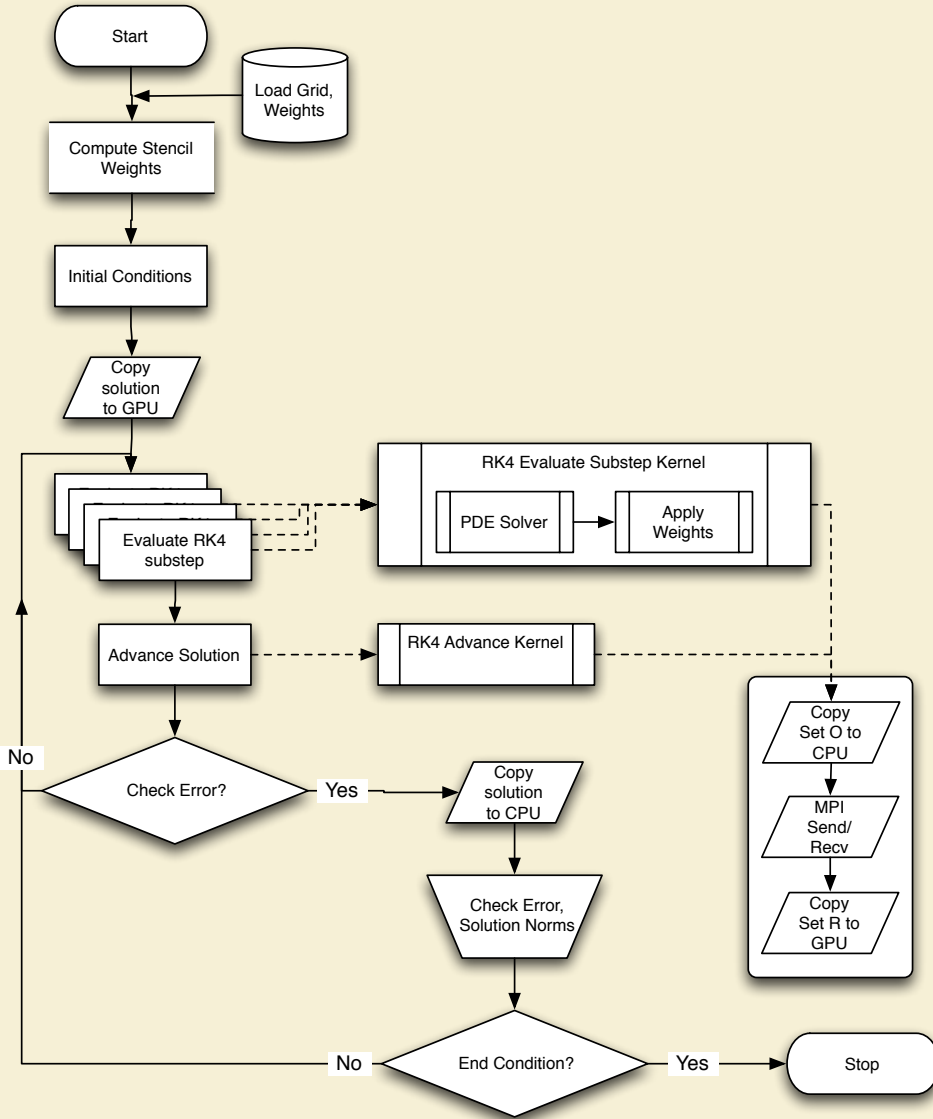


Figure 4.3: Workflow for RK4 on multiple GPUs.

memory loads—the SAXPY that produces the second output uses the same evaluation kernel. Both outputs are stored in global device memory. When the computation spans multiple GPUs, steps $\mathbf{k}_{1 \rightarrow 3}$ are each followed by a communication barrier to synchronize the subsets \mathcal{O} and \mathcal{R} of the second output (this includes copying the subsets between GPU and CPU). An additional synchronization occurs on the updated solution, \mathbf{u}_{n+1} , to ensure that all GPUs share a consistent view of the solution going into the next time-step.

To evaluate $\mathbf{k}_{1 \rightarrow 4}$, the discretized operators from Equation (2.9) are applied using sparse matrix-vector multiplication. If the operator D is composed of multiple derivatives, a differentiation matrix for each derivative is applied independently, including an additional multiplication for the discretized H operator. On the GPU, the kernel parallelizes across rows of the DMs, so all derivatives for stencils are computed in one kernel call.

For the GPU, the OpenCL language [50] assumes a lowest common denominator of hardware capabilities to provide functional portability. For example, all target architectures are assumed to support some level of SIMD (Single Instruction Multiple Data) execution for kernels. Multiple *work-items* execute a kernel in parallel. A collection of work-items performing the same task is called a *work-group*. While a user might think of work-groups as executing all work-items simultaneously, the work-items are divided at the hardware level into one or more SIMD *warps*, which are executed by a single multiprocessor. On the family of Fermi GPUs, a warp is 32 work-items [60]. OpenCL assumes a tiered memory hierarchy that provides fast but small *local memory* space that is shared within a work-group [50]. Local memory on Fermi GPUs is 48 KB per multiprocessor [60]. The *global device memory* allows sharing between work-groups and is the slowest but most abundant memory. In the GPU computing literature, the terms *thread* and *shared memory* are synonymous to *work-item* and *local memory* respectively, and are preferred below.

Although the primary focus of this paper is the implementation and verification of the RBF-FD method across multiple CPUs and GPUs, we have nonetheless tested two approaches to the computation of derivatives on the GPU to assess the potential for further improvements in performance. In both cases, the stencil weights are stored in CSR format [5], a packed one-dimensional array in global memory with all the weights of a single stencil in consecutive memory addresses. Each operator is stored as an independent CSR matrix. The consecutive ordering on the weights implies that the solution vector, structured according to the ordering of set \mathcal{G} is treated as random access.

All the computation on the GPU is performed in 8-byte double precision.

Naive Approach: One thread per stencil

In this first implementation, each thread computes the derivative at one stencil center (Figure 4.4). The advantage of this approach is trivial concurrency. Since each stencil has the same number of neighbors, each derivative has an identical number of computations. As long as the number of stencils is a multiple of the warp size, there are no idle threads. Should the total number of stencils be less than a multiple of the warp size, the final warp would contain idle threads, but the impact on efficiency would be minimal assuming the stencil size is sufficiently large.

Perfect concurrency from a logical point of view does not imply perfect efficiency in practice. Unfortunately, the naive approach is memory bound. When threads access weights in global memory, a full warp accesses a 128-byte segment in a single memory operation [60]. Since each thread handles a single stencil, the various threads in a warp access data in very disparate areas of global memory, rather than the same segment. This leads to very large slowdowns as extra memory operations are added for each 128-byte segment that the threads of a warp must access. However, with stencils sharing many common nodes, and the Fermi hardware providing caching, some weights in the unused portions of the segments might remain in cache long enough to hide the cost of so many additional memory loads.

Alternate Approach: One warp per stencil

An alternate approach, illustrated in Figure 4.5, dedicates a full warp of threads to a single stencil. Here, 32 threads load the weights of a stencil and the corresponding elements of

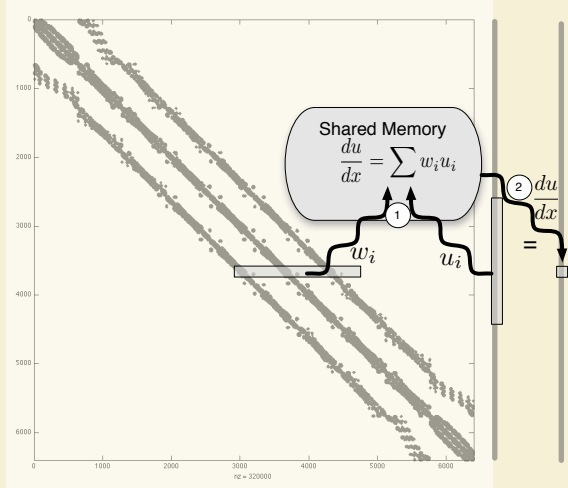


Figure 4.4: Naive approach to sparse matrix-vector multiply. Each thread is responsible for the sparse vector dot product of weights and solution values for derivatives at a single stencil.

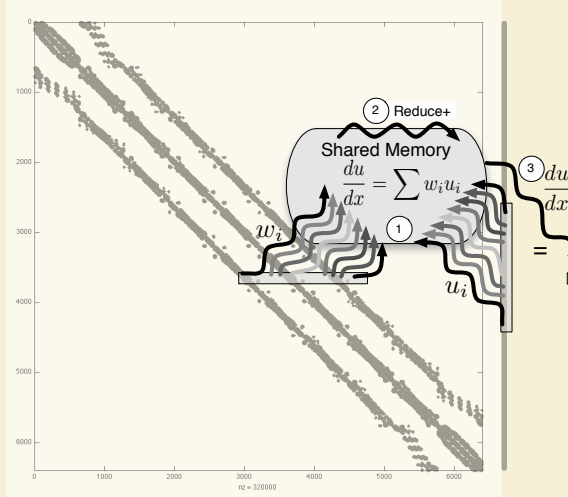


Figure 4.5: Alternative approach. A full warp (32 threads) collaborate to apply weights and compute the derivative at a stencil center.

the solution vector. As the 32 threads each perform a subset of the dot product, their intermediate sums are accumulated in 32 elements of shared memory (one per thread). Should a stencil be larger than the warp size, the warp iterates over the stencil in increments of the warp size until the full dot product is complete. Finally, the first thread of the warp performs a sum reduction across the 32 (warp size) intermediate sums stored in shared memory and writes the derivative value to global memory.

By operating on a warp by warp basis, weights for a single stencil are loaded with a reduced number of memory accesses. Memory loads for the solution vector remain random access but see some benefit when solution values for a stencil are in a small neighborhood in the memory space. Proximity in memory can be controlled by node indexing (see e.g.,

[?] and [12]).

For stencil sizes smaller than 32, some threads in the warp always remain idle. Idle threads do not slow down the computation within a warp, but under-utilization of the GPU is not desirable. For small stencil sizes, caching on the Fermi can hide some of the cost of memory loads for the naive approach, with no idle threads, making it more efficient. The real strength of one warp per stencil is seen for large stencil sizes. As part of future work on optimization, we will consider a parallel reduction in shared memory, as well as assigning multiple stencils to a single warp for small n .

dirichlet: kernel copies dirichlet values into place [Author's Note: Need to dust off code](#)

4.4.2 Fragments (integrate above)

While the nomenclature used in this paper is typically associated with CUDA programming, the names *thread* and *warp* are used to clearly illustrate kernel execution in context of the NVidia specific hardware used in tests. OpenCL assumes a lowest common denominator of hardware capabilities to provide functional portability. However, intimate knowledge of hardware allows for better understanding of performance and optimization on a target architecture. For example, OpenCL assumes all target architectures are capable at some level of SIMD (Single Instruction Multiple Data) execution, but CUDA architectures allow for Single Instruction Multiple Thread (SIMT). SIMT is similar to traditional SIMD, but while SIMD immediately serializes on divergent operations, SIMT allows for a limited amount of divergence without serialization.

At the hardware level, a *thread* executes instructions on the GPU. On Fermi level GPUs, groups of 32 threads are referred to as *warps*. A warp is the unit of threads executed concurrently on a single *multi-processor*. In OpenCL (i.e., software), a collection of hardware threads performing the same instructions are referred to as a *work-group* of *work-items*. Work-groups execute as a collection of warps constrained to the same multiprocessor. Multiple work-groups of matching dimension are grouped into an *NDRRange*. The *kernel* provides a master set of instructions for all threads in an NDRRange [50].

NVidia GPUs have a tiered memory hierarchy related to the grouping of threads described above. In multiprocessors, each computing core executes a thread with a limited set of registers. The number of registers varies with the generation of hardware, but always come in small quantities (e.g., 32K shared by all threads of a multiprocessor on the Fermi). Accessing registers is free, but keeping data in registers requires an effort to maintain balance between kernel complexity and the number of threads per block. Threads of a single work-group can share information within a multiprocessor through *shared memory*. With only 48 KB available per multiprocessor [60], shared memory is another fast but limited resource on the GPU. OpenCL refers to shared memory as *local memory*. Sharing information across multiprocessors is possible in *global device memory*—the largest and slowest memory space on the GPU. To improve seek times into global memory, Fermi level architectures include L1 on each multiprocessor and a shared L2 cache for all multiprocessors.

4.4.3 Implicit Solvers

Perhaps this section should move up. I think it might be best to discuss GMRES and iterative methods before Distributed Solvers (that way we can say the general solution form

is “matrix form”. but in parallel we need to use distributed algorithms.

The GMRES algorithm follows Algorithm ??.

The Arnoldi process can be completed using in a variety of ways. Some libraries like CUSP and [65] prefer the straightforward Givens rotations because they are easily parallelizable. The givens algorithm is provided in Algorithm ??

Others like [...] prefer to use an alternate algorithm. This algorithm is demonstrated in Algorithm ??.

Parallelizing the algorithm is possible with communication points listed in red (*).

4.5 RBF-FD as SpMV

From the definition of RBF-FD we can formulate the problem computationally in two ways. First, stencil operations are independent. Therefore, we can write kernels with perfect parallelism by dedicating a single thread per stencil or a group of threads per stencil.

Unfortunately, perfect concurrency does not imply perfect or even ideal concurrency on the GPU.

We first demonstrate the case where one thread is dedicated to each stencil. This is followed by dedicating a group of thread to the stencil. In each case we are operating under the assumption that each stencil is independent on the GPU.

To further optimize RBF-FD on the GPU, we formulate the problem in terms of a Sparse Matrix-Vector Mulitply (SpMV). When we consider the problem in this light we generate a single Differentiation Matrix that can see two optimizations not possible with our stencil-based view:

- First, the sparse containers used in SpMV allow for their own unique optimizations to compress storage and leverage hardware cache.
- Evaluation of multiple derivatives can be accumulated by association into one matrix operation. This reduces the total number of floating point operations required per iteration.

We compare the performance of our custom kernel to ViennaCL kernels (ELL, CSR, COO, HYB, DIAG), UBlas (COO, CSR) and Eigen (COO, CSR, ELL)

Chapter 5

Numerical Validation

5.1 Choosing ϵ

Present our attempts to get the right support parameter

We duplicate some results of [26] by choosing the same epsilon values specified in Table 5.1.

I also produced a Matlab script to generate the contours for any stencil size and produced the following figures.

5.1.1 CVT epsilon tests

[26] consider epsilon as a function of the number of nodes on the sphere. However, this assumption requires nodes to be distributed as MD nodes. When we apply the same functions to CVTs of larger problems we get varying results. The subtle perturbations in nodes

test on icosahedral grid

function based on min enclosing circle instead. Will be finer tuned to the grid. if nodes are uniform in stencil and stencil size locked then the only things that can influence epsilon and conditioning is the enclosing circle radius.

5.2 Parabolic

Include figure tracking max temperature and min temperature. If we have zero flux conditions then they should average out. If we have Dirichlet BCs the temperature will converge to 0.

5.3 Hyperbolic

Here, we present the first results in the literature for parallelizing RBF-FDs on multi-CPU and multi-GPU architectures for solving PDEs. To verify our multi-CPU, single GPU and multi-GPU implementations, two hyperbolic PDEs on the surface of the sphere are tested: 1) vortex roll-up [58, 59] and 2) solid body rotation [45]. These tests were chosen since they are not only standard in the numerical literature, but also for the development of

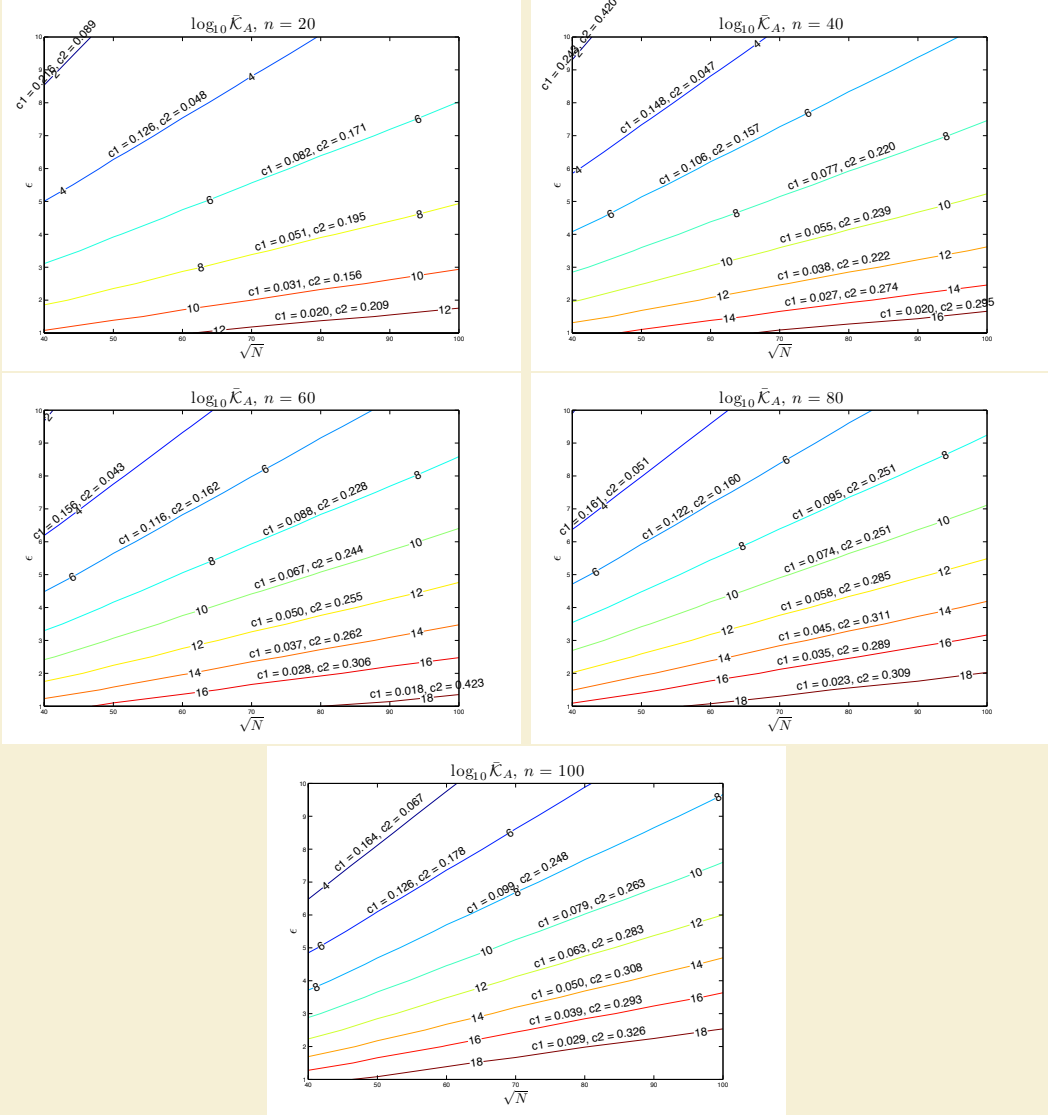


Figure 5.1: Contours for choosing ϵ for $n = 20, 40, 60, 80$ and 100 on the unit sphere as a function of \sqrt{N} . Contours assume near uniform distribution of nodes (e.g., maximum determinant nodes, icosahedral grids and spherical centroidal voronoi tessellations). Superimposed above each contour are parameters for the linear regression of the line, $c_1\sqrt{N} - c_2$.

RBFs in solving PDEs on the sphere [25, 27, 33, 36]. Although any ‘approximately evenly’ distributed nodes on the sphere would suffice for our purposes, maximum determinant (MD) node distributions on the sphere are used (see [72] for details) in order to be consistent with previously published results (see e.g., [27] and [34]). Node sets from 1024 to 27,556 are considered with stencil sizes ranging from 17 to 101.

All results in this section are produced by the single-GPU implementation. Multi-CPU and multi-GPU implementations are verified to produce these same results. Synchronization of the solution at each time-step and the use of double precision on both the CPU and GPU ensure consistent results regardless of the number and/or choice of CPU vs GPU.

Eigenvalues are computed on the CPU by the Armadillo library [66].

5.3.1 Vortex Rollup

The first test case demonstrates vortex roll-up of a fluid on the surface of a unit sphere. An angular velocity field causes the initial condition to spin into two diametrically opposed but stationary vortices.

The governing PDE in latitude-longitude coordinates, (θ, λ) , is

$$\frac{\partial h}{\partial t} + \frac{u}{\cos \theta} \frac{\partial h}{\partial \lambda} = 0 \quad (5.1)$$

where the velocity field, u , only depends on latitude and is given by

$$u = \omega(\theta) \cos \theta.$$

Note that the $\cos \theta$ in u and $1/\cos \theta$ in (5.1) cancel in the analytic formulation, so the discrete operator approximates $\omega(\theta) \frac{\partial}{\partial \lambda}$.

Here, $\omega(\theta)$ is the angular velocity component given by

$$\omega(\theta) = \begin{cases} \frac{3\sqrt{3}}{2\rho(\theta)} \operatorname{sech}^2(\rho(\theta)) \tanh(\rho(\theta)) & \rho(\theta) \neq 0 \\ 0 & \rho(\theta) = 0 \end{cases}$$

where $\rho(\theta) = \rho_0 \cos \theta$ is the radial distance of the vortex with $\rho_0 = 3$. The exact solution to (5.1) at non-dimensional time t is

$$h(\lambda, \theta, t) = 1 - \tanh\left(\frac{\rho(\theta)}{\gamma} \sin(\lambda - \omega(\theta)t)\right),$$

where γ defines the width of the frontal zone.

From a method of lines approach, the discretized version of (5.1) is

$$\frac{d\mathbf{h}}{dt} = -\operatorname{diag}(\omega(\theta)) D_\lambda \mathbf{h}. \quad (5.2)$$

where D_λ is the DM containing the RBF-FD weights that approximate $\frac{\partial}{\partial \lambda}$ at each node on the sphere.

For stability, hyperviscosity is added to the right hand side of (5.2) in the form given in (2.9). The scaling parameter γ_c and the order of hyperviscosity k are given in Table 5.1. The goal when choosing k is to damp the higher spurious eigenmodes of $\operatorname{diag}(\omega(\theta)) D_\lambda$ while leaving the lower physical modes that can be resolved by the stencil intact. In this process, the eigenvalues will be pushed into the left half of the complex plane. Then, γ_c is used to condense the eigenvalues as near to the imaginary axis as possible. Figure 5.2b shows the effect of hyperviscosity on the eigenvalues of the DM, $-\operatorname{diag}(\omega(\theta)) D_\lambda$, in (5.2).

In order to scale to large node sets, the RBF shape parameter, ϵ , is chosen such that the mean condition number of the local RBF interpolation matrices $\bar{\kappa}_A = \frac{1}{N} \sum_{j=1}^N (\kappa_A)_j$ is kept constant as N increases ($(\kappa_A)_j$ is the condition number of the interpolation matrix in (??), representing the j^{th} stencil). For a constant mean condition number, ϵ varies linearly with

Table 5.1: Values for hyperviscosity and the RBF shape parameter ϵ for vortex roll-up test.

	$\epsilon = c_1\sqrt{N} - c_2$		$H = -\gamma_c N^{-k} \Delta^k$	
Stencil Size (n)	c_1	c_2	k	γ_c
17	0.026	0.08	2	8
31	0.035	0.1	4	800
50	0.044	0.14	4	145
101	0.058	0.16	4	40

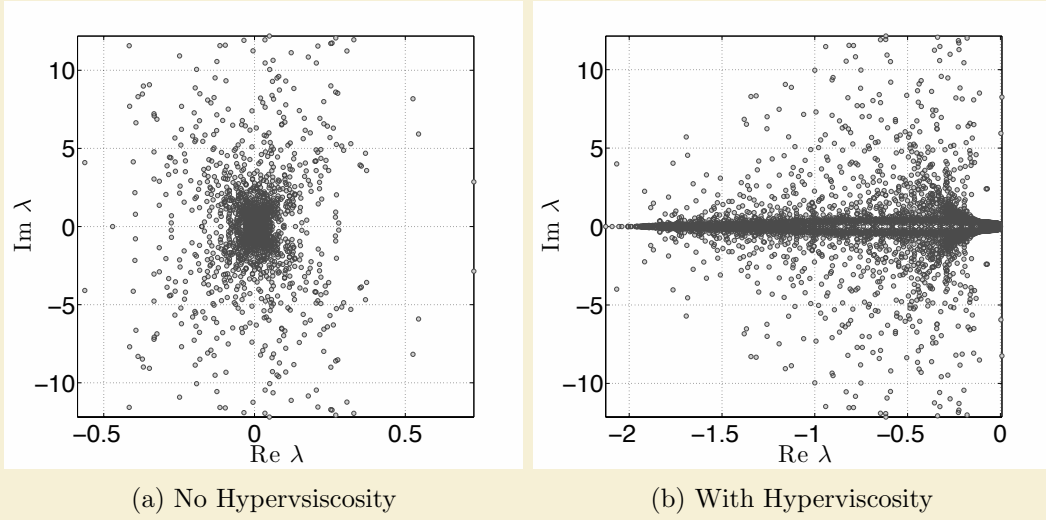


Figure 5.2: Eigenvalues of $\text{diag}(\omega(\theta))D_\lambda$ for the vortex roll-up test case for $N = 4096$ nodes, stencil size $n = 101$ and $\epsilon = 3.5$. Left: no hyperviscosity. Right: hyperviscosity enabled with $k = 4$ and $\gamma_c = 40$.

\sqrt{N} (see [26] Figure 4a and b). This is not surprising since the condition number strongly depends on the quantity ϵr , where $r \sim 1/\sqrt{N}$ on the sphere. Thus, to obtain a constant condition number, we let $\epsilon(N) = c_1\sqrt{N} - c_2$, where c_1 and c_2 are constants based on [26].

Figure 5.3 shows the solution to Equation (5.1) at $t = 10$, on $N = 10201$ nodes, with stencil size $n = 50$. This resolution is sufficient to properly capture the vortices at $t = 10$, but lower resolutions would suffer approximation errors associated with insufficient grid resolution. For this reason, the solution at $t = 3$ is considered in the normalized ℓ_2 error convergence study presented in Figure 5.4. The time step $\Delta t = 0.05$ for all resolutions.

Author's Note: Include older figures of convergence without stabilization. Mention that CVT nodes require independent tuning of HV param. Its useful but not incredibly convenient at the moment.

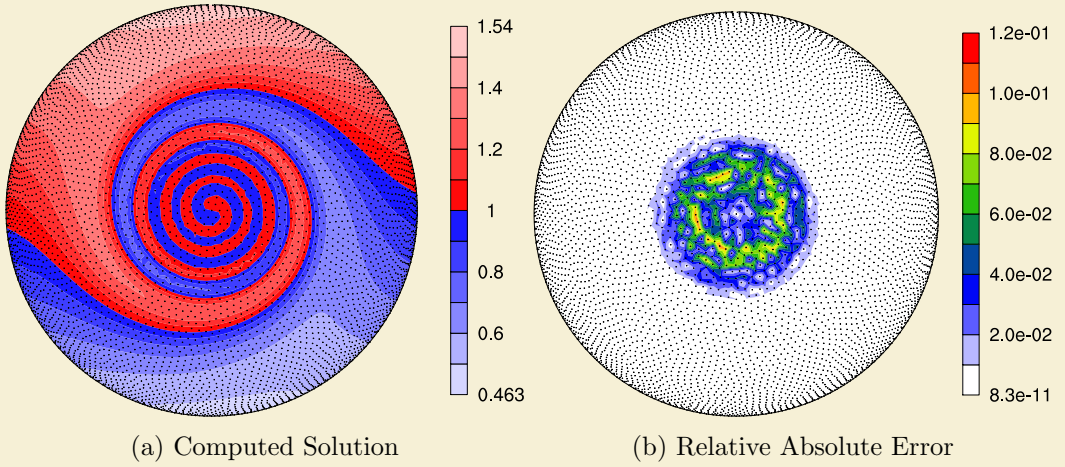


Figure 5.3: Vortex roll-up solution at time $t = 10$ using RBF-FD with $N = 10,201$ and $n = 50$ point stencil. Normalized ℓ_2 error of solution at $t = 10$ is $1.25(10^{-2})$

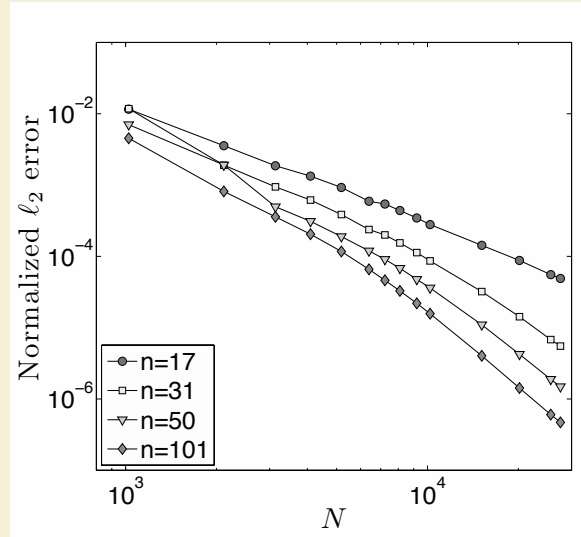


Figure 5.4: Convergence plot for vortex roll-up at $t = 3$.

5.3.2 Solid body rotation

The second test case simulates the advection of a cosine bell over the surface of a unit sphere at an angle α relative to the pole of a standard latitude-longitude grid. The governing PDE is

$$\frac{\partial h}{\partial t} + \frac{u}{\cos \theta} \frac{\partial h}{\partial \lambda} + v \frac{\partial h}{\partial \theta} = 0, \quad (5.3)$$

with velocity field,

$$\begin{cases} u = u_0(\cos \theta \cos \alpha + \sin \theta \cos \lambda \sin \alpha), \\ v = -u_0(\sin \lambda \sin \alpha) \end{cases}.$$

inclined at an angle α relative to the polar axis and velocity $u_0 = 2\pi/(1036800 \text{ seconds})$ to require 12 days per revolution of the bell as in [27, 59].

The discretized form of (5.3) is

$$\frac{d\mathbf{h}}{dt} = -\text{diag}\left(\frac{u}{\cos\theta}\right)D_\lambda\mathbf{h} - \text{diag}(v)D_\theta\mathbf{h} \quad (5.4)$$

where DMs D_λ and D_θ contain RBF-FD weights corresponding to all N stencils that approximate $\frac{\partial}{\partial\lambda}$ and $\frac{\partial}{\partial\theta}$ respectively. Rather than merge the differentiation matrices in (5.4) into one operator, our implementation evaluates them as two sparse matrix-vector multiplies. The separate matrix-vector multiplies are motivated by an effort to provide general and reusable GPU kernels. Additionally, they artificially increase the amount of computation compared to the vortex roll-up test case to simulate cases when operators cannot be merged into one DM (e.g., a non-linear PDE).

By splitting the DM, the singularities at the poles ($1/\cos\theta \rightarrow \infty$ as $\theta \rightarrow \pm\frac{\pi}{2}$) in (5.3) remain. However, in this case, the approach functions without amplification of errors because the MD node sets have nodes near, but not on, the poles. As noted in [27, 34], applying the entire spatial operator to the right hand side of Equation ?? generates a single DM that analytically removes the singularities at poles.

We will advect a C^1 cosine bell height-field given by

$$h = \begin{cases} \frac{h_0}{2}(1 + \cos(\frac{\pi\rho}{R})) & \rho \leq R \\ 0 & \rho \geq R \end{cases}$$

having a maximum height of $h_0 = 1$, a radius $R = \frac{1}{3}$ and centered at $(\lambda_c, \theta_c) = ({}^3\pi/2, 0)$, with $\rho = \arccos(\sin\theta_c \sin\theta + \cos\theta_c \cos\theta \cos(\lambda - \lambda_c))$. The angle of rotation, $\alpha = \pi/2$, is chosen to transport the bell over the poles of the coordinate system.

Table 5.2: Values for hyperviscosity and RBF shape parameter for the cosine bell test.

	$\epsilon = c_1\sqrt{N} - c_2$	$H = -\gamma_c N^{-k} \Delta^k$		
Stencil Size (n)	c_1	c_2	k	γ_c
17	0.026	0.08	2	$8 * 10^{-4}$
31	0.035	0.1	4	$5 * 10^{-2}$
50	0.044	0.14	6	$5 * 10^{-1}$
101	0.058	0.16	8	$5 * 10^{-2}$

Figure 5.5 compares eigenvalues of the DM for $N = 4096$ nodes and stencil size $n = 101$ before and after hyperviscosity is applied. To avoid scaling effects of velocity on the eigenvalues, they have been scaled by $1/u_0$. The same approach as in the vortex roll-up case is used to determine the parameters for hyperviscosity and ϵ . Our tuned parameters are presented in Table 5.2.

Figure 5.6 shows the cosine bell transported ten full revolutions around the sphere. Without hyperviscosity, RBF-FD cannot complete a single revolution of the bell before instability takes over. However, adding hyperviscosity allows computation to extend to dozens or even thousands of revolutions and maintain stability (e.g., see [34]). After ten

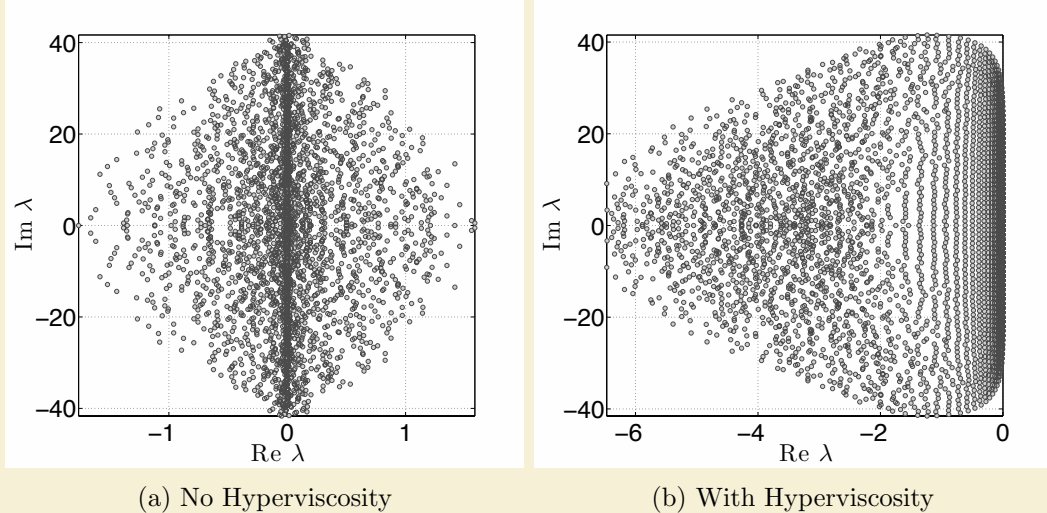


Figure 5.5: Eigenvalues of (5.4) for the cosine bell test case with $N = 4096$ nodes, stencil size $n = 101$, and $\epsilon = 3.5$. Left: no hyperviscosity. Right: hyperviscosity enabled with $k = 8$ and $\gamma_c = 5 * 10^{-2}$. Eigenvalues are divided by u_0 to remove scaling effects of velocity.

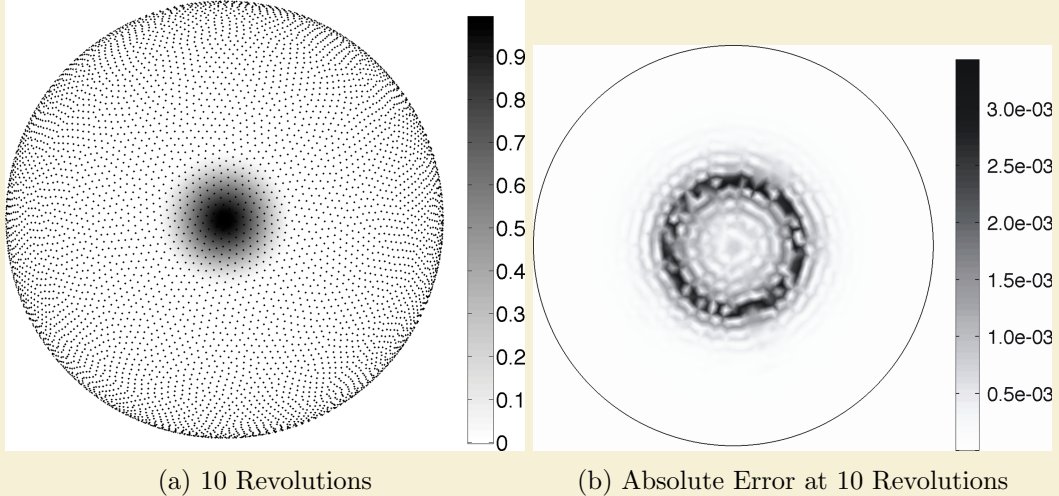


Figure 5.6: Cosine bell solution after 10 revolutions with $N = 10201$ nodes and stencil size $n = 101$. Hyperviscosity parameters are $k = 8$, $\gamma_c = 5(10^{-2})$.

revolutions, the cosine bell is still intact. The majority of the absolute error (Figure 5.6b) appears at the base of the C^1 bell where the discontinuity appears in the derivative. At ten revolutions, Figure 5.7 illustrates the convergence of the RBF-FD method. All tests in Figure 5.7 assume 1000 time-steps per revolution (i.e., $\Delta t = 1036.8$ seconds).

Complete: 17.28 minutes was a conservative step that allowed the problem to scale up to $N = 27556$ nodes. Compare this to the conservative 30 minute time-step taken for $N = 4096$ nodes in [27], which was already half necessary for DG and 8x less than necessary

for both Spherical Harmonics and Double Fourier methods. [Author's Note: It would be good to quantify the appropriate \$dt\$ that would compare RBF-FD to their \$N = 4096\$ case with global RBFs.](#)

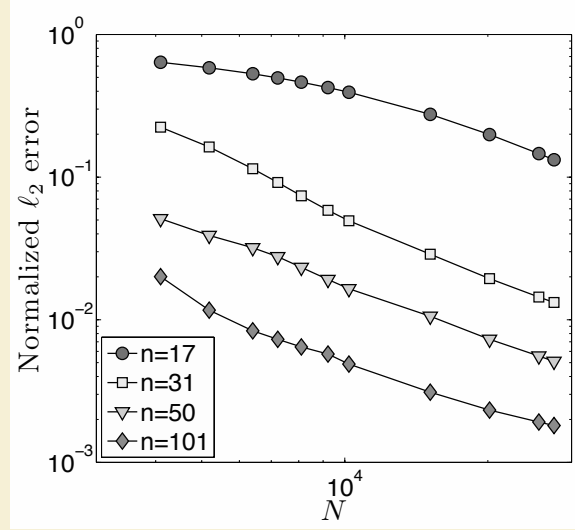


Figure 5.7: Convergence plot for cosine bell advection. Normalized ℓ_2 error at 10 revolutions with hyperviscosity enabled.

5.4 Fragments (integrate above)

To verify our multi-CPU and multi-CPU+GPU implementations, two hyperbolic PDEs on the surface of the sphere are tested. For both cases a spherical coordinate system is used in terms of latitude λ and longitude θ :

$$\begin{aligned} x &= \rho \cos \lambda \cos \theta, \\ y &= \rho \sin \lambda \cos \theta, \\ z &= \rho \sin \theta. \end{aligned}$$

Node sets are the Maximum Determinant point distributions on the sphere [72] consistent with previously published results (see e.g., [?] and [?]).

Hyperviscosity parameters γ_c and k depend on the RHS of the PDE. For this test case, hyperviscosity scaling parameters are listed in Table 5.1. Linear functions to choose the RBF support parameter ϵ are also provided. The parameters γ_c and k were obtained via trial-and-error parameter searching on $N = 4096$ nodes. The goal when choosing parameters is to push all eigenvalues to the left half-plane, and then tweak γ_c up or down to condense the eigenvalues as near to the imaginary axis as possible. We try to keep the range of filtered eigenvalue real parts within twice the width of the unfiltered range, so hyperviscosity does not cause too much diffusion in the solution.

For the cosine bell we use the initial conditions

$$h = \begin{cases} \frac{h_0}{2}(1 + \cos(\frac{\pi\rho}{R})) & \rho \leq R \\ 0 & \rho \geq R \end{cases}$$

where the bell of radius $R = \frac{a}{3}$ is centered at (λ_c, θ_c) and provided by the expression,

$$\rho = a \arccos(\sin \theta_c \sin \theta + \cos \theta_c \cos \theta \cos(\lambda - \lambda_c)).$$

We assume $a = 1$, $h_0 = 1$, and $(\lambda_c, \theta_c) = (\frac{3\pi}{2}, 0)$. The angle $\alpha = \frac{\pi}{2}$ is chosen to transport the bell over the poles of the coordinate system, and $u_0 = \frac{2\pi a}{1036800}$.

[Author's Note: State that we can split operator to test cases like nonlinear PDEs.](#)

[Author's Note: Include figures from NCL or Paraview](#)

5.4.1 CFL

We constrict our timesteps according to the Courant-Friedrich-Lowy (CFL) condition:

$$C_{\max} \frac{\Delta x_{\min}}{v_{\max}} < \Delta t$$

where Δx_{\min} is the minimum distance between any two nodes in the domain, and the v_{\max} is the maximum velocity

For the cosine bell test cases we use a conservative $C_{\max} = 0.4$ to ensure stable transport in all cases with $n = 101$. However, in testing it was found that $n = 17$ is capable of stably advecting with $C_{\max} > 1$ for $n = 17$; $n = 101$ can go up to $C_{\max} = 0.51$ for $N = 27556$ (e.g. 650 timesteps per revolution).

apparently, canceling the cosine analytically causes the conditioning of the system to change slightly. The hyperviscosity parameters I have in the paper are for the case with the cosine present. The parameters continue to function well for the other cases, but their impact on the eigenvalue distributions is noticeably higher (further span to the left).

5.5 GFLOP Throughput

In order to quantify the performance of our implementation, we can measure two factors. First, we can check the speedup achieved on the GPU relative to the CPU to get an idea of how much return of investment is to be expected by all the effort in porting the application to the GPU. Speedup is measured as the time to execute on the CPU divided by the time to execute on the GPU.

The second quantification is to check the throughput of the process. By quantifying the GFLOP throughput we have a measure that tells us two things: first, a concrete number quantifying the amount of work performed per second by either hardware, and second because we can calculate the peak throughput possible on each hardware, we also have a measure of how occupied our CPU/GPU units are. With the GFLOPs we can also determine the cost per watt for computation and conclude on what problem sizes the GPU is cost effective to target and use.

Now, as we parallelize across multiple GPUs, these same numbers can come into play. However we are also interested in the efficiency. Efficiency is the speedup divided by the number of processors. With efficiency we have a measure of how well-utilized processors are as we scale either the problem size (weak) or the number of processors (strong). As the efficiency diminishes we can conclude on how many stencils/nodes per processor will keep our processors occupied balanced with the shortest compute time possible (i.e., we are maximizing return of investment).

5.6 Elliptic

Chapter 6

Stokes

6.1 Introduction

We consider herein the solution to steady-state viscous Stokes flow on the surface of a sphere, governed by: [Author's Note: Where did we go wrong? Our vector laplacian does not have a curl component included. How do we derive that from here?](#)

$$\nabla \cdot [\eta(\nabla \mathbf{u} + (\nabla \mathbf{u})^T)] + RaT\hat{r} = \nabla p \quad (6.1)$$

$$\nabla \cdot \mathbf{u} = 0 \quad (6.2)$$

where the unknowns \mathbf{u} and p represent the vector velocity- and scalar pressure-field respectively, η is the viscosity tensor, Ra is the non-dimensional Rayleigh number, and T is an initial temperature profile. Many practical applications in sciences such as geophysics, climate modeling, and computational fluid dynamics must solve variations of the Navier-Stokes equations. The focus of this paper is on the implicit solve component for viscous (Stokes) flow, which amounts to the steady-state problem described by Equations 6.1 and 6.2.

This article introduces the first (to our knowledge) parallel approach to solve the steady-state equations on the surface of the unit sphere with the Radial Basis Function-generated Finite Differences (RBF-FD) method. Building on our work in [?], which parallelized explicit RBF-FD advection, our goal is to integrate both explicit and implicit components within a larger transient flow model.

[Author's Note: follow with details of RBF methods and novelty of RBF-FD.](#)

For decades, the demand for fast and accurate numerical solutions in fluid flow has lead to a plethora of computational methods for various geometries, discretizations and dimensions. On the sphere in \mathbb{R}^3 popular discretizations include the standard latitude-longitude grid, cubed-sphere [59], yin-yang overlapping grid [46], icosahedral grid [62] and centroidal voronoi tessellations [17]. Associate with each discretization is a mesh—specific to the choice of numerical method—that indicates connectivity of nodes for differentiation.

Two decades ago [47], meshless methods based on Radial Basis Functions (RBFs) were introduced for problems that require geometric flexibility with scattered node layouts in d -dimensional space, plus natural extensions to higher dimensions with minimal change in programming complexity [27, 85]. These RBF methods tout competitive accuracy with

other state-of-the-art and high-order methods [24, 25, 27, 28, 85], as well as stability for large time steps. A survey of RBF methods is provided by [24].

Author's Note: Change first sentence RBF-generated finite differences (RBF-FD) hold a promising future in that they share many advantages of global RBF methods, but reduce computational complexity to $O(N)$ and exhibit increased parallelism. The method was first suggested in 2000 [77], but made its grand debut a few years later in the simultaneous, yet independent, efforts of [9, 70, 76, 84]. It has been successfully employed for a variety of problems including Hamilton-Jacobi equations [9], convection-diffusion problems [10, 73], incompressible Navier-Stokes equations [11, 70], transport on the sphere [34], and the shallow water equations [26].

Compared to classical finite differences (FD) which calculate differentiation weights with one-dimensional polynomials, RBF-FD leverages d -dimensional RBFs as test functions. This allows for generalization to d -dimensional space on completely scattered node layouts. For both methods, a stencil of size n neighboring nodes determines the accuracy of the approximation. However, contrary to the regular stencil node distributions from FD, RBF-FD allows for completely scattered node distributions. In comparison with global RBF methods, spectral accuracy is sacrificed in exchange for computational speed and parallelism. Still, high-order accuracy is possible with RBF-FD—6th- to 10th-order accuracy is common.

Until now, most of the focus in RBF-FD has been on explicit methods. However, many practical applications in sciences such as geophysics, climate modeling, and computational fluid dynamics must solve variations of the navier stokes equations which include an implicit solve component. This paper develops multi-GPU algorithms for implicit RBF-FD systems toward the goal of integration within transient flow problems. The explicit component of transient flow is a natural extension of our work in [?].

Author's Note: Flesh these points out and integrate them in surrounding paragraphs (until "end") Speed not the issue. Need less RBFs for given accuracy of steady state less nodes implies less memory general geometries are supported better distributions of nodes on spheres. competition like CitComS, etc. use cubed sphere, yinyang grids and triangular meshes in combination with low order methods (2nd and 3rd order). Increasing the order of the method or dimension can significantly increase the complexity of the algorithms. RBF-FD naturally extends to higher dimensions and increasing the order is as simple as increasing the number of nodes in the stencil. **Author's Note:** end

Related work ([list references](#)): RBF methods for Elliptic PDEs

- Global [69]
- Compact Support
- divergence-free spherical radial basis Glerkin method for Stokes on the unit sphere [?]
- RBF-FD
 - Incompressible Navier-Stokes using explicit (Euler) and semi-implicit (Crank Nicholson) time step. Small problem size (61×61) and small stencil sizes ($n = 9$);

ghost nodes beyond boundary strategy. Both RBF-FD and RBF-HFD tested.
[11]

Related work on Preconditioned iterative methods for Stokes Flow

- Survey of preconditioners used for Stokes flow problems [55] (limited applicability since they do not assume non-SPD matrices)
- Multi-GPU Jacobi iteration for Navier stokes flow in cavity http://scholarworks.boisestate.edu/cgi/viewcontent.cgi?article=1003&context=mecheng_facpubs

For decades, a major push has been executed in science to parallelize algorithms and leverage resources available on the increasingly capable supercomputers and clusters. Perhaps as soon as the next decade, we will see exascale level architectures ([?]). Given today's technology, those architecture will surely achieve their performance with the help of accelerator hardware such as GPUs.

To prepare the RBF community for the future, we develop algorithms employing two levels of parallelization: first the MPI standard spans computation across multiple CPUs, and second computation is distributed across the many processing cores of GPU accelerators.

The two level parallelization can even be extended to three level parallelism with pThreads or OpenMP [?]. While OpenCL provides the means to target parallelism on either multi-core CPUs or many-core GPUs, it does not allow a parallel kernel on one hardware interact with a parallel kernel on the another. That is to say, an OpenCL kernel on the CPU cannot launch kernels on the GPU.

Our goal is to demonstrate to the geosciences that RBF-FD can function well on both hyperbolic and elliptic problems. In [?] we introduced a multi-GPU implementation of RBF-FD and demonstrated the method's strong ability to stably advect solid bodies on the sphere. In this paper we continue toward the goal of RBF-FD solutions for fluid flow problems with a multi-GPU Poisson solver for steady-state Stokes flow. In this context, speed is not a paramount issue.

Related work on RBF methods targeting the GPU is quite limited. Schmidt et al. [69] solve an implicit system for a global RBF method using Accelerys Jacket in Matlab. Our work in [?] introduced the first parallel implementation of RBF-FD for explicit advection capable of spanning multiple CPUs as well as multiple GPUs.

Related work on multi-CPU or multi-GPU RBFs

- CPU [89] [?]
- single-GPU [69]
- multi-GPU
 - Preconditioned BiCGStab for Navier Stokes, Finite Element method [38]

While RBF-FD differentiation matrices are applied in the same fashion as standard FD methods, they are unique in that they are asymmetric, non-positive definite and potentially have high condition numbers. To solve an implicit system therefore, we require an iterative krylov solver like GMRES or BiCGStab which are applicable to matrices of this type.

Additionally, preconditioned variants of these methods are required to reduce the complexity of the solution process.

Within this paper we implement a preconditioned GMRES method for RBF-FD on multiple GPUs.

Parallel GMRES

- CPU only: PETSc [89], Hypre [?]
- Parallel GMRES on single GPU available in ViennaCL [63] and CUSP [?]
- Parallel GMRES on Multiple GPUs [2]
- Reduced Communication with increased computation [15]

This article continues our effort with an implementation of RBF-FD on both single and multiple-GPUs for elliptic PDEs. In the next section we introduce

6.2 Bad Problem

Our initial derivation of the Stokes problem was incorrect. What we thought was the proper identity reduced the problem to simple scalar velocity laplacians and pressure gradients. The correct formulation of Stokes flow in 3D would have a curl component connecting each dimension.

Rather than start over and reformulate our problem, we opted to continue development of our GPU-based solver with the recognition that the problem we posed is actually a coupled Poisson problem and can be solved using the same iterative solver. By implementing and testing the solver and preconditioners for one problem, we prepare for the other.

6.2.1 Details

Items to test for our solver: GFLOPs throughput (CPU,GPU), Convergence of Solver (in iteration residual) vs Preconditioners.

Test problems: Sphere coupled poisson. Annulus. Stokes on annulus?

6.3 RBF-FD Weights

Given a set of function values, $\{u(\mathbf{x}_j)\}_{j=1}^N$, on a discrete set of nodes $\{\mathbf{x}_j\}_{j=1}^N$, the operator \mathcal{L} acting on $u(\mathbf{x}_j)$ is approximated by a weighted combination of function values, $\{u(\mathbf{x}_i)\}_{i=1}^n$, in a small neighborhood of $u(\mathbf{x}_j)$, where n defines the size of the stencil and $n \ll N$:

$$\mathcal{L}u(\mathbf{x})|_{\mathbf{x}=\mathbf{x}_j} \approx \sum_{i=1}^n w_i u(\mathbf{x}_i) \quad (6.3)$$

The RBF-FD weights, w_i , are found by enforcing that they are exact within the space spanned by the RBFs $\phi_i(\epsilon r) = \phi(\epsilon \|\mathbf{x} - \mathbf{x}_i\|)$, centered at the nodes $\{\mathbf{x}_i\}_{i=1}^n$, with $r = \|\mathbf{x} - \mathbf{x}_i\|$ being the distance between the RBF center and the evaluation point measured in the standard Euclidean 2-norm. It has also been shown through experience and studies

[26, 29, 34, 86] that better accuracy is gained by the interpolant being able to reproduce a constant. Hence, the constraint $\sum_{i=1}^n c_k = \mathcal{L}1|_{\mathbf{x}=\mathbf{x}_j} = 0$ is added, where w_{n+1} is ignored after the matrix in (6.4) is inverted. That is,

$$\begin{pmatrix} \phi(\epsilon \|\mathbf{x}_1 - \mathbf{x}_1\|) & \phi(\epsilon \|\mathbf{x}_1 - \mathbf{x}_2\|) & \cdots & \phi(\epsilon \|\mathbf{x}_1 - \mathbf{x}_n\|) & 1 \\ \phi(\epsilon \|\mathbf{x}_2 - \mathbf{x}_1\|) & \phi(\epsilon \|\mathbf{x}_2 - \mathbf{x}_2\|) & \cdots & \phi(\epsilon \|\mathbf{x}_2 - \mathbf{x}_n\|) & 1 \\ \vdots & \ddots & \ddots & \vdots & \vdots \\ \phi(\epsilon \|\mathbf{x}_n - \mathbf{x}_1\|) & \phi(\epsilon \|\mathbf{x}_n - \mathbf{x}_2\|) & \cdots & \phi(\epsilon \|\mathbf{x}_n - \mathbf{x}_n\|) & 1 \\ 1 & 1 & \cdots & 1 & 0 \end{pmatrix} \begin{bmatrix} c_1 \\ c_2 \\ \vdots \\ c_n \\ c_{n+1} \end{bmatrix} = \begin{bmatrix} \mathcal{L}\phi(\epsilon \|\mathbf{x} - \mathbf{x}_1\|)|_{\mathbf{x}=\mathbf{x}_j} \\ \mathcal{L}\phi(\epsilon \|\mathbf{x} - \mathbf{x}_2\|)|_{\mathbf{x}=\mathbf{x}_j} \\ \vdots \\ \mathcal{L}\phi(\epsilon \|\mathbf{x} - \mathbf{x}_n\|)|_{\mathbf{x}=\mathbf{x}_j} \\ 0 \end{bmatrix} \quad (6.4)$$

This small system solve is repeated N times for each \mathbf{x}_j , $j = 1\dots N$, to form the DM associated with one derivative quantity. As an example, if \mathcal{L} is the identity operator then the above procedure will lead to RBF-FD interpolation. If \mathcal{L} is $\frac{\partial}{\partial x}$, it will lead to the DM that approximates the first derivative in x . While Equation 6.4 is symmetric, the added constraints for coefficient c_{n+1} detracts from the system's positive definite-ness. In lieu of this, a direct LU factorization solves for the weights. Also, observe that multiple right hand sides can be employed to efficiently obtain weights corresponding to all required derivative quantities (i.e., $\frac{\partial}{\partial x}$, $\frac{\partial}{\partial y}$, ∇^2 , etc.) in one system solve per stencil center.

6.4 GPU Based Solver

Author's Note: We should only discuss the ViennaCL implementation. Unless I can get my ILU preconditioner implemented for CUSP.

Our implementation leverages existing libraries for sparse matrix-vector operations on the GPU. Two libraries exist for sparse matrix linear algebra on the GPU: CUSP [5] and ViennaCL [63]. By implementing our algorithm in the context of ViennaCL, we directly benefit from improvements to the performance of underlying sparse matrix-vector product, vector dot vector and other linear algebra primitives. Also, ViennaCL provides seamless interoperability with the Boost::UBLAS, EIGEN and MTL libraries via C++ templates. We test the performance of our algorithm on one or more CPUs with the Boost::UBLAS library.

Table comparing CUSP and ViennaCL features

The GMRES algorithm was introduced in 1986 by Saad and Schultz [64]. The iterative solver support general matrix structures, whereas methods like Conjugate Gradient require symmetric positive definiteness.

6.4.1 GMRES Algorithm

At the core of the GMRES algorithm is an Arnoldi (orthogonalization) process. **Author's Note:** significance of orthogonalization.

Multiple variants of GMRES exist **Author's Note:** cite refs that utilize unique orthogonalization steps. The motivation behind alternative Arnoldi processes is to save both memory and operation counts. In some cases stability of the GMRES iterations can also be improved **Author's Note:** I recall a paper saved on my laptop. Saad [64] introduced a

practical implementation of the GMRES method that utilizes Given's rotations to compute an implicit QR factorization. The Given's based algorithm is part of the CUSP library; ViennaCL implements the Householder reflection algorithm.

We have implemented the Given's rotation algorithm within ViennaCL, because it is simpler to implement in parallel and increases parallelism [Author's Note: verify statement with reference](#).

[2] does not describe their use of rotations.)

Note that the application of a preconditioner such as ILU0 introduces an additional call to MPI_Alltoallv before everywhere M^{-1} is present in Algorithm 6.2.

Algorithm 6.1 Left-preconditioned GMRES(k) with Given's Rotations

```

1:  $\varepsilon$  (tolerance for the residual norm  $r$ ),  $x_0$  (initial guess), and set  $convergence = false$ 
2: MPI_Alltoallv( $x_0$ )
3: while  $convergence == false$  do
4:    $r_0 = M^{-1}(b - Ax_0)$ 
5:   MPI_Alltoallv( $r_0$ )
6:    $\beta = \|r_0\|_2$                                      ▷ MPI_Allreduce( $r_0, r_0$ )
7:    $v_1 = r_0/\beta$ 
8:   for  $j = 1$  to  $k$  do
9:      $w_j = M^{-1}Av_j$                                 ▷ MPI_Alltoallv( $w_j$ )
10:    for  $i = 1$  to  $j$  do
11:       $h_{i,j} = \langle w_j, v_i \rangle$                   ▷ MPI_Allreduce
12:       $w_j = w_j - h_{i,j}v_i$ 
13:    end for
14:     $h_{j+1,j} = \|w_j\|_2$                             ▷ MPI_Allreduce
15:     $v_{j+1} = w_j/h_{j+1,j}$ 
16:  end for
17:  Set  $V_k = [v_1, \dots, v_k]$  and  $\bar{H}_k = (h_{i,j})$  an upper Hessenberg matrix of order  $(m + 1) \times m$ 
18:  Solve a least-square problem of size  $m$ :  $\min_{y \in \mathbb{R}^k} \|\beta e_1 - \bar{H}_k y\|_2$ 
19:   $x_k = x_0 + V_k y_k$ 
20:  if  $\|M^{-1}(b - Ax_k)\|_2 < \varepsilon$  then
21:     $convergence = true$ 
22:  end if
23: end while

```

6.4.2 Multiple GPUs

Domain Decomposition

A restricted additive Schwarz [?] domain decomposition is applied. Traditional additive Schwarz methods construct a restriction matrix R to constrain processor computation to a subdomain and R^T project it back onto the global domain. In contrast, restricted additive Schwarz replaces the restriction matrix R with some restriction operator R_P^0 where $R_P^0 \subset R$, but continues to use R^T to project the solution back onto the global domain. The main idea behind re , restricted additive schwarz assigns all nodes to exactly one subdomain.

Regular additive Schwarz would allow nodes to be in one or more subdomains.

$$\mathbf{u} = \sum_{p=0}^{\text{numprocs}} R'_p (A(R_p^0)^T)^{-1} R_P^0 R_P F \quad (6.5)$$

where R_p is a restriction matrix (identity on diagonals for stencils operated on by a processor, zero elsewhere). In our case, the partitions are determined by node coordinates, so all non-zeros for a stencil row end up on the same processor (i.e., the decomposition of the matrix does not allow multiple domain blocks per row).

MPI Communication

Mention communication using MPI_AlltoAllv, MPI_Allreduce. (Show communication points in algorithm—be sure to explicitly show Givens rotations in algorithm. [2] did list rotations. We also use the CPU for Gram Schmidt process.)

6.5 Multiple GPUs

Scaling GMRES across multiple GPUs requires a domain decomposition. Domain decompositions can be interpreted as partitioning of nodes or cuts along

Domain Decomposition

The domain is decomposed naively by cutting the domain into domain bounding box into P equal sized partitions. Each processor is assigned one partition. Partitions may contain unequal number of nodes. Future work will integrate a domain partitioning library such as ParMETIS [?] or SCOTCH [?] to improve load balancing for processors.

$$\mathbf{u} = \sum_{p=0}^{\text{numprocs}} R_p (A R_p^T)^{-1} F \quad (6.6)$$

where R_p is a restriction matrix (identity on diagonals for stencils operated on by a processor, zero elsewhere). In our case, the partitions are determined by node coordinates, so all non-zeros for a stencil row end up on the same processor (i.e., the decomposition of the matrix does not allow multiple domain blocks per row).

The restriction matrix R_p^0 contains only zeros and ones. Cai et al. [?] let R_p^0 contain ones on the diagonal to indicate rows of the system for which a processor p is responsible. Our implementation similarly places I on the diagonal, but we then apply a general permutation matrix P to compress $R_p^0 A$ such that processors assemble an $N_p \times m$ local matrix (where $N_p \ll N$ and $m \ll N$). Likewise, processors allocate vectors for the reduced problem size. The solution is $N_p \times 1$ and RHS is $m \times 1$. Recall that the domain decomposition is determined by node partitioning, which does not guarantee rows of the global system corresponding to stencils in a processor's partition will be a contiguous block of the full system.

6.5.1 Solution Ordering

To simplify distribution of solution values, we apply a reordering to the system to interleave components of the solution and group solutions by node. This allows us to directly copy a double4 for each

The DM assembly depends on all dimensions of solution values for a single node to be consecutive in memory. While Equation 6.15 has all components of U, V, W and P grouped together, the values of u_1, v_1, w_1 and p_1 correspond to node (x_1, y_1, z_1) .

Figure 6.1 demonstrates the effect of interleaving our solution. The sparsity pattern of the original DM with solutions grouped by component is shown in Figure 6.1a. Well defined blocks of non-zeros are filled with RBF-FD weights from Equation 6.7. Figure 6.1b presents the sparsity pattern for interleaved solution components. The pattern is similar to a single block of Figure 6.1a, but the sub-matrix $(10 : 50) \times (10 : 50)$ of each solution ordering, shown in Figures 6.1c and 6.1d, illustrate that non-zeros in Figure 6.1b are small 4×4 blocks with the structure of Equation 6.7.

Node Order

Author's Note: Should we discuss node ordering and its implications on convergence? if so, I should state:

- Nodes are read from file
- Their order is either: unmodified or modified
- If modified, our goal is to improve memory access patterns by reducing the bandwidth of the DM. A bandwidth of n is the best case scenario where the solution vector is accessed linearly. The worst case scenario is when bandwidth is N and the solution is accessed randomly via stencils.
- Ordering nodes according to a space filling curve can reduce the “randomness” of solution access by placing elements of stencils nearby (sometimes sequential) in memory.
- Many space filling curves exist. Raster (IJK), Snake, Morton, Hilbert, U, X, etc. We consider Raster here, with other orderings left for future work.
- Our restriction operator for domain decomposition might reduce the bandwidth for each processor compared to the global DM. How does the combination of restriction and reordering work?
- Reordering the DM has implications on its condition number and the convergence rate of the GMRES algorithm. We should provide bandwidth of matrix before and after reordering, as well as the condition number before and after. We should monitor convergence with and without reordering, and compare the number of GMRES iterations per minute/second.

MPI Communication

The majority of communication within our implementation consists of two MPI routines: MPI_Alltoallv and MPI_Allreduce.

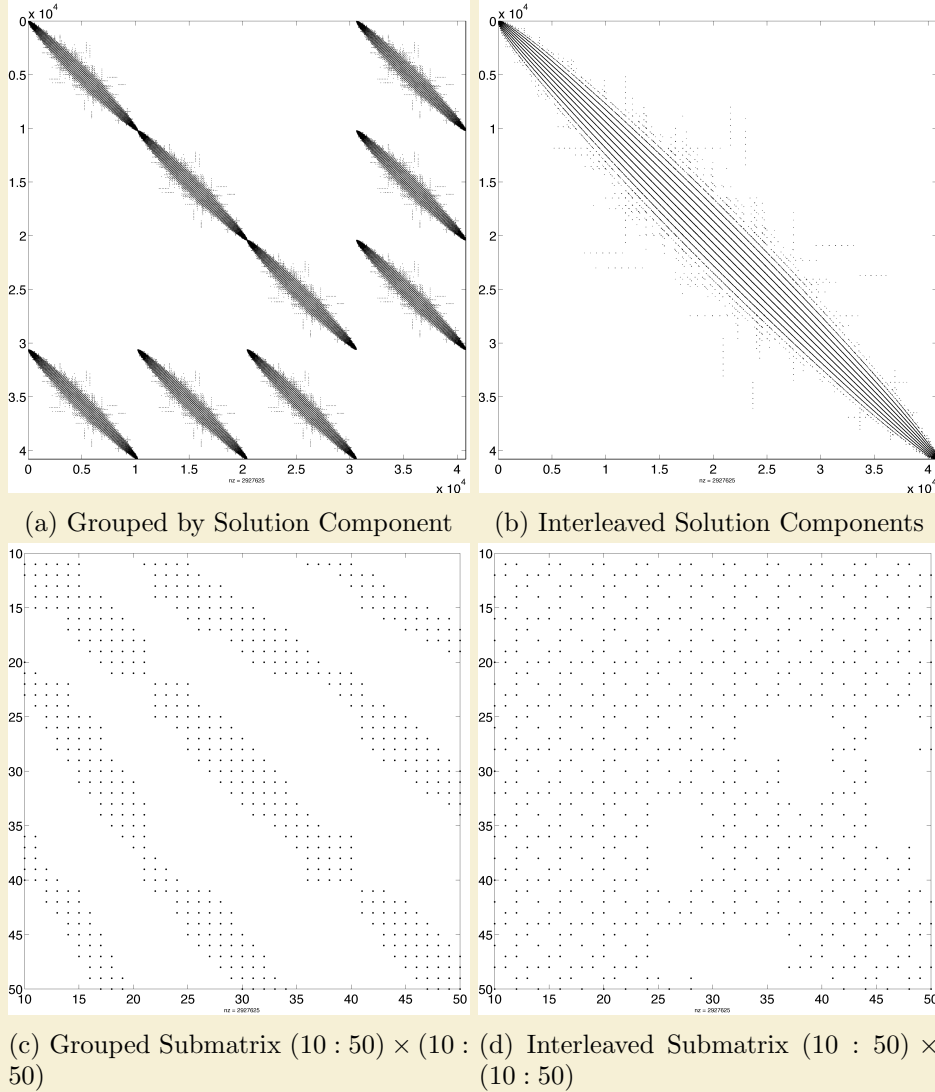


Figure 6.1: Sparsity pattern of linear system in Equation 6.7. Solution values are either ordered by component (e.g., $(u_1, \dots, u_N, v_1, \dots, v_N, w_1, \dots, w_N, p_1, \dots, p_N)^T$) or interleaved (e.g., $(u_1, v_1, w_1, p_1, \dots, u_N, v_N, w_N, p_N)^T$).

6.6 Governing Equations

We solve the PDE on the surface of the sphere as an example for one and multiple GPUs. Boundary conditions detract from the accuracy of RBF-FD and introduce other issues such as Runge phenomena [?], so we first verify the solution without boundaries.

Author's Note: Need to reference work that solves problem in two steps and justify our approach to solve in one step. Golub paper might be good for this. Or the Stoke preconditioners paper

Assuming η is a constant (i.e., $\nabla\eta = 0$), our system simplifies to

$$\begin{pmatrix} -\eta\nabla^2 & 0 & 0 & \frac{\partial}{\partial x_1} \\ 0 & -\eta\nabla^2 & 0 & \frac{\partial}{\partial x_2} \\ 0 & 0 & -\eta\nabla^2 & \frac{\partial}{\partial x_3} \\ \frac{\partial}{\partial x_1} & \frac{\partial}{\partial x_2} & \frac{\partial}{\partial x_3} & 0 \end{pmatrix} \begin{pmatrix} u_1 \\ u_2 \\ u_3 \\ p \end{pmatrix} = \frac{RaT}{\sqrt{x_1^2 + x_2^2 + x_3^2}} \begin{pmatrix} x_1 \\ x_2 \\ x_3 \\ 0 \end{pmatrix}. \quad (6.7)$$

where the ∇^2 operator in spherical polar coordinates for \mathbb{R}^3 is:

$$\nabla^2 = \underbrace{\frac{1}{\hat{r}} \frac{\partial}{\partial \hat{r}} \left(\hat{r}^2 \frac{\partial}{\partial \hat{r}} \right)}_{\text{radial}} + \underbrace{\frac{1}{\hat{r}^2} \Delta_S}_{\text{angular}}. \quad (6.8)$$

Here Δ_S is the Laplace-Beltrami operator—i.e., the Laplacian constrained to the surface of the sphere with radius \hat{r} . This form nicely illustrates the components of the ∇^2 corresponding to the radial and angular terms.

On the surface of the unit sphere the radial term vanishes, so we are left with:

$$\nabla^2 \equiv \Delta_S. \quad (6.9)$$

The following RBF operator from [85]—Equation (20) can be applied to the RHS of Equation 6.4 to generate Laplace-Beltrami RBF-FD weights:

$$\Delta_S = \frac{1}{4} \left[(4 - r^2) \frac{\partial^2}{\partial r^2} + \frac{4 - 3r^2}{r} \frac{\partial}{\partial r} \right], \quad (6.10)$$

where r is the Euclidean distance between nodes of an RBF-FD stencil and is independent of our choice of coordinate system.

Additionally following [26, 28], the off-diagonal blocks in Equation 6.7 must be constrained to the sphere via the projection matrix:

$$P = I - \mathbf{x}\mathbf{x}^T = \begin{pmatrix} (1 - x_1^2) & -x_1x_2 & -x_1x_3 \\ -x_1x_2 & (1 - x_2^2) & -x_2x_3 \\ -x_1x_3 & -x_2x_3 & (1 - x_3^2) \end{pmatrix} = \begin{pmatrix} P_{x_1} \\ P_{x_2} \\ P_{x_3} \end{pmatrix} \quad (6.11)$$

where \mathbf{x} is the unit normal at the stencil center, and [26, 28] show that with a little manipulation weights can be directly computed with these operators for Equation 6.4:

$$P \frac{\partial}{\partial x_1} = (x_1 \mathbf{x}^T \mathbf{x}_k - x_{1,k}) \frac{1}{r} \frac{\partial}{\partial r} |_{\mathbf{x}=\mathbf{x}_j} \quad (6.12)$$

$$P \frac{\partial}{\partial x_2} = (x_2 \mathbf{x}^T \mathbf{x}_k - x_{2,k}) \frac{1}{r} \frac{\partial}{\partial r} |_{\mathbf{x}=\mathbf{x}_j} \quad (6.13)$$

$$P \frac{\partial}{\partial x_3} = (x_3 \mathbf{x}^T \mathbf{x}_k - x_{3,k}) \frac{1}{r} \frac{\partial}{\partial r} |_{\mathbf{x}=\mathbf{x}_j} \quad (6.14)$$

6.6.1 Constraints

Due to the lack of boundary conditions on the sphere, the family of solutions that satisfy the PDE in Equation 6.7 includes four free constants (one for each u_1, u_2, u_3 and p).

One way to close the null-space of the solution is to augment Equation 6.7 with the following constraints:

$$\left(\begin{array}{cccc|cccc} -\eta \nabla^2 & 0 & 0 & \frac{\partial}{\partial x_1} & 1_{N \times 1} & 0 & 0 & 0 \\ 0 & -\eta \nabla^2 & 0 & \frac{\partial}{\partial x_2} & 0 & 1_{N \times 1} & 0 & 0 \\ 0 & 0 & -\eta \nabla^2 & \frac{\partial}{\partial x_3} & 0 & 0 & 1_{N \times 1} & 0 \\ \frac{\partial}{\partial x_1} & \frac{\partial}{\partial x_2} & \frac{\partial}{\partial x_3} & 0 & 0 & 0 & 0 & 1_{N \times 1} \\ \hline 1_{1 \times N} & 0 & 0 & 0 & & & & \\ 0 & 1_{1 \times N} & 0 & 0 & & & & \\ 0 & 0 & 1_{1 \times N} & 0 & & & & \\ 0 & 0 & 0 & 1_{1 \times N} & & & & \end{array} \right) \left(\begin{array}{c} u_1 \\ u_2 \\ u_3 \\ p \\ c_1 \\ c_2 \\ c_3 \\ c_4 \end{array} \right) = \frac{RaT}{\sqrt{x_1^2 + x_2^2 + x_3^2}} \left(\begin{array}{c} x_1 \\ x_2 \\ x_3 \\ 0 \\ \int_{\Omega} u_1 \partial \bar{\Omega} \\ \int_{\Omega} u_2 \partial \Omega \\ \int_{\Omega} u_3 \partial \Omega \\ \int_{\Omega} p \partial \Omega \end{array} \right). \quad (6.15)$$

Author's Note: Need the integral of my manufactured solution on the RHS. ℓ_1 norm does not converge to 0, so it will screw solve with constraints where the subscript on $1_{N \times 1}$ indicates a $N \times 1$ vector of ones. These constraints add the unknowns (c_1, c_2, c_3, c_4) , which should solve to be zero. The four rows on the bottom require that the solution satisfy the integral over the domain for each solution component. In combination with the four added columns, the constraints indicate that the solution components must satisfy integrals using the same constant value. This is only possible if the constants are zero. Our added constraints are not chosen for physical significance, but for algebraic significance. When solving Equation 6.15 with GMRES, the constraints improve conditioning of the system and increase the rate of convergence.

We also investigate the use of GMRES without constraints. This increases the number of iterations required to converge, but allows increased parallelism (decreased data sharing). Author's Note: Perhaps we can iterate without constraints until convergence slows then "restart" the problem on a single GPU with constraints included? Limits scalability but would allow more parallelism for part of iterations while also reasonable convergence.

6.6.2 Manufactured Solution

To verify our implementation, we manufacture a solution that satisfies the continuity equation. Using the identity

$$\nabla \cdot (\nabla \times g(\mathbf{x})) = 0, \quad (6.16)$$

for any function $g(\mathbf{x})$, we can easily manufacture a solution by choosing some vector function $g(\mathbf{x})$, projecting it onto the sphere via $P_x g(x)$ and applying the curl projection, Q_x :

$$Q_x = \begin{bmatrix} 0 & -x_3 & x_2 \\ x_3 & 0 & -x_1 \\ -x_2 & x_1 & 0 \end{bmatrix}. \quad (6.17)$$

Figure 6.2: A divergence free field is manufactured for the sphere.

Then, a manufactured solution that satisfies both momentum and continuity conditions on the surface of the sphere is given by:

$$\mathbf{u} = Q_x(g(\mathbf{x})) \quad (6.18)$$

Typically, on the surface of the sphere, the projection operator from Equation 6.11 must be applied to an arbitrary $g(\mathbf{x})$. Here, we choose the components of $g(\mathbf{x})$ to be various spherical harmonics in Cartesian coordinates where $P_x Y_l^m = Y_l^m$. Consequently, application of P_x can be ignored.

We select $g(x)$ to be:

$$g(x) = 8Y_3^2 - 3Y_{10}^5 + Y_{20}^{20} \quad (6.19)$$

and the pressure function:

$$P = Y_6^4 \quad (6.20)$$

The manufactured solution is shown in Figure 6.2. A Mollweide projection [?] maps the sphere onto the plane.

Convergence

As the problem size N increases, we expect the approximation to the solution to converge on the order of \sqrt{n} where n is the choice of stencil size. Figure ?? demonstrates the convergence of our solution with respect to \sqrt{N} for stencil sizes $n = 31, 101$ Author's Note: [update when figure is complete](#).

6.7 Preconditioning

GMRES is slow to converge when used without a preconditioner.

The differentiation matrix produced by RBF-FD is asymmetric, non-positive definite, and non-diagonally dominant. Thus, many of the popular choices for preconditioning provided by CUSP and ViennaCL do not apply.

Our tests show that an incomplete LU factorization with zero fill-in [65] functions well.

We also find that a large Krylov subspace must be saved. GMRES converges best when approximately 250 dimensions are saved between restarts.

[Plot comparing residual of GMRES without precond and with ILU0](#)

Author's Note: [Need to comment on the conditioning of the system and how stencils can influence convergence](#).

Need a table/plot comparing convergence of various preconditioners (ILU0, ILUT, AMG, etc.). We will justify our use of ILU0 even if it is the most basic and frequently least beneficial approach.

Demonstrate ILU0 is best for converging between

- Jacobi

- ILU0 on block ($1 : 3 * N$)
- ILU0 on full matrix
- ILUT
- AMG

Algorithm 6.2 Incomplete LU Factorization with Zero Fill-in (ILU0)

```

1: for i do = 0
2:    $a_{i,i} = a_{i,i}/a_{i,i}$ 
3: end for
```

6.8 GMRES Results

We want to express benchmarks in terms of the number of GMRES iterations per second, and the number of iterations required to converge. Readers wont care what percentage of peak we are getting, just how fast we get to the solution.

- One GPU
 - Convergence for stokes steady
 - GMRES iteration plot (assuming 1e-8 and restart=60)
- Multi-GPU
 - Number of iterations without constraints
 - Number of iterations with constraints
 - GMRES iteration plot
 - plot: number of GMRES iterations per second w.r.t. number of processors

6.9 Fragments

Need to describe the solver.

State that the conditions under which a problem is solved determines how quickly it will converge. For example, nodes too close together on delaunay meshes cause higher condition numbers and require more iterations. Proper choice of preconditioners can dramatically reduce the number of iterations required to converge. Although preconditioners incur an additional cost in preprocessing and at each iteration of the solver, the potential number of iterations they save

John Dennis dissertation has a list of nice datasets (compare the list to Hoth) and their preconditioners. We might list similar paramters used for results here.

Bibliography

- [1] E. Anderson, Z. Bai, C. Bischof, S. Blackford, J. Demmel, J. Dongarra, J. Du Croz, A. Greenbaum, S. Hammarling, A. McKenney, and D. Sorensen. *LAPACK Users' Guide*. Society for Industrial and Applied Mathematics, Philadelphia, PA, third edition, 1999. [24](#)
- [2] Jacques M. Bahi, Raphaël Couturier, and Lilia Ziane Khodja. Parallel gmres implementation for solving sparse linear systems on gpu clusters. In Layne T. Watson, Gary W. Howell, William I. Thacker, and Steven Seidel, editors, *SpringSim (HPC)*, pages 12–19. SCS/ACM, 2011. [61](#), [63](#), [64](#)
- [3] Sylvie Barak. Gpu technology key to exascale says nvidia. <http://www.eetimes.com/electronics-news/4230659/GPU-technology-key-to-exascale-says-Nvidia>, November 2011. [19](#)
- [4] R. K. Beatson, W. A. Light, and S. Billings. Fast Solution of the Radial Basis Function Interpolation Equations: Domain Decomposition Methods. *SIAM J. Sci. Comput.*, 22(5):1717–1740, 2000. [34](#)
- [5] Nathan Bell and Michael Garland. Implementing sparse matrix-vector multiplication on throughput-oriented processors. *Proceedings of the Conference on High Performance Computing Networking, Storage and Analysis - SC '09*, (1):1, 2009. [37](#), [43](#), [62](#)
- [6] Evan F. Bollig, Natasha Flyer, and Gordon Erlebacher. Solution to pdes using radial basis function finite-differences (rbf-fd) on multiple gpus. *Journal of Computational Physics*, (0):–, 2012. [32](#)
- [7] J. C. Carr, R. K. Beatson, J. B. Cherrie, T. J. Mitchell, W. R. Fright, B. C. McCallum, and T. R. Evans. Reconstruction and Representation of 3D Objects with Radial Basis Functions. In *SIGGRAPH '01: Proceedings of the 28th annual conference on Computer graphics and interactive techniques*, pages 67–76, New York, NY, USA, 2001. ACM. [14](#)
- [8] J. C. Carr, R. K. Beatson, B. C. McCallum, W. R. Fright, T. J. McLennan, and T. J. Mitchell. Smooth Surface Reconstruction from Noisy Range Data. In *GRAPHITE '03: Proceedings of the 1st international conference on Computer graphics and interactive techniques in Australasia and South East Asia*, pages 119–ff, New York, NY, USA, 2003. ACM. [14](#)

- [9] Tom Cecil, Jianliang Qian, and Stanley Osher. Numerical Methods for High Dimensional Hamilton-Jacobi Equations Using Radial Basis Functions. *JOURNAL OF COMPUTATIONAL PHYSICS*, 196:327–347, 2004. [10](#), [20](#), [59](#)
- [10] G Chandhini and Y Sanyasiraju. Local RBF-FD Solutions for Steady Convection-Diffusion Problems. *International Journal for Numerical Methods in Engineering*, 72(3), 2007. [10](#), [20](#), [59](#)
- [11] P P Chinchapatnam, K Djidjeli, P B Nair, and M Tan. A compact RBF-FD based meshless method for the incompressible Navier-Stokes equations. *Proceedings of the Institution of Mechanical Engineers, Part M: Journal of Engineering for the Maritime Environment*, 223(3):275–290, March 2009. [20](#), [59](#), [60](#)
- [12] Michael Connor and Piyush Kumar. Fast construction of k-nearest neighbor graphs for point clouds. *IEEE Transactions on Visualization and Computer Graphics*, 16:599–608, 2010. [45](#)
- [13] CD Correa, D Silver, and M Chen. Volume Deformation via Scattered Data Interpolation. *Proceedings of Eurographics/IEEE VGTC Workshop on Volume Graphics*, pages 91–98, 2007. [10](#)
- [14] Oleg Davydov and Dang Thi Oanh. On the optimal shape parameter for gaussian radial basis function finite difference approximation of the poisson equation. *Computers Mathematics with Applications*, 62(5):2143 – 2161, 2011. [10](#), [22](#), [33](#)
- [15] K Dekker. Parallel GMRES and Domain Decomposition. Technical report, Delft University of Technology, Delft, The Netherlands, 2000. [61](#)
- [16] E Divo and AJ Kassab. An Efficient Localized Radial Basis Function Meshless Method for Fluid Flow and Conjugate Heat Transfer. *Journal of Heat Transfer*, 129:124, 2007. [10](#), [17](#), [34](#)
- [17] Qiang Du, Max Gunzburger, Lili Ju, and Xiaoqiang Wang. Centroidal Voronoi Tessellation Algorithms for Image Compression, Segmentation, and Multichannel Restoration. *Journal of Mathematical Imaging and Vision*, 24(2):177–194, 2006. [58](#)
- [18] Qiang Du, Max D. Gunzburger, and Lili Ju. Voronoi-based Finite Volume Methods, Optimal Voronoi Meshes, and PDEs on the Sphere. *Computer Methods in Applied Mechanics and Engineering*, 192:3933–3957, August 2003. [30](#)
- [19] G. E. Fasshauer. RBF Collocation Methods and Pseudospectral Methods. Technical report, 2006. [5](#), [8](#), [10](#), [17](#)
- [20] Gregory E. Fasshauer. Solving Partial Differential Equations by Collocation with Radial Basis Functions. In *In: Surface Fitting and Multiresolution Methods A. Le M’ehaut’e, C. Rabut and L.L. Schumaker (eds.)*, Vanderbilt, pages 131–138. University Press, 1997. [7](#), [8](#), [10](#), [15](#)

- [21] Gregory E. Fasshauer. *Meshfree Approximation Methods with MATLAB*, volume 6 of *Interdisciplinary Mathematical Sciences*. World Scientific Publishing Co. Pte. Ltd., 5 Toh Tuck Link, Singapore 596224, 2007. 5, 6, 8, 9, 10, 12, 15, 17, 22, 25, 31, 32
- [22] Gregory E. Fasshauer and Jack G. Zhang. On choosing “optimal” shape parameters for rbf approximation. *Numerical Algorithms*, 45(1-4):345–368, 2007. 9
- [23] A. I. Fedoseyev, M. J. Friedman, and E. J. Kansa. Improved Multiquadric Method for Elliptic Partial Differential Equations via PDE Collocation on the Boundary. *Computers & Mathematics with Applications*, 43(3-5):439 – 455, 2002. 7, 8, 10, 16
- [24] Natasha Flyer and Bengt Fornberg. Radial basis functions: Developments and applications to planetary scale flows. *Computers & Fluids*, 46(1):23–32, July 2011. 4, 9, 10, 59
- [25] Natasha Flyer and Erik Lehto. Rotational transport on a sphere: Local node refinement with radial basis functions. *Journal of Computational Physics*, 229(6):1954–1969, March 2010. 4, 10, 49, 59
- [26] Natasha Flyer, Erik Lehto, Sebastien Blaise, Grady B. Wright, and Amik St-Cyr. Rbf-generated finite differences for nonlinear transport on a sphere: shallow water simulations. *Submitted to Elsevier*, pages 1–29, 2011. 10, 20, 22, 26, 27, 31, 32, 33, 48, 51, 59, 62, 67
- [27] Natasha Flyer and Grady B. Wright. Transport schemes on a sphere using radial basis functions. *Journal of Computational Physics*, 226(1):1059 – 1084, 2007. 4, 9, 10, 20, 49, 53, 54, 58, 59
- [28] Natasha Flyer and Grady B. Wright. A Radial Basis Function Method for the Shallow Water Equations on a Sphere. In *Proc. R. Soc. A*, volume 465, pages 1949–1976, December 2009. 4, 9, 10, 26, 59, 67
- [29] B Fornberg, T Driscoll, G Wright, and R Charles. Observations on the behavior of radial basis function approximations near boundaries. *Computers & Mathematics with Applications*, 43(3-5):473–490, February 2002. 22, 62
- [30] B Fornberg, N Flyer, and JM Russell. Comparisons Between Pseudospectral and Radial Basis Function Derivative Approximations. *IMA Journal of Numerical Analysis*, 2009. 29
- [31] B. Fornberg and G. Wright. Stable computation of multiquadric interpolants for all values of the shape parameter. *Computers & Mathematics with Applications*, 48(5-6):853 – 867, 2004. 5, 10, 11
- [32] Bengt Fornberg, Elisabeth Larsson, and Natasha Flyer. Stable Computations with Gaussian Radial Basis Functions in 2-D. Technical Report 2009-020, Uppsala University, August 2009. 11

- [33] Bengt Fornberg, Elisabeth Larsson, and Natasha Flyer. Stable Computations with Gaussian Radial Basis Functions. *SIAM J. on Scientific Computing*, 33(2):869—892, 2011. [5](#), [10](#), [22](#), [49](#)
- [34] Bengt Fornberg and Erik Lehto. Stabilization of RBF-generated finite difference methods for convective PDEs. *Journal of Computational Physics*, 230(6):2270–2285, March 2011. [10](#), [20](#), [22](#), [27](#), [29](#), [31](#), [32](#), [49](#), [53](#), [59](#), [62](#)
- [35] Bengt Fornberg and Cécile Piret. A Stable Algorithm for Flat Radial Basis Functions on a Sphere. *SIAM Journal on Scientific Computing*, 30(1):60–80, 2007. [5](#), [11](#), [29](#)
- [36] Bengt Fornberg and Cécile Piret. On Choosing a Radial Basis Function and a Shape Parameter when Solving a Convective PDE on a Sphere. *Journal of Computational Physics*, 227(5):2758 – 2780, 2008. [5](#), [6](#), [10](#), [49](#)
- [37] Richard Franke. Scattered Data Interpolation: Tests of Some Method. *Mathematics of Computation*, 38(157):181–200, 1982. [5](#), [10](#)
- [38] D Göddeke, SHM Buijssen, H Wobker, and S Turek. GPU Acceleration of an Unmodified Parallel Finite Element Navier–Stokes Solver. *High Performance Computing and Simulation*, 2009. [60](#)
- [39] Prashant Goswami, Philipp Schlegel, Barbara Solenthaler, and Renato Pajarola. Interactive sph simulation and rendering on the gpu. In *Proceedings of the 2010 ACM SIGGRAPH/Eurographics Symposium on Computer Animation*, SCA ’10, pages 55–64, Aire-la-Ville, Switzerland, Switzerland, 2010. Eurographics Association. [31](#)
- [40] R Hardy. Multiquadric Equations of Topography and Other Irregular Surfaces. *J. Geophysical Research*, (76):1–905, 1971. [4](#), [5](#)
- [41] Y. C. Hon and R. Schaback. On unsymmetric collocation by radial basis functions. *Appl. Math. Comput.*, 119(2-3):177–186, 2001. [8](#), [10](#), [12](#)
- [42] Yiu-Chung Hon, Kwok Fai Cheung, Xian-Zhong Mao, and Edward J. Kansa. A Multiquadric Solution for the Shallow Water Equations. *ASCE J. Hydraulic Engineering*, 125:524–533, 1999. [9](#), [10](#)
- [43] A. Iske. *Multiresolution Methods in Scattered Data Modeling*. Springer, 2004. [5](#), [10](#), [12](#), [13](#)
- [44] L. Ivan, H. De Sterck, S. A. Northrup, and C. P. T. Groth. Three-Dimensional MHD on Cubed-Sphere Grids: Parallel Solution-Adaptive Simulation Framework. In *20th AIAA CFD Conference*, number 3382, pages 1325–1342, 2011. [37](#)
- [45] R. Jakob-Chien, J.J. Hack, and D.L. Williamson. Spectral transform solutions to the shallow water test set. *Journal of Computational Physics*, 119(1):164–187, 1995. [48](#)
- [46] Masanori Kameyama, Akira Kageyama, and Tetsuya Sato. Multigrid-based simulation code for mantle convection in spherical shell using Yin–Yang grid. *Physics of the Earth and Planetary Interiors*, 171(1-4):19–32, December 2008. [58](#)

- [47] E J Kansa. Multiquadratics—A scattered data approximation scheme with applications to computational fluid-dynamics. I. Surface approximations and partial derivative estimates. *Computers Math. Applic.*, (19):127–145, 1990. [4](#), [6](#), [7](#), [8](#), [10](#), [14](#), [58](#)
- [48] E J Kansa. Multiquadratics—A scattered data approximation scheme with applications to computational fluid-dynamics. II. Solutions to parabolic, hyperbolic and elliptic partial differential equations. *Computers Math. Applic.*, (19):147–161, 1990. [4](#), [6](#), [7](#), [8](#), [10](#), [14](#)
- [49] George Karypis and Vipin Kumar. A fast and high quality multilevel scheme for partitioning irregular graphs. *SIAM Journal on Scientific Computing*, 20(1):359–392, 1999. [38](#)
- [50] Khronos OpenCL Working Group. *The OpenCL Specification (Version: 1.0.48)*, October 2009. [41](#), [43](#), [45](#)
- [51] G Kosec and B Šarler. Solution of thermo-fluid problems by collocation with local pressure correction. *International Journal of Numerical Methods for Heat & Fluid Flow*, 18, 2008. [10](#), [34](#)
- [52] Elisabeth Larsson and Bengt Fornberg. A Numerical Study of some Radial Basis Function based Solution Methods for Elliptic PDEs. *Comput. Math. Appl.*, 46:891–902, 2003. [5](#), [8](#), [10](#), [11](#), [15](#), [16](#)
- [53] Yuxu Lin, Chun Chen, Mingli Song, and Zicheng Liu. Dual-RBF based surface reconstruction. *Vis Comput.*, 25(5-7):599–607, May 2009. [10](#)
- [54] X. Liu, G.R. Liu, K. Tai, and K.Y. Lam. Radial point interpolation collocation method (RPICM) for partial differential equations. *Computers & Mathematics with Applications*, 50(8-9):1425 – 1442, 2005. [10](#)
- [55] Dave a. May and Louis Moresi. Preconditioned iterative methods for Stokes flow problems arising in computational geodynamics. *Physics of the Earth and Planetary Interiors*, 171(1-4):33–47, December 2008. [60](#)
- [56] Bryan S. Morse, Terry S. Yoo, Penny Rheingans, David T. Chen, and K. R. Subramanian. Interpolating implicit surfaces from scattered surface data using compactly supported radial basis functions. In *ACM SIGGRAPH 2005 Courses*, SIGGRAPH ’05, New York, NY, USA, 2005. ACM. [9](#), [10](#)
- [57] C.T. Mouat and R.K. Beatson. RBF Collocation. Technical Report UCDMS2002/3, Department of Mathematics & Statistics, University of Canterbury, New Zealand, February 2002. [10](#), [11](#), [15](#)
- [58] Ramachandran D. Nair and Christiane Jablonowski. Moving Vortices on the Sphere: A Test Case for Horizontal Advection Problems. *Monthly Weather Review*, 136(2):699–711, February 2008. [48](#)
- [59] R.D. Nair, S.J. Thomas, and R.D. Loft. A discontinuous Galerkin transport scheme on the cubed sphere. *Monthly Weather Review*, 133(4):814–828, April 2005. [48](#), [53](#), [58](#)

- [60] NVidia. *NVIDIA CUDA - NVIDIA CUDA C - Programming Guide version 4.0*, March 2011. [43](#), [45](#)
- [61] Jia Pan and Dinesh Manocha. Fast GPU-based Locality Sensitive Hashing for K-Nearest Neighbor Computation. *Proceedings of the 19th ACM SIGSPATIAL GIS '11*, 2011. [31](#)
- [62] DA Randall, TD Ringler, and RP Heikes. Climate modeling with spherical geodesic grids. *Computing in Science & Engineering*, pages 32–41, 2002. [37](#), [58](#)
- [63] Karl Rupp, Florian Rudolf, and Josef Weinbub. ViennaCL-A High Level Linear Algebra Library for GPUs and Multi-Core CPUs. In *Proc. GPUScA*, pages 51—56, 2010. [37](#), [61](#), [62](#)
- [64] Youcef Saad and Martin H. Schultz. GMRES: A generalized minimal residual algorithm for solving nonsymmetric linear systems. *SIAM J. Sci. Stat. Comput.*, 7(3):856–869, 1986. [62](#)
- [65] Yousef Saad. *Iterative Methods for Sparse Linear Systems*. Society for Industrial Mathematics, second edition, 2003. [36](#), [46](#), [69](#)
- [66] C. Sanderson. Armadillo: An open source c++ linear algebra library for fast prototyping and computationally intensive experiments. Technical report, NICTA, 2010. [50](#)
- [67] Robert Schaback. Multivariate Interpolation and Approximation by Translates of a Basis Function. In C.K. Chui and L.L. Schumaker, editors, *Approximation Theory VIII—Vol. 1: Approximation and Interpolation*, pages 491–514. World Scientific Publishing Co., Inc, 1995. [5](#), [11](#), [20](#)
- [68] J. Schmidt, C. Piret, B.J. Kadlec, D.A. Yuen, E. Sevre, N. Zhang, and Y. Liu. Simulating Tsunami Shallow-Water Equations with Graphics Accelerated Hardware (GPU) and Radial Basis Functions (RBF). In *South China Sea Tsunami Workshop*, 2008. [34](#)
- [69] J. Schmidt, C. Piret, N. Zhang, B.J. Kadlec, D.A. Yuen, Y. Liu, G.B. Wright, and E. Sevre. Modeling of Tsunami Waves and Atmospheric Swirling Flows with Graphics Processing Unit (GPU) and Radial Basis Functions (RBF). *Concurrency and Computat.: Pract. Exper.*, 2009. [10](#), [34](#), [59](#), [60](#)
- [70] C. Shu, H. Ding, and K. S. Yeo. Local radial basis function-based differential quadrature method and its application to solve two-dimensional incompressible Navier-Stokes equations. *Computer Methods in Applied Mechanics and Engineering*, 192(7-8):941 – 954, 2003. [10](#), [20](#), [59](#)
- [71] C Shu, H Ding, and N Zhao. Numerical Comparison of Least Square-Based Finite-Difference (LSFD) and Radial Basis Function-Based Finite-Difference (RBFFD) Methods. *Computers and Mathematics with Applications*, 51(8):1297–1310, 2006. [10](#), [11](#), [20](#)

- [72] Ian H. Sloan and Robert S. Womersley. Extremal systems of points and numerical integration on the sphere. *Adv. Comput. Math*, 21:107–125, 2003. [29](#), [49](#), [55](#)
- [73] D Stevens, H Power, M Lees, and H Morvan. The use of PDE centres in the local RBF Hermitian method for 3D convective-diffusion problems. *Journal of Computational Physics*, 2009. [8](#), [10](#), [11](#), [17](#), [20](#), [59](#)
- [74] David Stevens, Henry Power, Michael Lees, and Herve Morvan. A Meshless Solution Technique for the Solution of 3D Unsaturated Zone Problems, Based on Local Hermitian Interpolation with Radial Basis Functions. *Transp Porous Med*, 79(2):149–169, Sep 2008. [10](#), [11](#), [17](#)
- [75] David Stevens, Henry Power, and Herve Morvan. An order-N complexity meshless algorithm for transport-type PDEs, based on local Hermitian interpolation. *Engineering Analysis with Boundary Elements*, 33(4):425 – 441, 2008. [10](#), [11](#), [17](#), [34](#)
- [76] A. I. Tolstykh and D. A. Shirobokov. On using radial basis functions in a “finite difference mode” with applications to elasticity problems. In *Computational Mechanics*, volume 33, pages 68 – 79. Springer, December 2003. [20](#), [59](#)
- [77] A.I. Tolstykh. On using RBF-based differencing formulas for unstructured and mixed structured-unstructured grid calculations. In *Proceedings of the 16 IMACS World Congress, Lausanne*, pages 1–6, 2000. [19](#), [20](#), [59](#)
- [78] Robert Vertnik and Božidar Šarler. Meshless local radial basis function collocation method for convective-diffusive solid-liquid phase change problems. *International Journal of Numerical Methods for Heat & Fluid Flow*, 16(5):617–640, 2006. [10](#), [17](#)
- [79] B. Šarler and R. Verntnik. Meshfree Explicit Local Radial Basis Function Collocation Method for Diffusion Problems. *Computers and Mathematics with Applications*, 51(8):1269–1282, 2006. [10](#), [17](#)
- [80] J. G. Wang and G. R. Liu. A point interpolation meshless method based on radial basis functions. *Int. J. Numer. Methods Eng.*, 54, 2002. [10](#)
- [81] Geoffrey Womeldorf. Spherical Centroidal Voronoi Tessellations: Point Generation and Density Functions Via Images. Master’s thesis, Florida State University, 2008. [30](#)
- [82] Robert S. Womersley and Ian H Sloan. How good can polynomial interpolation on the sphere be?, 2001. [29](#)
- [83] Grady Wright and Bengt Fornberg. Scattered node mehrstellenverfahren-type formulas generated from radial basis functions. In *The International Conference on Computational Methods*, December 15-17 2004. [10](#), [20](#)
- [84] Grady B. Wright. *Radial Basis Function Interpolation: Numerical and Analytical Developments*. PhD thesis, University of Colorado, 2003. [10](#), [20](#), [22](#), [59](#)
- [85] Grady B. Wright, Natasha Flyer, and David A. Yuen. A hybrid radial basis function-pseudospectral method for thermal convection in a 3-d spherical shell. *Geochem. Geophys. Geosyst.*, 11(Q07003):18 pp., 2010. [4](#), [9](#), [10](#), [17](#), [26](#), [58](#), [59](#), [67](#)

- [86] Grady B. Wright and Bengt Fornberg. Scattered node compact finite difference-type formulas generated from radial basis functions. *J. Comput. Phys.*, 212(1):99–123, 2006. [10](#), [12](#), [20](#), [22](#), [62](#)
- [87] Z M Wu. Hermite-Birkhoff interpolation of scattered data by radial basis functions. *Approx. Theory Appl.*, (8):1–10, 1992. [8](#)
- [88] Xuan Yang, Zhixiong Zhang, and Ping Zhou. Local Elastic Registration of Multimodal Medical Image Using Robust Point Matching and Compact Support RBF. In *BMEI '08: Proceedings of the 2008 International Conference on BioMedical Engineering and Informatics*, pages 113–117, Washington, DC, USA, 2008. IEEE Computer Society. [10](#)
- [89] Rio Yokota, L.A. Barba, and Matthew G. Knepley. PetRBF — A parallel O(N) algorithm for radial basis function interpolation with Gaussians. *Computer Methods in Applied Mechanics and Engineering*, 199(25-28):1793–1804, May 2010. [34](#), [60](#), [61](#)
- [90] Hao Zhang and Marc G. Genton. Compactly supported radial basis function kernels, 2004. [10](#)